UNIVERSITY OF CALIFORNIA, SAN DIEGO

Convective Heating Analysis of an IFE Target in a High Temperature, Low Reynolds Number Xenon Environment

A Thesis submitted in partial satisfaction of the requirements
For the degree of Master of Science

in

Engineering Sciences (Mechanical Engineering)

by

Dain Steffen Holdener

Committee in charge:

Professor Mark Tillack, Chair
Professor Yousef Bahadori
Professor Farrokh Najmabadi
Professor George Tynan

2011

The Thesis of Dain Steffen Holdener is approved and it is acceptable in quality and form for publication on microfilm and electronically:

_____

_____

_____

_____

Chair

University of California, San Diego

2011

DEDICATION

I would like to dedicate this work to my friends and loved ones who have supported me throughout my academic studies. To my parents, who instilled in me the value of hard work, honesty and integrity, I will forever be grateful. Above all, I would like to dedicate this work to Christ, my rock and Savior. I pray that You continue to bless me in my life and career so that I can continue to honor Your name.

TABLE OF CONTENTS

LIST OF FIGURES

LIST OF TABLES

ACKNOWLEDGEMENTS

I would like acknowledge and thank Professor Tillack for the opportunity in focusing my graduate studies in support of fusion energy, a project I feel very strongly for. I would also like to thank Professor Tillack for his support as my academic advisor and chair of my committee. Being relatively new to the field of fusion energy, Professor Tillack's wealth of knowledge and experience in this field has been tremendously insightful, especially in guiding me on how I might best contribute in the face of shifting project priorities and design parameters.

I would also like to thank the members of my thesis committee for their patience, insight and interest in my work. I would especially like to thank Professor Bahadori for introducing me to physical gas dynamics and the many hours spent after lecture reviewing my research. My understanding in this field proved invaluable throughout my graduate studies.

I also would like to thank Xueren Wang for collaborating with Professor Tillack and myself in this effort. His expertise in using ANSYS, and willingness to share his knowledge with me was invaluable.

I thank Jeff Latkowski, Gwen Loosemore, Robin Miles and Mark Havstad for the opportunity to work along side the LIFE team at LLNL. I would especially like to thank Matt McNenly at LLNL for being so gracious with his free time in guiding me in the proper implementation and use of DS2V.

I would finally like to thank my good friends Adam Pechner and Rob Martin for their unwavering support. If I ever needed someone to talk to regarding my work, whether a question in conceptual understanding or simply a sanity check, I would always

turn to Adam and Rob first, and without hesitation. As always, your help is very much appreciated!

Chapter 2, in part, contains materials submitted to Transactions of Fusion Science and Technology, June 2011. Holdener, D. S., Tillack, M. S., Wang, X. R., 2011. The thesis author was the primary investigator and author of this paper.

Chapter 3, in part, contains materials submitted to Transactions of Fusion Science and Technology, June 2011. Holdener, D. S., Tillack, M. S., Wang, X. R., 2011. The thesis author was the primary investigator and author of this paper.

Chapter 4, in part, contains materials submitted to Transactions of Fusion Science and Technology, June 2011. Holdener, D. S., Tillack, M. S., Wang, X. R., 2011. The thesis author was the primary investigator and author of this paper.

Chapter 5, in part, contains materials submitted to Transactions of Fusion Science and Technology, June 2011. Holdener, D. S., Tillack, M. S., Wang, X. R., 2011. The thesis author was the primary investigator and author of this paper.

Appendix A, in part, contains materials submitted to Transactions of Fusion Science and Technology, June 2011. Holdener, D. S., Tillack, M. S., Wang, X. R., 2011. The thesis author was the primary investigator and author of this paper.

ABSTRACT OF THE THESIS

Convective Heating Analysis of an IFE Target in a High Temperature, Low Reynolds Number Xenon Environment

by

Dain Steffen Holdener

Engineering Sciences (Mechanical Engineering)

University of California, San Diego, 2011

Professor Mark Tillack, Chair

Target survival in the hostile chamber environment of the proposed Laser Inertial Fusion Energy (LIFE) power plant is critical. The main focus of this work is to investigate the flow properties and convective heat load imposed upon the target traveling through the high-temperature xenon environment. This rarefied flow is characterized within the continuum regime, but is approaching transition where traditional CFD codes

reach the bounds of operation. Thus ANSYS, specifically the Navier-Stokes module CFX, will be used in parallel with direct simulation Monte Carlo code DS2V and empirically and analytically derived expressions of heat transfer to the target for validation. Comparison of the DS2V and ANSYS viscous and thermal boundary layers were shown to match almost identically, while the simulated heat fluxes vary less than 8% on average over the hohlraum's surface.

Since melting of the laser entrance hole window or fuel capsule constitutes failure of the target, a first-order approximation of the transient thermo-mechanical behavior of the target was conducted using the multi-physics code, COMSOL. Helium internal to the target has been shown to act as tremendous heat sink for cooling the laser entrance hole windows; however, spinning the target at 15,000 RPM induced buoyancy driven swirling effects that heated the sensitive fuel capsule. From the results herein, external baffles and radiative shields that completely partition the internal helium of the hohlraum have been shown to reduce this heating and optimize target survival in conjunction with other key reactor parameters.

Chapter 1:

Introduction

Fusion energy is the power source of our Sun, making sustained life on Earth possible. Demonstrating energy gain from a fusion reaction eludes scientists to this day, but if shown successful a tremendous energy source in form of the hydrogen isotope deuterium mined from water is readily available. Approximately 2/3 of the Earth's surface is covered in water, and assuming an average depth of 3000 m, the ocean has a volume of 10^{14} m^3 and a mass of 10^{21} kg. Of this mass, 1/9 is comprised of hydrogen, and 2/6700 of the hydrogen mass is deuterium. This equates to a deuterium mass of 2.2 x 10^{16} kg, or 10^{31} J of energy, a virtually limitless supply for practical purposes.[1] Inherently safe, and proliferation resistant, fusion has the capability in becoming a 'game-changer' in meeting global energy demands for the 21st century, and thus has been at the forefront of scientific research for the past 50 years.

Two general methods have been adopted as the means of obtaining ignition: magnetic and inertial confinement. Despite the processes of nuclear fusion being well understood, the confinement conditions required for thermonuclear burn lies on the edge of current technology. Fusion ignition with energy gain has yet to be demonstrated in the laboratory, yet scientists are still attempting to show a controlled nuclear burn is possible.

The International Thermonuclear Experimental Reactor (ITER) is the most advanced magnetic tokamak nuclear fusion reactor currently under construction. ITER is being built in Cadarache, France and is expected to create its first plasma by November, 2019.[2] The National Ignition Facility (NIF) operated by Lawrence Livermore National Laboratory (LLNL), in Livermore, California boasts the current most energetic operational laser allowing for strides in inertial fusion research. NIF has successfully demonstrated 1.1 MJ of combined energy from 192 individual laser beams, breaking the MegaJoule barrier thought to be required to obtain energy gain. The NIF facility began ignition experiments in the fall of 2010, and is hopeful in demonstrating a reliable and repeatable ignition platform by the end of 2012.[3]

Researchers at LLNL have begun designing an inertial fusion energy power plant, LIFE or Laser Inertial Fusion Energy based on the operational principals of NIF assuming it is successful in achieving thermonuclear burn. While NIF is currently investigating the underlying physics of IFE, LIFE is being designed for commercial power production. In order to be on par with typical 1 GW power plants, LIFE is designed to continuously engage 10-20 targets per second.[4] To help absorb ion and x-ray radiation from continual thermonuclear burns, the chamber will be filled with xenon gas. However, the target must travel six meters through the chamber with the xenon gas temperature now up to 8000 K without having the laser entrance hole (LEH) windows or cryogenic deuterium-tritium ice fuel layers melt.[5,6,7] Additional background on the NIF and LIFE inertial fusion projects, in addition to previous inertial fusion energy design studies will be presented in Chapter 2.

The primary focus of this work is to investigate the flow properties and convective heat load imposed upon the target traveling through the high-temperature xenon environment, and begin to understand the target's transient thermo-mechanical behavior by applying external heat flux along the surface of the hohlraum while spinning. As opposed to direct-drive targets where an array of high-energy driver beams illuminate a fuel capsule, the indirect-drive targets suspend a cryogenic fuel capsule within a small hollow cavity, known as a hohlraum. Incident driver beams on the inside surface of the hohlraum are then converted to X-rays, bathing the fuel capsule uniformly.

The indirect-drive approach is particularly attractive for it is inherently resistant to convective heating of the chamber gas. Significant analysis of the convective heat load to direct-drive targets has demonstrated the heating constraints on the fuel capsule, limiting the density of the chamber gas.[8] With an indirect drive target, the hohlraum takes the brunt of the convective heating, protecting the sensitive fuel capsule inside. This allows for an increase in the chamber gas density to help mitigate the ion and X-ray radiation damage, but consequently changes the nature of the fluid flow.

This rarefied flow is traditionally characterized as being within the continuum regime, but is approaching transition where traditional CFD codes reach their bounds of operation. Thus ANSYS, specifically the Navier-Stokes module CFX, will be used in parallel with direct simulation Monte Carlo DS2V algorithms to investigate the flow field and heat transfer to the target. The resulting surface heat fluxes will then be compared with empirically and analytically derived correlations of heat transfer for validation. These correlations and their applicability will be discussed further in Chapter 3, along with model descriptions of the ANSYS and DS2V simulations. Comparison of the

ANSYS and DS2V viscous and thermal boundary layers are gone through in detail in Chapter 4, where they will be shown to match almost identically, while the simulated heat fluxes varying less than 8% on average.

Since melting of the LEH window or fuel capsule constitutes failure of the target, a first-order look will then be taken of the transient thermo-mechanical behavior of the target using the multi-physics code, COMSOL, the model of which will be described in detail in Chapter 3. It will be shown in Chapter 4 the LEH windows offer very little thermal resistance independently, but inclusion of the helium internal to the hohlraum acts as a tremendous heat sink for the windows. However, spinning the target will be shown to induce buoyancy-driven swirling effects that bring the heated helium towards the sensitive fuel capsule

Since the LIFE project is early in the design stages, the most recent two flight conditions and target designs will be considered throughout this work. Special emphasis has been placed on understanding fundamental heat transfer trends that include target speed and shape in addition to chamber gas temperature and density with the end goal of target optimization. These conclusions will be summarized in Chapter 5, coupled with recommendation in design specifications – including external baffles and the partitioning of internal helium – to reduce the convective heating to the LEH windows and fuel capsule and maximize their protection.

References:

1. Da, Rosa Aldo Vieira. *Fundamentals of Renewable Energy Processes*. 2nd ed. Amsterdam: Elsevier Academic, 2009: pp. 36.

2. "ITER Schedule Approved: First Plasma Due by 2019." *Nuclear Engineering International*. 29 July 2010. Web. 03 May 2011. <http://www.neimagazine.com/story.asp?storyCode=2057015>.

3. Moses, E., "Advances in Inertial Confinement Fusion at the National Ignition Facility (NIF)," Proceedings of 9th International Symposium on Fusion Nuclear Technology, Dalin, China, October 11-16, 2009, LLNL-CONF-418579.

4. Heller, Arnie. "Safe and Sustainable Energy with LIFE", *Science and Technology Review* April/May (2009): pp. 6-15.

5. Latkowski, J., personal communication, September 30, 2010.

6. Miles, R., LIFE Target Working Group Meeting (powerpoint presentation), LLNL internal document, September 20, 2010.

7. Miles, R., personal communication, September 9, 2010.

8. Christensen, B.R., Raffray, A.R., Tillack, M.S., "Thermal Loading of a Direct Drive Target in Rarefied Gas," *Fusion Science & Technology* 47.4 (2005): 1175-1179.

Chapter 2:

Inertial Confinement Fusion

2.1: Fusion Basics

Fusion is the physical phenomena where nuclei of two or more atoms combine to creating a single, heavier nucleus. This process is generally accompanied by a substantial release of energy when occurring between two atoms of low atomic number. Among the most fundamental nuclear fusion reactions is the deuterium (^{2}H or D) and tritium (^{3}H or T) fuel cycle shown in equation 2.1, where the two isotopes of hydrogen fuse together forming a single helium atom (^{4}He), a neutron (n) and a release 17.6 MeV of energy!

$$^2H + ^3H \rightarrow He + n + 17.6MeV \tag{2.1}$$

Using Einstein's equation in the form of mass-energy equivalency, the difference in mass due to fusion is accounted for.[1,2] The goal for any nuclear fusion power plant is to harness this energy release in the production of electricity.

Deuterium is a naturally occurring, stable hydrogen isotope with two molecules found in every 6,700 hydrogen atoms. It is routinely mined from water and therefore

extremely abundant. Conversely, tritium is an unstable isotope of hydrogen with a half-life of 12.32 years. While only trace elements of tritium are found naturally, it can be produced in nuclear reactors by the process of neutron activation of lithium-6 by equation 2.2.[1,3] Thus fuel is abundant to sustain deuterium-tritium fusion reactors.

$$Li + n \rightarrow T + He + 4.8MeV \tag{2.2}$$

A useful measure to define the conditions for thermonuclear burn in fusion reactors is the Lawson criterion. This formulation describes the required temperature to overcome the Coulomb barrier as a function of sufficient confinement time, τ_E, and with sufficient ion density, N, to obtain a net yield of energy gain from a fusion reaction.[4] Lawson criterion bounds for the deuterium-tritium (DT) and deuterium-deuterium (DD) fuel cycles are illustrated in Figure 2.1. The DT fuel cycle has been found to have the most relaxed confinement conditions for all fusion reactions based on this criterion, and thus is the accepted fuel cycle for the first demonstrations of thermonuclear burn in the laboratory in addition to first generation fusion power plants.

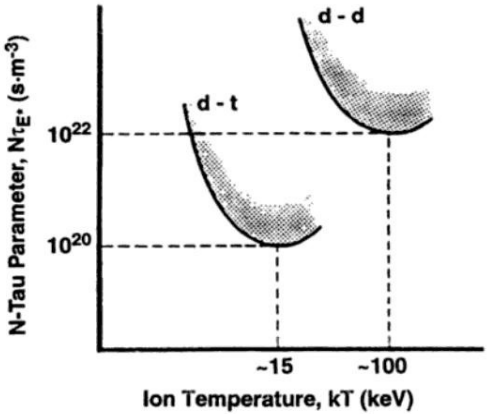

Figure 2.1: Lawson Criterion Bounds for DT and DD Fusion[4]

2.2: Inertial Confinement Fusion

Inertial fusion energy (IFE) is a technique for achieving nuclear burn whereby laser light, ion or electron beams (drivers) are used to compress a small, spherical fuel capsule. Energy from the driver is directed towards the fuel capsule, resulting in a highly symmetrical irradiation or "blowoff" of its surface. By Newton's Third Law, fuel within the capsule is accelerated radially inward, compressing the capsule and fuel to extreme temperatures and pressures while being confined by its radial inertia.

Demonstrating IFE relies on how the fuel and drivers are utilized in achieving thermonuclear ignition. The drivers may be shot directly onto the surface of the fuel capsule, or indirectly onto the interior surface of a hollow, cylindrical cavity (hohlraum) creating x-rays to compress the internally suspended fuel capsule. These two methods are known as "direct" and "indirect drive", and are the two main branches of inertial confinement fusion.

2.3: The National Ignition Facility and the National Ignition Campaign

Lawrence Livermore National Laboratory has been at the forefront of laser science and its applicability to IFE since their laser program's inception in 1972. Over the following decade, LLNL created six large fusion lasers, including the Nova laser capable of producing 100 kJ of energy in a billionth of a second. The following decade was spent understanding the underlying physics required for fusion ignition and energy gain. Although unsuccessful of achieving ignition, the sixth generation Nova experiments were key in understanding these physics. LLNL's focus then became to

engineer the next generation laser capable of achieving ignition.[5] This laser has since been named The National Ignition Facility and is shown in Figure 2.2.

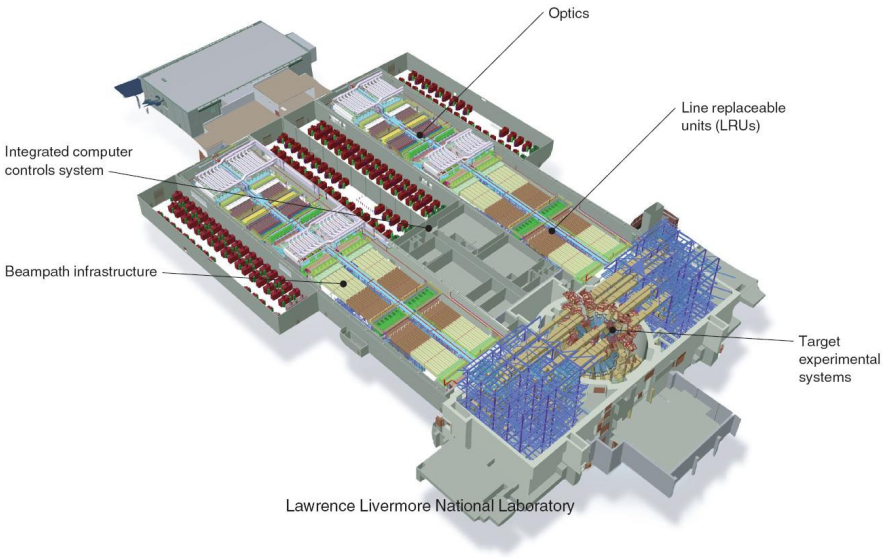

Figure 2.2: Cutaway of the National Ignition Facility, NIF[6]

As described by physicist Steve Haan, "Aside from giving us enormous experience with target design and fabrications, Nova showed us that NIF would be able to provide both the required hohlraum drive temperature and the laser symmetry to make ignition possible."[7] Comparison of the 100 lbs of laser glass required for the first generation Janus laser to the 200 tons of glass now used on NIF shows how encompassing the newer lasers have become.[5,7]

Located in Livermore, California, approximately 40 miles east of San Francisco, NIF has recently established itself as the most energetic laser in the world. On March 10, 2009, all 192 laser beams were fired to target chamber center, delivering 1.1 MJ of ultraviolet light.[8] This milestone was the first time a laser system had been able to break the much sought after "megajoule barrier," believed to be the minimum energy required to achieve a high gain fusion reaction.[5] NIF was soon certified complete by the

Department of Energy on March 31, 2009, and formally dedicated two months later on May 29, 2009.[9,10]

Lawrence Livermore National Laboratories in collaboration with Sandia and Los Alamos National Laboratories, General Atomics and the Laboratory for Laser Energetics at the University of Rochester have since formed the National Ignition Campaign (NIC) to undertake the challenge of achieving thermonuclear ignition. Incorporated into NIC are a series of integrated ignition experiments designed to look at the various parameters affecting thermonuclear burn.[11] Two have been successfully investigated, demonstrating "efficient laser coupling and symmetric capsule implosions in cryogenic hohlraum experiments" using NIF at the relatively modest level of 0.7 MJ. During this experiment, an ablation pressure of 120-142 Mbar was obtained, resulting in a maximum implosion velocity of 380 km/s and a radiation temperature of 3.3 million Kelvin, as shown in Figure 2.3.[12]

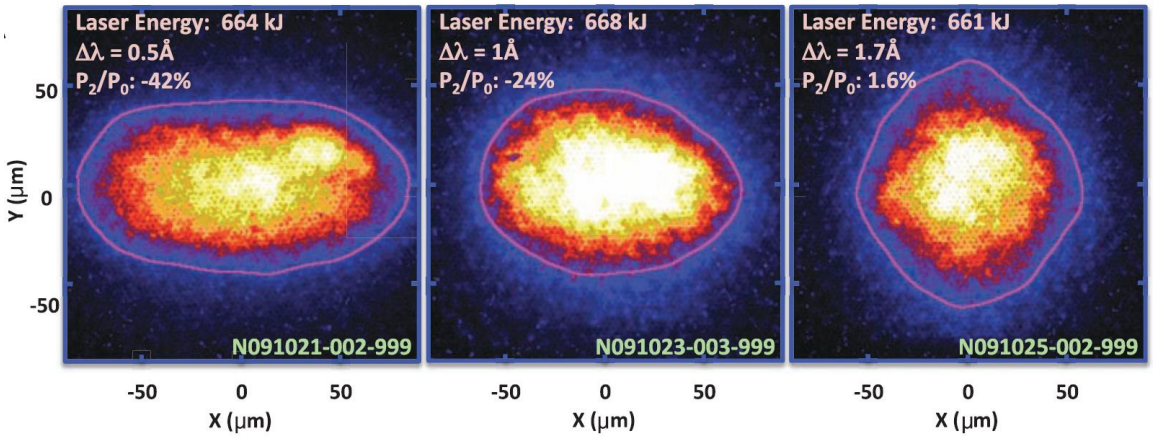

Figure 2.3: Implosion Symmetry of NIF Target[12]

2.4: The Laser Inertial Fusion Energy (LIFE) Engine

The transition from demonstrating thermonuclear burn in the laboratory to the design and implementation of an inertial confinement nuclear fusion power plant is extraordinarily difficult. Successful ignition with NIF will be critical in generating the interest and funding required in taking such an ambitious project to completion. In anticipation of NIF being successful in achieving burn, LLNL has put together a small team of physicists and engineers to begin working on the design of such a fusion power plant: the Laser Inertial Fusion Energy or LIFE engine.

The technical challenges associated with the design of the LIFE engine center around generating enough power to be competitive with modern power plants, which typically produce on the order of 1 GW of power. This can only be accomplished with the continuous engagement and ignition of approximately 10-20 targets per second.[13] Not only does this necessitate an actively cooled, high-average power laser driver comparable to the energy of NIF, but a target fabrication facility capable of producing and delivering approximately 1 million targets per day!

The target chamber will be filled with a small amount of xenon gas to stop ions and help with the absorption of x-rays during the thermonuclear burn[14], although this presents a particularly difficult challenge for the target. It must survive a flight traveling 250 m/s in a xenon gas of 8000 Kelvin to reach target chamber center.[15,16,17] Necessitating the laser entrance hole window remains intact, and a minimal amount of heat reaches the frozen DT layer during this flight is critical. The remainder of this work will be dedicated to quantifying and understanding the underlying physics of the

convective heat transfer to the target from this high temperature, low Reynold's Number xenon chamber gas to help aid in engineering the target's survival.

Since the LIFE engine is still in the early stages of design, target and chamber specifications have not been confirmed. Table 2.1 illustrates the evolution of these conditions with Figure 2.3 showing the new and old hohlraum schematics, both of which will be considered through the course of this analysis.

Table 2.1: Target Flight Conditions (TFC)[15,16,17,18,19]

	New and Old TFC *(same from Nov. 09' to Dec 10')*	
Hohlraum LEH window thickness	0.5 μm	
Hohlraum wall material	Lead	
Chamber gas	Xenon	
Internal hohlraum gas	Helium	
Initial internal hohlraum gas density	1 mg/cc	
Target spin rate	15,000 RPM	
	Old TFC *(valid Nov. 09')*	New TFC *(valid Dec. 10')*
Hohlraum radius, OD	6.6 mm	9.9 mm
Hohlraum length	11.9 mm	15.4 mm
Hohlraum wall thickness	25 μm	*(variable, see Figure 2.3)*
Hohlraum LEH window material	Polyimide (Kapton)	graphene
Chamber gas temperature	1000 K	8000 K
Chamber gas density	2.00×10^{22} /m^3	2.75×10^{22} /m^3
Chamber gas pressure at T_g	276 Pa *(2.1 torr)*	3037 Pa *(23 torr)*
Target injection velocity	200 m/s	250 m/s
Target transit distance in gas *(chamber radius)*	5 m	6 m
Initial target temperature	20 K	17 K
Initial internal target gas pressure	41,500 Pa	35,300 Pa

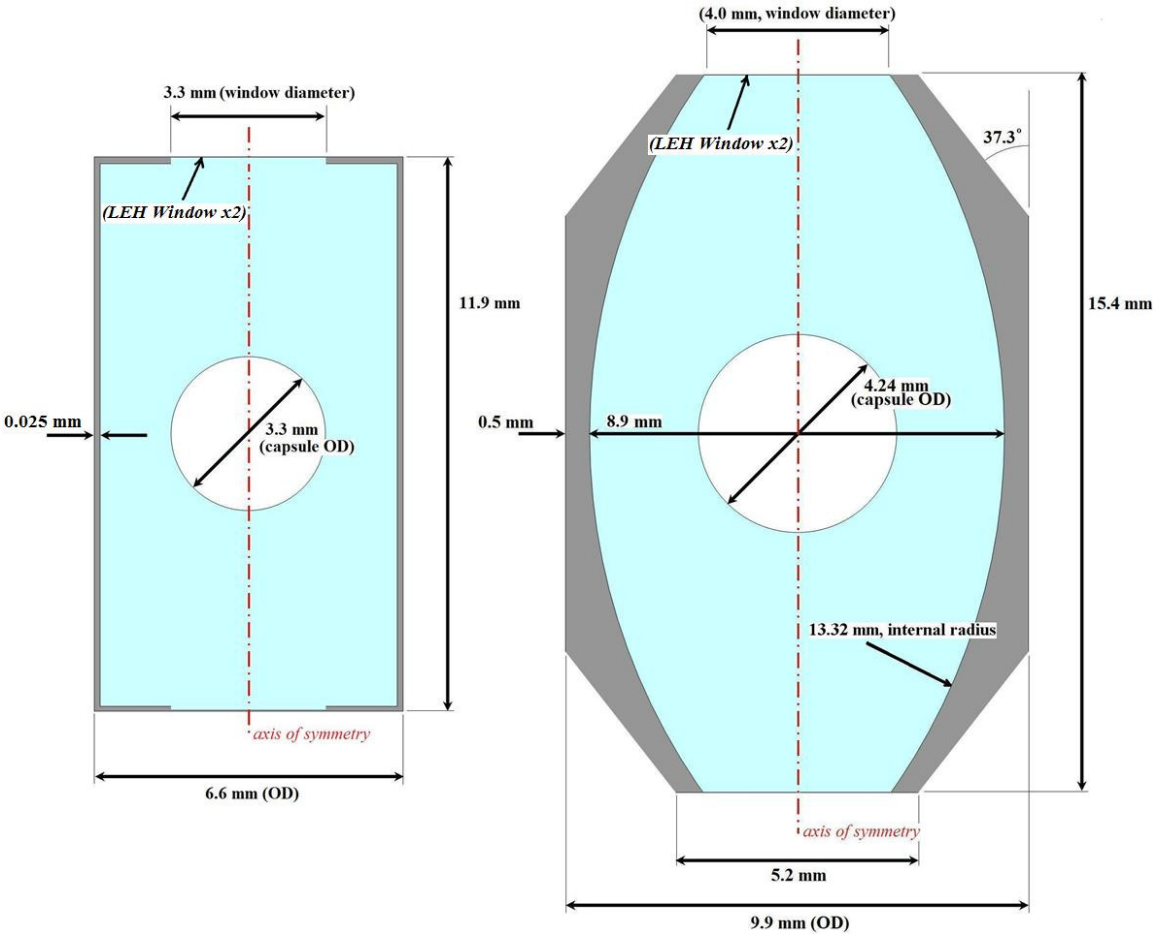

Figure 2.4: Hohlraum Schematics;
Old NIF-like Hohlraum Left[16,18], New LIFE.2 Hohlraum Right,[20,21]

2.5: Previous Work

Commercial IFE electric power plants have been the focus of a number of conceptual design studies. These studies are based on the technologies of existing IFE fuel cycles coupled with the most recent advancements in ion and laser drivers and extrapolated target technologies on performance and manufacturing capabilities. Their focus was to create a development plan for future energy independence using fusion energy. However, this work mainly focuses on the conductive heating through the fuel

capsule of direct drive targets and is only mildly applicable to the expected heating conditions of the LIFE indirect-drive targets.

In March of 1992, a final report was submitted and documented through the Department of Energy for the Prometheus-L (laser driven) and Promethieus-H (heavy ion driven) power plant design study. Promethus' chamber gas was restricted to a pressure of 3 mtorr, comprised of helium and hydrogen (with isotopes) left over from the fusion fuel cycle. The temperature of these gases and surrounding walls was believed not to exceed 873 Kelvin. Radiation from the walls was found to be the dominate heat transfer mechanism as opposed to convective heating from the ambient chamber gas, but no specific heat loads were reported. A simple code was then constructed to look at the heating of the direct drive targets for conduction through the fuel capsule into the DT ice layer. The temperature increase in the DT layer for both direct drive and indirect drive targets was found to be acceptable.[22]

A similar report was also submitted through the DOE in March of 1993 going through the OSIRIS (indirect drive, ion driven) and SOMBRERO ICF (direct drive, laser driven) power plant designs. As with Prometheus, the OSIRIS chamber pressure is very small, approximately 0.34 mtorr of Flibe gas, and as such the convective heat load is once again dominated by radiation. Fortunately, the SOMBRERO chamber conditions are very close to that of the old LIFE target chamber conditions; xenon gas at 1758 Kelvin and 6.5 torr. As with the previous studies, radiation was found to be the dominate heating mechanism. However; the extent of the convective heating analysis is very simplistic in that they limited themselves to the unreferenced correlation for the average

heating over a ‘spherical target with subsonic velocity’ of the form shown in equation 2.3.[23]

$$Nu = 0.37\,\mathrm{Re}^{0.6} \tag{2.3}$$

While this form does match closely with other spherical heating correlations shown in Chapter 4, it fails to predict the maximum and uneven heating of the DT ice layer at the forward stagnation point. Fortunately, their predicted heat flux of 42,000 W/m^2 from convective heating is on par with the LIFE heating results to follow.

The Department of Energy has continued their support for the development of key science and technology issues with the end goal of creating a practical power source using lasers in creation of the High Average Power Lasers (HAPL) program. With the support of 6 United States national laboratories, 9 universities and 14 industry partners, progress on many fronts have been made including target design, lasers, final optics, target injection, target fabrication and chamber development. However, their focus remains direct driver targets immersed in non-reacting gases, such as xenon, with considerably less density than the proposed LIFE facility, and again are only mildly applicable.[24,25]

In support of the HAPL program, a comprehensive look at the heating of direct-drive targets in a low-density, xenon environment was performed by Christensen, Raffray and Tillack. Also utilizing the commercial DSMC code DS2V, the effects of the chamber gas density, temperature, condensation and accommodation coefficients on the heat flux of the targets were explored. Nevertheless, the most severe heating conditions

investigated where for xenon gas a temperature of 4000 K and density 3.22 x 10^{21} m^{-3}, approximately one-half the temperature and an order of magnitude less dense then the new TFC of LIFE.[26] Thus, a need for updated heat transfer models with increased temperature and gas density for direct-drive targets is self evident.

Chapter 2, in part, contains materials submitted to Transactions of Fusion Science and Technology, June 2011. Holdener, D. S., Tillack, M. S., Wang, X. R., 2011. The thesis author was the primary investigator and author of this paper.

References:

1. Fay, J. A. and Golomb, D. S., *Energy and the Environment*, Oxford University Press, New York, 2002, pp. 138, 267, 276-77. [ISBN: 978-0-19-515092-6]

2. Lamarsh, J. R. and Baratta, A. J., "Atomic and Nuclear Physics," *Introduction to Nuclear Engineering*, 3rd ed., Prentice Hall, New Jersey, 2001, pp. 11-15, 29-33. [ISBN: 0-201-82498-1]

3. Harms, A. A., Schoepf, K. F., Miley, G. H., Kingdon, D. R., *Principles of Fusion Energy*, World Scientific, New Jersey, 2000, pp. 9-10, 110, 194-196, 253-255, 258-260. [ISBN: 978-981-238-033-3]

4. Harms, A. A., K. F. Schoeph, G. H. Miley, and D. R. Kingdon. *Principles of Fusion Energy*. New Delhi: Sunil Sachdev, 2002. pp. 128-131. [ISBN: 81-7764-233-2]

5. Cambell, Michael. "Laser Programs The First 25 Years... 1972-1997." *Laser Programs; University of California, Lawrence Livermore National Laboratory* UCRL-TB-128043 (1997).

6. Walter, Katie. "The National Ignition Facility Comes to Life." *Science & Technology Review* (September 2003).

7. Heller, Arnie. "On Target Designing for Ignition." *Science and Technology Review* July/August (1999): pp. 4-11.

8. Moses, E., “Advances in Inertial Confinement Fusion at the National Ignition Facility (NIF),” Proceedings of 9th International Symposium on Fusion Nuclear Technology, Dalin, China, October 11-16, 2009, LLNL-CONF-418579.

9. “Department of Energy - Department of Energy Announces Completion of World's Largest Laser." *Department of Energy - Homepage*. 31 Mar. 2009. Web. 28 May 2010. <http://www.energy.gov/news2009/7191.htm>.

10. “Dedication of World’s Largest Laser Marks the Dawn of a New Era." *Lawrence Livermore National Laboratory - Public Affairs Office*. 29 May 2009. Web. 28 May 2010. <https://publicaffairs.llnl.gov/news/news_releases/2009/NR-09-05-05.html>.

11. United States. Department of Energy. National Nuclear Security Administration. *National Ignition Campaign Execution Plan*. June 2005.

12. Glenzer, S. H., and Et Al. *Symmetric Inertial Confinement Fusion Implostions at Ultra-High Laser Energies*. Rep. no. 10.1126/science.1185634. Vol. 327. 28 January 2010. *Science Magazine*. Web. 27 May 2010.

13. Heller, Arnie. “Safe and Sustainable Energy with LIFE”, *Science and Technology Review* April/May (2009): pp. 6-15.

14. Storm, E., “LIFE: Laser Inertial Fusion Energy systems for electric power production and disposal of nuclear waste,” (LLNL powerpoint presentation to PPPL) September 25, 2009.

15. Latkowski, J., personal communication, September 30, 2010.

16. Miles, R., LIFE Target Working Group Meeting (powerpoint presentation), LLNL internal document, September 20, 2010.

17. Miles, R., personal communication, September 9, 2010.

18. Amendt, P. and Loosemore, G., “LIFE Target Details,” LLNL internal document, Aprial 22, 2009

19. Latkowski, J. “Target Concepts” (powerpoint presentation), July 13, 2009.

20. Amendt, P., “Documentation of Amendt’s initial guess of the eventual Rugby shape for a LIFE.2 target.” 1stGuessLIFE.2Rugby.ai. (powerpoint presentation), LLNL internal document.

21. Amendt, P., Cerjan, C., Hinkel, D. E., Milovich, J. L., Park, H. S. and Robey, H. F., “Rugby-like hohlraum Experimental Designs for Demonstrating X-ray Drive Enhancement.” Physics of Plasmas 15.1 (2008): 012702

22. United States. Department of Energy. *Inertial Fusion Energy Reactor Design Studies, Prometheus-L / Prometheus-H*. Vol. 2. St. Louis: McDonnell Douglas Aerospace, March 1992. MDC 92E0008, DOE/ER-54101.

23. United States. Department of Energy. *OSIRIS and SOMBRERO Inertial Fusion Power Plant Designs*. Vol. 2. March 1992. WJSA-92-01, DOE/ER/54100-1.

24. Linford, Rulon, Riccardo Betti, Jill Dahlburg, James Asay, Michael Campbell, Phillip Colella, Jeffrey Freidberg, Jeremy Goodman, David Hammer, Joseph Hoagland, Steve Jardin, John Lindl, Grant Logan, Keith Matzen, Gerald Navratil, Arthur Nobile, John Sethian, John Sheffield, Mark Tillack, and Jon Weisheit. "A Review of the U.S. Department of Energy's Inertial Fusion Energy Program." *Journal of Fusion Energy* 22.2 (2003): 93-126. *SpringerLink*. Web. 5 May 2011.

25. Sethian, John and Obenschain, Steve, "Fusion ENERGY with Lasers, Direct drive targets, and Solid wall chambers," Naval Research Laboratory, October 28, 2003.

26. Christensen, B.R., Raffray, A.R., Tillack, M.S., "Thermal Loading of a Direct Drive Target in Rarefied Gas," *Fusion Science & Technology* 47.4 (2005): 1175-1179.

Chapter 3:

Modeling Techniques

3.1: Flow Description and Modeling Challenges

The hohlraum targets, as described in Table 2.1, travel parallel to its axis of rotation through a xenon environment of elevated temperatures and sub-atmospheric pressures. Using these properties, the dimensionless variables listed in Table 3.1 can be defined and referenced in Appendix A for material and transport properties of xenon as a function of temperature.

Table 3.1: Target Dimensionless Variables

Dimensionless Variable	Formulation	Old TFC	New TFC
Reynolds number (Re)	$= (\rho v d)/\mu$	92	60
Mach number (Ma)	$= v/a = v/(\gamma RT)^{1/2}$	0.62	0.27
Knudsen number (Kn)	$= \lambda/d$	0.0084	0.0090
Prandtl number (Pr)	$= (C_p \mu)/k$	0.67	0.67

From Tables 2.1 and 3.1, some interesting observations on the properties of the hohlraum's flight characteristics can be made. With the hohlraum's outside diameter, d, taken as the system's characteristic length, L; the Reynolds number is sub-100 despite relatively high injection speeds of 200-250 m/s, necessitating laminar flow. Again taking the hohlraum's diameter as the characteristic length and the mean free path calculated from DS2V to be 55.2 and 89.5 μm, Knudsen numbers of 0.0084 and 0.0090 are found

for the old and new TFC respectively. With the accepted transition from the continuum to transition regimes occurring for Knudsen numbers approximately greater than 0.1[1], this flow can traditionally be considered as approaching transition regime but still well within the bounds of being a viscous fluid. Additionally, the target speed is necessitated to be subsonic with Mach numbers of 0.62 and 0.27 for the old and new TFC respectively. The Mach number is reduced despite the injection speed increasing by 50m/s since the temperature increases to 8000 K dramatically raising the local speed of sound.

As shown in Appendix A, the xenon gas within the chamber is not expected to be ionized by the time the target enters, resulting in a constant specific heat for the full temperature range of xenon. When combined with the temperature dependence between viscosity and thermal conductivity based on the Chapman-Enskog theory, a constant Prandtl number is found for the two chamber conditions. As described by DeWitt et al., the Prandtl number is a measure of the relative effectiveness of momentum and energy transport by diffusion in the velocity and thermal boundary layers. For laminar boundary layers, turbulent mixing does not overshadow transport by diffusion while the thermal boundary layer thickness is proportional to the Prandtl number relative to an exponent, as shown in equation 3.1.[2]

$$\frac{\delta}{\delta_t} \propto \mathrm{Pr}^n \tag{3.1}$$

For a Prandtl number near unity (typical of gases), this translates to a viscous and thermal boundary layer that are approximately equal to one another in length, and will be investigated further in Chapter 4.

These conditions do present a number of modeling challenges. Central to these challenges is the extreme temperature variation the target will be exposed to. Initially cryogenic to maintain the DT ice layer, the hohlraum will fly through xenon gas upwards of 8000 K. Proper implantation of transport properties for the full temperature range is vital. In addition, Munsen et al. suggests a flow of a perfect gas may be considered incompressible if the corresponding Mach number is approximately less than 0.3, but may become more important at higher speeds.[3] While this may suggest compressibility is not needed for the new flight conditions, its relative low Mach number is only skewed due to the unusually high local speed of sound of 919 m/s. Thus compressibility for both chamber conditions is advised. To not include compressibility when it is important would be to overestimate the thermal boundary thickness, causing an underestimation in the heat flux to the target.

Non-uniformity of the wall temperature during the transient heating of the hohlraum presents another challenge entirely. While some transient thermal-mechanical analysis of the hohlraum will be looked at in section 4.3, temporal heating analysis is not the focus of this work. However, the half-micron thick LEH window has very little thermal inertia, and is expected to heat up considerably fast. The effect of this changing wall temperature to the local heat transfer coefficient along the surface of the hohlraum will be looked into further in Chapter 4. Other challenges included in the process of

building and running models, refinement studies, and computational limitations will be discussed subsequently in sections 3.4 and 3.5.

3.2: Requirements for a Molecular Description

The conservation equations of mass, momentum and energy are common, and can be derived from either molecular or continuum models. However, these equations by themselves do not form a determinate set unless the heat flux and shear stress are expressed as lower-order functions of the macroscopic properties. The inability of the resulting continuum formulation as modeled by the Navier-Stokes equations to meet this condition imposes the range of validity upon these equations. In other words, when the macroscopic property gradients become so steep that their scale length is on the order of the local mean free path of the fluid, the transport terms within the Navier-Stokes equations begin to fail.[1]

As mentioned previously, Navier-Stokes equations are generally considered valid for Knudsen numbers above 0.1. However, according to Bird this can be misleading if a macroscopic characteristic length, L, is chosen to describe a single *overall* Knudsen number for the entire flow. Instead, this limit can be expressed precisely if a *local* Knusden number is defined with characteristic length equal to the scale length of macroscopic gradients, such as density shown in equation 3.2.

$$L = \frac{\rho}{d\rho/dx} \tag{3.2}$$

According to Bird, errors in the Navier-Stokes results are significant in regions of the flow where the local Knudsen number exceeds 0.1, and must be replaced by a molecular model above 0.2.[1]

In the limit of zero Knudsen number, the transport terms vanish and the Navier-Stokes equations reduce to the inviscid Euler equations. From the continuum standpoint, this equates to isentropic flow while the equivalent molecular description sees this as the velocity distribution function taking on the Maxwellian form everywhere. The opposing limit of infinite Knudsen number is regarded as collisionless, free-molecular flow. The Knudsen number limits on the before-mentioned customary mathematical models are shown in Figure 3.1.[1]

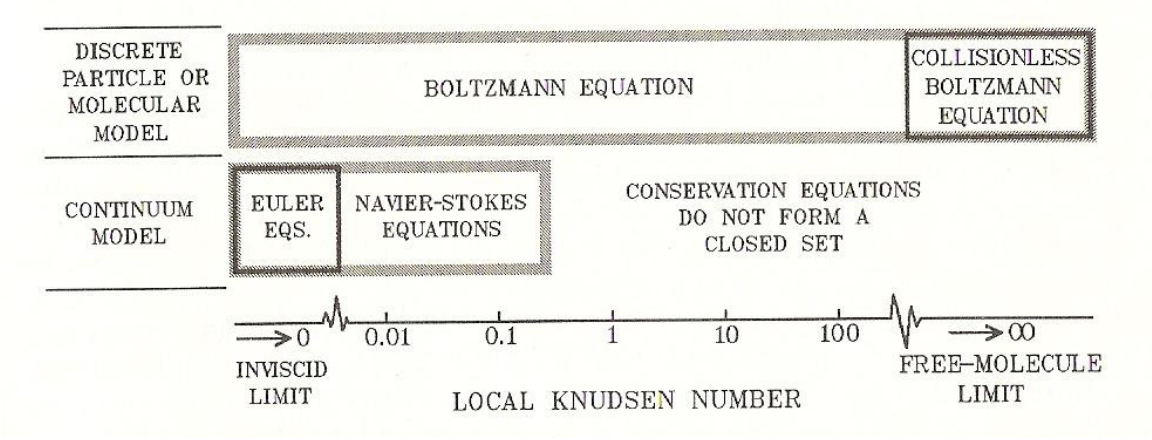

Figure 3.1: The Knudsen Number Limits on the Mathematic Models[1]

In 1952, Chapman and Cowling development of the Chapman-Enskog theory was a significant achievement to classical molecular dynamics. This theory validated the assumption in the Navier-Stokes formulation that shear stresses, heat fluxes, and diffusion velocities are linear functions of the gradients in velocity, temperature, and species concentration. The Chapman-Enskog theory sets the bounds of its validity in its assumption of the velocity distribution function, f, as a small perturbation of the

equilibrium or Maxwellian function, f_o. For the special case of flow in the x-direction whereby gradients only appear in the y-direction, Bird shows the Chapman-Enskog distribution function can be written of the form shown in equation 3.3.

$$f = f_o\left[1 - C\beta v'\left\{3\left(\beta^2 c'^2 - \frac{5}{2}\right)\frac{\lambda}{T}\frac{\partial T}{\partial y} + 4\beta u' s\frac{\lambda}{u_o}\frac{\partial u_o}{\partial y}\right\}\right] \tag{3.3}$$

It is of note the local Knudsen numbers for stream velocity, u, and temperature, T, appear explicitly in equation 3.3 for the terms associated with shear stress and heat flux respectively. These are the first term of the series expansion result of the Chapman-Enskog theory, and hence are only valid when small compared with unity.[1] This confirms the need for having a small Knudsen number when applying Navier-Stokes equations, and will be looked into further for the LIFE heating conditions in Chapter 4.

3.3: Literature Review of Applicable Heating Correlations

An overview of an extensive literature search pertaining to the forced convective heating of objects immersed in high temperature, low Reynolds number flow is presented here. Of primary interest are correlations through use of the Nusselt number (Nu = hL/k, once again with the characteristic length, L, equal to the hohlraum's diameter, d) in obtaining the heat transfer coefficient, h, along the surface of blunt cylinders with its axis parallel to the bulk flow. Unfortunately, very few studies were found to match this particular geometry. To supplement, a select few studies have been included that pertain to spheres in the same regime. Heat transfer studies of this nature are more numerous,

and the ones presented herein have been well matched to the correct Reynolds number, which is not true for all the before-mentioned correlations involving cylinders. A summary of these correlations, along with their resulting position dependent heat transfer coefficients will be presented in Table 4.1 of Chapter 4.

Searching was primarily performed through UCSD's online library catalog in addition to online databases, NASA's Technical Reports Server, Google Scholar, SpringerLink, and LinkingHub. Keywords most often used were of the following: heat transfer, cylinder, longitudinal, low Reynolds, high speed, high temperature, stagnation, blunt bodies and axisymmetric.

As mentioned previously, the main difficulty in finding relevant heat transfer studies is in relation to the cylindrical geometry with its axis parallel to the bulk flow. The vast majority involves cylinders in a cross, two-dimensional flow and thus required extensive sifting to find applicable studies. In addition, most correlations are formulated based on constant fluid properties, where dimensionless variables are calculated at the film temperature (average of the surface and freestream temperatures, as shown in equation 3.4) for modest temperature ranges.[2]

$$T_f = \frac{T_s + T_{\inf}}{2} \tag{3.4}$$

It is widely known transport properties can vary significantly with temperature, and using the average temperature between the two extremes is a method for accounting for this variation through the thermal boundary layer. Again, for modest temperature ranges this

is a reasonable approximation, but becomes increasingly a source of error the larger the temperature range becomes.

Of the correlations found pertaining to cylinders and the hohlraum directly, a recent study by Hadad and Jafarpur in 2008 may be one of the most applicable. Focused on laminar axial air flow, Hadad and Jafarpur use a semi-analytical approach to numerically solve the average heat flux over isothermal bodies with unit aspect ratio including cylinders, cones and spheres. For each case, the authors show grid independence when solving the energy equation simplified for incompressible flow with constant fluid properties. The resulting average Nusselt number for a cylinder valid for the Reynolds range of 1 to 100 is shown in equation 3.5,

$$Nu = 1.5828 + 0.5506\,\mathrm{Re}^{1/2}\,\mathrm{Pr}^{1/3} \tag{3.5}$$

and similarly for a sphere of the Reynolds range 1 to 100,000 in equation 3.6.

$$Nu = 2 + 0.5918\,\mathrm{Re}^{1/2}\,\mathrm{Pr}^{1/3} \tag{3.6}$$

It is of note that the solution is comprised of both the conduction limit (verified to be 2 for a sphere in infinite medium by Dewitt et al.[2]) in addition to the convective laminar boundary layer solution for heat transfer. Hadad and Jafarpur make note that excellent agreement was found between their correlation and available data from a number of sources.[4] As discussed before, the fact the flow is considered incompressible suggests

the average heat transfer may be underestimated due to an overestimation in the thermal boundary layer thickness.

An older correlation from Belov and Terpigor'ev in 1969 may be of some use in regards to heat transfer at the forward stagnation point. Their study was motivated by trying to account for discrepancies in theory and experimental data for heat transfer at the stagnation point of blunt bodies subjected to subsonic and supersonic jets through turbulence in the freestream. However, within their analytical derivation lies the case of heat transfer near the stagnation point for a subsonic jet with no turbulence, thus matching LIFE's target flight conditions, and is subsequently described in equation 3.7.

$$Nu = 0.763\,\mathrm{Re}^{0.5}\,\mathrm{Pr}^{0.4} \tag{3.7}$$

Restrictions of Reynolds number was not placed upon this correlation.[5] Belov and Terpigor'ev also do not explicitly state a reference temperature for which these dimensionless variables are to be calculated, and thus Reynolds and Prandtl numbers will be calculated at the film temperature as is generally done. Once again, this derivation was based on the assumption of incompressible flow, and as such may be underestimating the expected heat transfer for LIFE's target flight conditions.

In 1987, Kang and Sparrow conducted a series of experiments measuring the heat transfer along the longitudinal surface of a cylinder whose axis was parallel to the bulk flow. Their intent was to look at differences in heat transfer of open- and closed-bore cylinders, with the close-bore being applicable to the LIFE.2 target. The maximum heat

transfer along the longitudinal surface was found for the closed-bore cylinder as described in equation 3.8.

$$Nu = 0.202\,\mathrm{Re}^{2/3}\,\mathrm{Pr}^{1/3} \tag{3.8}$$

All thermophysical data for this correlation is calculated at the freestream temperature. The location and magnitude of maximum heat transfer was found dependent on the configuration. For all cases, the local Nusselt along the longitudinal surface of the cylinder increased initially, obtained a maximum, and then decreased monotonically. Kang and Sparrow suggest this is indicative of a separation bubble near the leading edge followed by the post-reattachment boundary layer development. The suggested applicability range is modestly higher than for the LIFE chamber conditions, with Reynolds ranged from 7,700 to 47,000.[6]

In 1964, Sogin published a report regarding experimental measurements of heat transfer to the rear of bluff obstacles to a low speed airstream. These measurements were taken using a flat-plate strip in two-dimensional flow. For an angle of attack of 90^{o}, the heat transfer was found constant along the entire back surface of the plate, and is represented by equation 3.9.

$$Nu = 0.20\,\mathrm{Re}^{2/3} \tag{3.9}$$

Viscosity and thermal conductivity for this correlation is to be calculated at the film temperature, with the density found at the film temperature and stagnation pressure.

However, this correlation is only mildly applicable to the LIFE target conditions, with the Reynolds number ranged from 100,000 to 440,000[7], and is included because it was the only study found that is similar to the heating conditions along the leeward window surface.

In addition to the work by Hadad and Jafarpur presented earlier, correlations relating to spheres in similar heating conditions to the LIFE target are numerous. Whitaker in 1972 suggested an encompassing form of a sphere's average Nusselt number, and is shown in equation 3.10.

$$Nu = 2 + \left(0.4\,\mathrm{Re}^{1/2} + 0.06\,\mathrm{Re}^{2/3}\right)\mathrm{Pr}^{0.4}\left(\frac{\mu}{\mu_s}\right)^{1/4} \tag{3.10}$$

All thermophysical data is calculated at the free stream temperature, except for μ_s which corresponds to the viscosity of the fluid at the surface temperature of the sphere. This form of the Nusselt number combines previous work that had been done in relation to heat transfer from the laminar boundary layer and wake regions, and thus is suggested to be valid for a wide range of heating conditions:[8]

$$0.71 \leq \mathrm{Pr} \leq 380$$

$$3.5 \leq \mathrm{Re} \leq 7.6 \times 10^4$$

$$1.0 \leq (\mu/\mu_s) \leq 3.2$$

The Prandtl number for xenon remains constant at 0.67, and thus is slightly outside of its suggested range. In addition, for the old TFC where the free stream is 1000 K and the wall is held at 150 K, a viscosity ratio of 5.4 is obtained, and does not fall within the accepted bounds until a wall temperature of 250 K is used. In relation to the values calculated in Table 4.1, a Prandtl number of 0.71 increases the heat transfer coefficient, h, by 2% while increasing the wall temperature to 250 K reduced h by 9%. Thus additional uncertainty in using this equation slightly outside of its bounds is roughly 7%.

In 1961, Cohen published a report finding an analytical solution that included the heat transfer at the stagnation point of an axisymmetric body. This work was done at the Langley Research Center in support of NASA space reentry vehicles. Through the use of a similarity solution of the boundary-layer equations for compressible flow, while using the thermophysical data of air, Cohen suggests a Nusselt number described in equation 3.11.

$$Nu = 0.767\,\mathrm{Re}^{0.5}\,\mathrm{Pr}^{0.4}\left(\frac{\mu_e \rho_e}{\mu \rho}\right)^{0.43} \tag{3.11}$$

All thermophysical data in equation 3.11 are calculated at the surface or 'wall' temperature of the blunt object, except viscosity and density with subscripts 'e', corresponding the values 'external' to the boundary layer or upstream values. As with Whitaker, this correlation is applicable through a wide range of heating conditions:

$$v < 9{,}144 \text{ m/s}$$

$$10^{-4} \text{ atm} < \text{stagnation pressure, } p_{st} < 10^{2} \text{ atm}$$

$$300 \text{ K} < T_w < 1722 \text{ K}$$

The velocity and temperature upper bounds come from the freestream total enthalpy limit where air begins to ionize. No information is provided for the lower bound of wall temperature, but increasing the temperature to 300 K had negligible effects on the final heat transfer coefficient. Also of note, Cohen shows equation 3.11 is only slightly dependent on gas properties. For incompressible flow with constant fluid properties, the coefficient and exponent change to 0.763 and 0.5 respectively. In addition, corresponding values of 0.768 and 0.4 were obtained for equilibrium dissociated air with unit Lewis number and for a perfect gas with constant specific heat. The later of these coefficients are reflected in equation 3.12 to better match LIFE's heating conditions.[9]

$$Nu = 0.768\,\mathrm{Re}^{0.5}\,\mathrm{Pr}^{0.4}\left(\frac{\mu_e \rho_e}{\mu \rho}\right)^{0.4} \tag{3.12}$$

This change is reflected in Table 4.1, and resulted in a slight increase in the heat transfer coefficient of 1.5% when compared to using equation 3.11. It is of note a few assumptions have been made in calculating the density at the wall of equations 3.11 and 3.12. Starting from upstream, the xenon gas was assumed to stagnate isentropically, where it was then cooled to the wall temperature via the ideal gas law.

The Nusselt and Reynolds numbers in equations 3.11 and 3.12 are defined as a function of position, x, along the blunt body starting at the forward stagnation point: Nu =

hx/k_w, $Re = \rho_w u_e x/\mu_w$. The coefficient 'u_e' refers to the velocity perpendicular to the body of revolution external to the boundary layer.[9] It is well documented that near the stagnation point, this velocity reduces to a linear function of position of the form $u_e = Cx$, where C is a constant known as the local velocity gradient external to the boundary layer at the stagnation point.[9,10] As described by Reshotko and Cohen in the 1955 National Advisory Committee for Aeronautics technical note 3513, "because of this linear velocity relation, the ratio $Nu/\sqrt{Re}$ at the stagnation point ($x = 0$) is finite, although the individual Nu and Re numbers individually become zero at $x = 0$."[11] It is recommended that in the absence of experimental data, a reasonable estimate of the local velocity gradient can be made from potential flow relations,[11] found to be $3V/d$ for a sphere, where V is the stream velocity and d is the diameter of the sphere.[10,11]

3.4: Direct Simulation Monte Carlo and DS2V

A full description of the direct simulation Monte Carlo (DSMC) technique is presented by Bird (1994)[1], but in overview DSMC models real gases through the simulation of thousands or millions of representative molecules. The position and velocity of these molecules are modified with simulated time as they undergo representative collisions. In stark contrast to traditional computational fluid dynamic codes in which solutions are sought that model the flow as a continuum, DSMC directly simulates these physical processes. DSMC is very computationally demanding, and is only feasible as the gas density becomes adequately low. However, as described in section 3.2, at these low densities DSMC becomes necessary in that the Navier-Stokes equations begin to fail in providing an adequate representative model.[1,12]

In regimes where DSMC and CFD are both applicable, DSMC presents a number of unique advantages. First, the flow is unsteady with physical time, and if steady solutions are obtained, they are done so through large simulation times of unsteady flow. Secondly, the DSMC method does not require initial conditions or an iterative process of convergence to obtain its final solution, and hence has no numerical instabilities! For time average steady flows, statistical scatter will reduce as the sample increases, but the typical definition of "convergence" is not a proper description of this process. Finally, although it has no consequence to the LIFE heating conditions, DSMC has the ability to include effects such as non-equilibrium chemistry through additional complexity of the molecular model.[1,12]

Inherent to the DSMC processes are three computational approximations that can lead to error. These include the ratio of the number of simulated to real molecules, the time step in which the molecular motion and collision are uncoupled, and the size of the cell and sub-cell in physical space. Bird addresses these issues, setting forth the following two DSMC criteria:[1]

- "Linear dimensions of the cells should be small in comparison with the scale length of the macroscopic flow gradients in the direction in which the dimension is measured. In regions with large macroscopic gradients, this generally means that the cell dimension should be of the order of one third the local mean free path."
- "The time step should be much less than the local mean collision time."

Bird has implemented these criterions first hand in the creation of many DSMC programs, including the program used in this work, DS2V. Intended for ease of use for

non-experts, DS2V has become a well established visual DSMC program suited for two dimensional and axially symmetric flows. It is capable of both steady and unsteady flows, and is freely distributed via Bird's website.[13] It is of note the only computational parameter set by the user is the initial number of megabytes to be used for storage. All other parameters are automatically set by the program.[12]

Bird places some responsibility on the user in the proper implementation of DS2V. A parameter defined as the mean separation between collision partners to the local mean free path (m.c.s./m.f.p.) is tracked everywhere in the flow field, and must be much smaller than 1 (suggested value of 0.2) everywhere in the domain to satisfy the first criterion. Automatically built into the program's logic is a variable time-step calculated to be one-third the local mean collision time, automatically satisfying the second criterion.[12]

DS2V simulations are defined through a simple user graphical interface where inputs for computational parameters, reference streams and boundaries are available. With the aid of the simple domain schematic of Figure 3.2, a typical DS2V simulation used to look at the external forced convective heating of the hohlraum was constructed as follows.

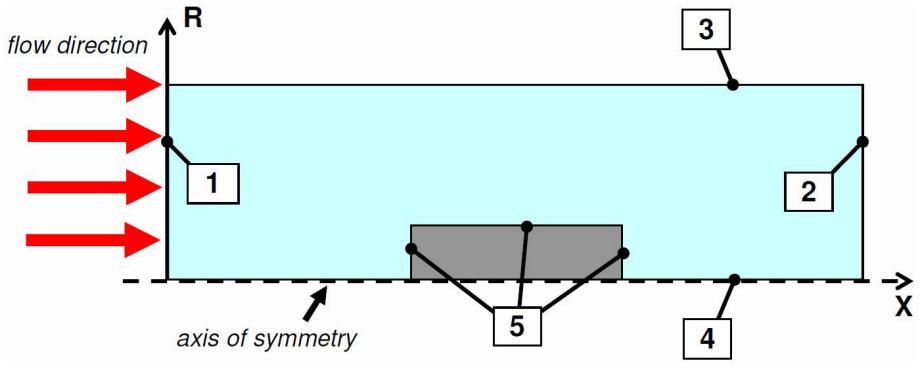

Figure 3.2: DS2V Domain Schematic

Upon entering the graphical interface, the simulated flow was first designated to be axially symmetric and to include radial weighting factors. These weighting factors help to evenly distribute particles throughout the domain, and are recommended by Bird in axial symmetric flows.[1,12] Upon making this choice, the 'minimum y' boundary (boundary 4 in Figure 3.2) was forced to be the default axis of symmetry. From here the flow was assumed to be traveling in the positive x-direction, and as such boundaries 1 and 3 of Figure 3.2 was designated as an interface with the stream or reference gas. Finally, boundary 2 was set by holding the pressure fixed, as is typically done at the outflow of simulations such as these. The placement of these boundaries, and hence the domain size were also set here. The influence of these boundaries were studied extensively, but the 'default' domain sizes will be set to be 0.04 x 0.012 m for the Old TFC and 0.055 x 0.015 m for the New TFC in the 'X' and 'R' directions respectively.

The reference gas designated earlier on boundaries 1 and 3 of Figure 3.2 must now be defined. DS2V is capable of including multiple species of a gas mixture, but only the number density, temperature and velocity of a single species is needed for this work. From Table 2.1, these conditions were set to be 2.00×10^{22} 1/m^3, 1000 K, and 200 m/s in the positive x-direction for the Old TFC, and 2.75×10^{22} 1/m^3, 8000 K, and 250 m/s for the New TFC. The type of gas was then specified to be xenon, which conveniently is a standard input. The temperature dependent viscosity is handled through a power law, and is set to a default reference temperature of 273 K for all gas species. For the updated values to these parameters, refer to Table A.1 of Appendix A.

With the gas fully defined, all that remains to complete the setup is the target surface specification. This is a simple procedure where the target was first drawn

centered on the axis of symmetry, as shown in boundary 5 of Figure 3.2. For this particular flow setup, the boundary must be drawn counterclockwise to be properly recognized by DS2V. Each of the three segments where chosen to include 10 property intervals from which surface properties, such as heat flux and pressure, are measured. Most important to these surfaces, the walls were held at a fixed temperature of 150 K (as explained in section A.1) with assumed diffuse reflection and full accommodation to the surface temperature. In essence this is the worse case of heat transfer for the targets. Molecules impinging upon the surface of the hohlraum will transfer all of their energy to the surface and be diffusely reflected at the surface temperature.

The most serious problem encountered in running DS2V was a radial bias in flow properties caused by the default setting of nearest-neighbor collisions. The source code for DS2V is not publically available, and as thus only conjecture can be offered to explain this occurrence. Turning off this feature was not intuitive, and required a trial-by-error approach within the advanced user settings.

Another serious problem encountered while running DS2V was obtaining an adequate m.c.s./m.f.p ratio to satisfy Bird's first DSMC criterion. This problem is due to the extreme drop in temperature of the molecules near the surface of the hohlraum. This effect is accompanied by a drastic drop in the local mean free path, increasing in the m.c.s./m.f.p. ratio near the target's surface. These effects, along with refinement studies will be discussed in more detail in Chapter 4, but in general all that could be done to counter this problem was to increase the initial memory allocation for the run, shrink the size of the domain or increase the surface temperature. However, by doing so the run times required for the flow to fully develop increased substantially.

3.5: Computational Fluid Dynamics, ANSYS and COMSOL

Computational fluid dynamics (CFD) is a well established division of fluid dynamics that uses numerical methods and algorithms to find solutions to complex fluid flows. At the basis of almost all CFD codes are the Navier-Stokes equations, defining any single-phase fluid flow based on the conservation of mass, momentum and energy along with the assumption of continuum flow. For most engineering applications, CFD has become the standard of modern fluid analysis.

Of the many CFD codes available, all apply the same simple methodology in their use. The geometry, or physical bounds of the problem, must first be defined, after which the volume occupied by the fluid is discretized into a number of finite cells. It is then up to the user to define the physics included with the flow, for instance entropy and radiation if applicable. Boundary conditions must then be characterized for every surface to describe the fluid behavior and the properties of the boundaries of the problem. The simulation can then be started, where the partial differential equations that govern the flow are solved iteratively as a steady-state or transient process. Finally, a postprocessor is used for the analysis and visualization of the resulting fluid flow solution.

As discussed in Section 3.2, CFD and the Navier-Stokes equations should not be used when the local macroscopic property gradients become so steep that their scale length is on the order of the local mean free path of the fluid. This has traditionally required an overall Knudsen number to be less than 0.1. However, as described previously in section 3.2, Bird argues the limit can be expressed precisely if a local Knudsen number is defined with characteristic length equal to the scale length of macroscopic gradients, such as density defined previously in equation 3.2.[1] In addition, it

is well accepted within academia and industry circles that a CFD simulation can only be considered accurate when the final solution does not change due proximity of the boundaries and the density of the mesh. Refinement studies of this nature will be discussed further in Chapter 4.

By finding a solution that mathematically describes the flow, versus modeling the atomic physical interactions, computational fluid dynamics is typically much more efficient in finding solutions. This has undoubtedly been a driving force for its popularity within industrial and academia circles. However, along with this widespread accessibility and use comes inexperience in modeling, resulting in the main disadvantage in using CFD. The quality of the solution often depends on the ability of the user. Models may be set up, and solutions obtained that appear reasonable on the surface, all the while being incomplete and inaccurate. This necessitates once again refinement and validation studies to help show the accuracy of the final solution.

The well established and commercially available CFD code ANSYS CFX was used within this analysis via the ANSYS Workbench platform in modeling the heat transfer from the ambient xenon gas to the hohlraum in the LIFE chamber. With the aid of the simple domain schematic of Figure 3.3, a typical ANSYS simulation used within this work was constructed as follows.

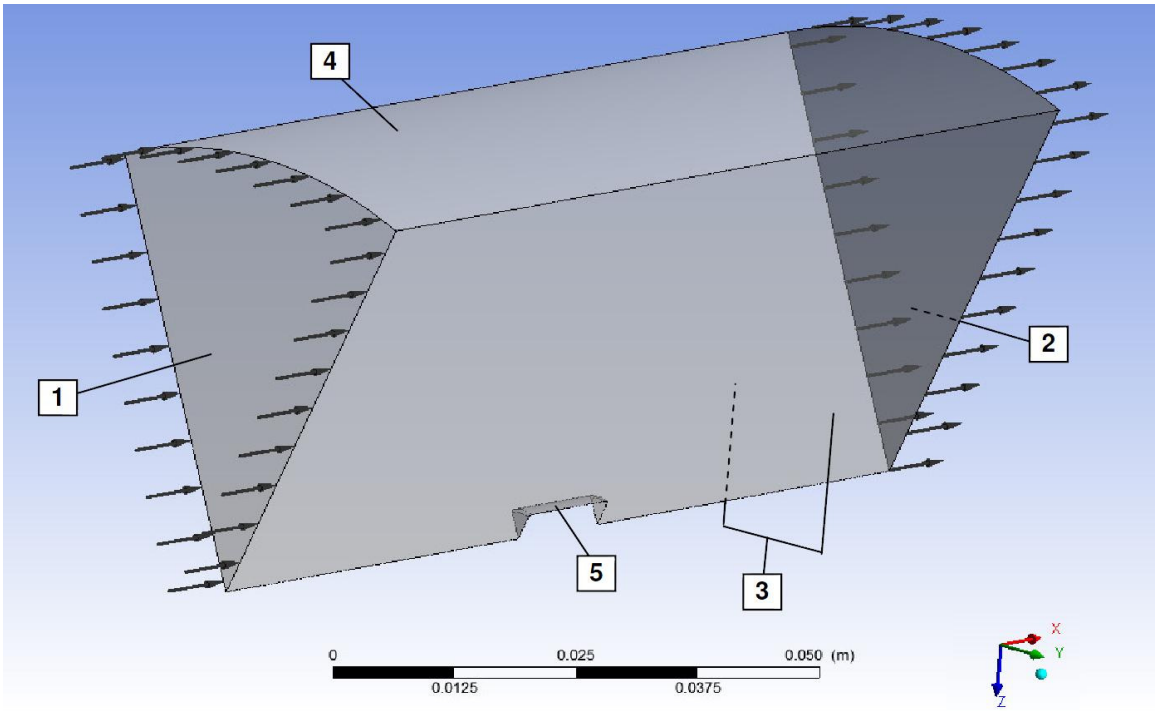

Figure 3.3: ANSYS Domain Schematic

Using Pro Engineer Wildfire 5.0, symmetry of the target was taken advantage of in making a 45 degree wedge 20 cm in length and 5 cm in radius, as shown in Figure 3.3. The target was then cut on the angled surface of the wedge, centered about its length with rounded corners 10% of the NIF-like hohlraum radius (0.33 cm) to avoid singularities within the flow field. This model was then saved as an igs file, where it could easily be imported into the ANSYS Workbench model definition. Using ANSYS CFX Mesh generator, the model was then finely discretized into many elements, with specific refinement along the axis of symmetry and the hohlraum's surface and are summarized in Table 3.2. It is of note that a special 'inflation' layer was placed along the surface of the hohlraum. This feature stacks a series of 4 to 5 elements very close together on the surface they are applied to better capture the fluid-surface interactions. In addition, the maximum spacing along the surface of the hohlraum in addition to the axis of symmetry

was set to 100 μm, less than double the free stream mean free path of either flow described in Section 3.1.

Table 3.2: ANSYS CFX Mesh Settings

Default Body Spacing (entire domain)
max spacing = 0.001 m
Default Face Spacing (entire domain)
min edge length = 0.0001 m max edge length = 0.005 m
Face Spacing (hohlraum wall)
min edge length = 0.00005 m max edge length = 0.0001 m
Edge Spacing (axis of symmetry)
constant edge length = 0.0001 m expansion factor = 1.2
Inflation (hohlraum wall)
max thickness = 0.005 m

With the mesh now complete, ANSYS CFX-Pre can now be accessed to define the fluid and boundary conditions. A user defined gaseous xenon was first created that obeys the ideal gas law with a molecular mass of 131.293 g/mol, and constant specific heat at constant pressure of 158 J/kg·K. In order to maintain consistency between DSMC and CFD modeling techniques, the same temperature dependent transport properties employed by DS2V (see Appendix A, Table A.1) was also used for ANSYS. The domain was then set to reference this gaseous xenon and assumed to be a laminar, continuous fluid. High speed energy effects were included through selection of the "total energy" heat transfer option along with selecting the optional inclusion of the viscous work term in the energy equation.

Assuming the flow travels in the positive x-direction, the inflow was set to surface 1 (shown in Figure 3.3) as a subsonic flow with normal speed and static temperature of

200 m/s and 1000 K for the old TFC and 250 m/s and 8000 K for the new TFC. The outlet was then forced to be designated as surface 2, with an average static pressure held at 276 and 3037 Pa for the old and new conditions. The two sides of surface 3 were simply defined to be symmetrical, after which the outer radial wall of surface 4 was classified as an adiabatic, free-slip wall. The final 5th surface belongs to the hohlraum's wall, and was defined to be non-slip held at a temperature of 150 K.

Running ANSYS presented a pair of difficulties, the second of which could not be resolved. The first problem occurred in meshing along the axis of symmetry or the angled surface of the wedge. Non-uniform meshes and misleading solutions were obtained when a thinner wedge of 5 degrees was used. Switching to a 45 degree wedge allowed the inflation boundary to be nicely produced right up to the axis of symmetry, allowing the tetrahedral elements automatically generated by ANSYS CFX Mesh to be much more uniform

The second problem occurred when simulating the LIFE.2 target in the new target flight conditions. A solution could not be obtained when holding the wall at 150 K, as wished. With the ambient gas temperature being 8000 K, this would have constituted more than a 53x decrease in temperature, resulting in the solution to become unstable and fail to converge. In fact, raising the temperature to 1000 K and 1500 K also did not yield a solution. Not until the next simulation when the wall was set at 2000 K was convergence obtained.

The final phase of analysis consists of the transient heating of the helium internal to the hohlraum and was performed using the multi physics based code COMSOL. While ANSYS is far superior to COMSOL in modeling fluid flow, this work was

performed in collaboration with the LIFE team at LLNL, and was chosen to duplicate and expand on the work already performed, all of which had been done previously with COMSOL. Specifically, the intent of this work was to include spinning along with target heating, and to understand possible swirling effects of helium acting as a heat sink for heating/cooling of the window and fuel capsule as a function of the heat transfer coefficient along the LEH windows. Repeating this work for both target geometries was a simple extension that added another insightful dimension to the analysis. Nevertheless, with the aid of the domain schematic of Figure 3.4, a typical COMSOL simulation used within this work was constructed as follows.

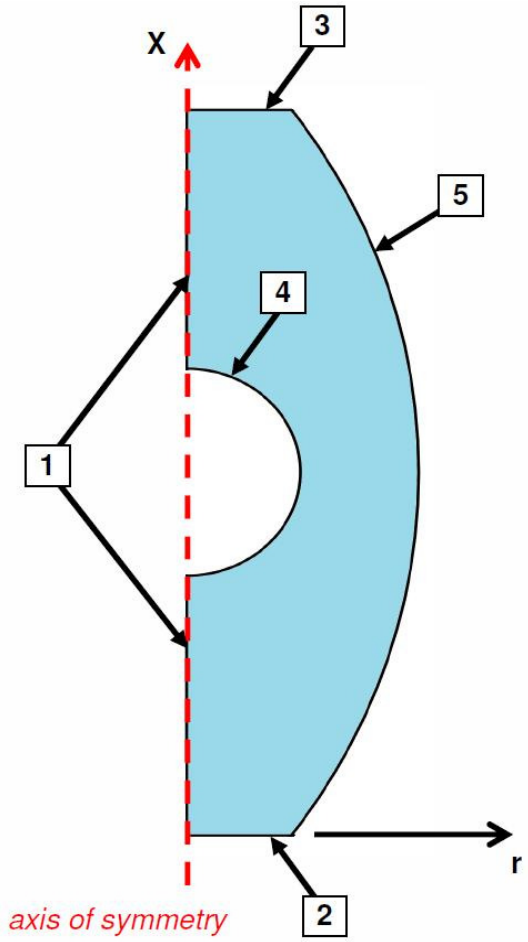

Figure 3.4: COMSOL Domain Schematic

When starting COMSOL, separate physics modules of fluid mechanics and heat transferred were coupled together to be simulated within a two-dimensional axially symmetric domain. Depicted in blue in Figure 3.4, this domain was drawn using the tools within the model definition portion of the COMSOL program and set to an initial pressure of 41,500 Pa and temperature of17 K, representing the new target flight conditions. Only a single domain was defined since this was the first analysis of its kind to couple heat transfer and fluid mechanics in the heating of the hohlraum's interior, and was desired to be as simple as possible. In addition, heat sources were only planned to be placed along the LEH windows (surfaces 2 and 3 of Figure 3.4), and since the window thickness is approximately four orders of magnitude smaller than the hohlraum's diameter or length, it could not be meshed along side the hohlraum's internal helium with COMSOL. Therefore, a 'virtual' LEH window will be assumed that offers no thermal resistance in the heating of the internal helium. A rudimentary mesh was then created for this domain using COMSOL's internal mesh generator, with the final elements varying in size approximately 40-400 μm.

With the mesh specified, thermal and viscous boundary conditions were then specified. The effects of spinning were included by defining the angular velocity a function of its local radial distance for both the domain and non-slip boundaries. To do this, the local circumferential distance was multiplied by the spin rate of 15,000 RPM (250 rev/s), as shown in equation 3.13.

$$u_{\varphi} = (2\pi r)\left(250\frac{rev}{s}\right) = 1570.8r\left[\frac{1}{s}\right] \tag{3.13}$$

Note, ‘r’ is a global variable automatically set by COMSOL in choosing a two-dimensional axially symmetric flow, and is measured from the dashed red line as shown in Figure 3.4. Heat transfer of the LEH windows will be defined through surfaces 2 and 3 by an external heat transfer coefficient (varied from 1 to 40 $W/m^2 \cdot K$ in 1 $W/m^2 \cdot K$ increments) with a reference temperature of 8000 K. To look at the effect of a varying heat transfer coefficient independent of all other variables, surfaces 1, 4 and 5 will be assumed adiabatic. Finally, the transient solution was set for a run time of 24 ms broken down into approximately 100 intervals by having time steps equal to 250 μs.

Interestingly, the difficulties in running COMSOL closely mirrored those for ANSYS, only more accentuated. The mesh generator employed by COMSOL is very poor. Element constraints could not be placed within the domain, along surfaces or edges as was possible with ANSYS, and in general the user has very little control in mesh refinement. Fortunately the geometry was simple enough a straightforward medium-density mesh sufficed, but further refinements proved difficult for the COMSOL solver to handle.

COMSOL also had difficulty in converging to a solution when large heat fluxes were driven through the LEH windows. This was overcome by a simple, yet tedious procedure of stepping the solution to its final boundary constraints. More specifically, solutions for less intense heat fluxes were used as the starting point for more forceful heating simulations, placing less strain on the COMSOL solver.

Chapter 3, in part, contains materials submitted to Transactions of Fusion Science and Technology, June 2011. Holdener, D. S., Tillack, M. S., Wang, X. R., 2011. The thesis author was the primary investigator and author of this paper.

References:

1. Bird, G. A. *Molecular Gas Dynamics and the Direct Simulation of Gas Flows*. Oxford: Clarendon, 1994, pp. 2-3, 208-216.

2. Incropera, Frank P., David P. DeWitt, Theodore L. Bergman, and Adrienne S. Lavine. *Introduction to Heat Transfer.* 5th ed. Hoboken NJ: Wiley, 2007: pp. 363, 369, 410.

3. Munson, Bruce Roy, Donald F. Young, and Theodore H. Okiishi. *Fundamentals of Fluid Mechanics*. 5th ed. Hoboken, NJ: J. Wiley & Sons, 2006: pp. 130.

4. Hadad, Yaser, and Khosrow Jafarpur. "Laminar Forced Convection Heat Transfer from Isothermal Bodies with Unit Aspect Ratio." Proc. of 6th IASME/WSEAS International Conference on HEAT TRANSFER, THERMAL ENGINEERING and ENVIRONMENT (HTE'08), Greece, Rhodes. August 20-22, 2008.

5. Belov, I. A., and V. S. Terpigor'ev. "Turbulence in Calculations of Heat Transfer at the Stagnation Point of a Jet Interacting Normally with a Planar Obstacle." *Inzhenerno-Fizicheskii Zhurnal* 17.6 (1969): 1106-109.

6. Kang, S. S., and E. M. Sparrow. "Heat Transfer From an Open- or Closed-Bore Cylinder Situated Longitudinal to a Freestream." *Transaction of the ASME. Journal of Heat Transfer* 109.2 (1987): 314-20. Print.

7. Sogin, H. H. "A Summary of Experiments on Local Heat Transfer From the Rear of Bluff Obstacles to a Low Speed Airstream." *Transactions of the ASME. Journal of Heat Transfer* 86 (1964): 200-02. Print.

8. Whitaker, Stephan. "Forced Convection Heat Transfer Correlations for Flow in Pipes, Past Flat Plates, Single Cylinders, Single Spheres, and for Flow in Packed Beds and Tube Bundles." *American Institute of Chemical Engineers* 18.2 (1972): 361-71.

9. Cohen, Nathaniel B. "*Boundary-Layer Similiar Solutions and Correlation Equations for Laminar Heat-Transfer Distribution in Equilibrium Air at*

Velocities up to 41,100 Feet Per Second." Langely Research Center, Langely Air Force Base, VA. NASA Technical Report R-118, 1961.

10. Schlichting, Hermann. *Boundary Layer Theory.* 4th ed. New York: McGraw-Hill, 1960: pp. 185-190.

11. Reshotoko, Eli and Clarence B. Cohen. "Heat Transfer at the Forward Stagnation Point of Blunt Bodies." National Advisory Committee for Aeronautics, Lewis Flight Propulsion Laboratory, Cleveland, Ohio. Technical note 3513, July 1955.

12. *Visual DSMC Program for Two-Dimensional and Axially Symmetric Flows - The DS2V Program User's Guide*. Rep. Version 3.8. Sydney, Austrailia: G.A.B. Consulting Pty, October 2006.

13. *DSMC Resources from Graeme Bird*. Web. 21 Apr. 2011. <http://www.gab.com.au/>.

Chapter 4:

Results and Analysis

4.1: Heat Transfer Correlations

A summary of the literature search and resulting heat transfer correlations covered in section 3.3 are presented in Tables 4.1. Studies dealing with flow around a cylinder with the bulk flow parallel to its axis of rotation are of greatest interest and presented first. A select few studies involving spheres in similar heating conditions to the original flight conditions have also been included as a means of comparison in the subsequent sections. All of these heat transfer correlations are represented graphically next to simulated heat fluxes from DS2V and ANSYS in Figures 4.8, 4.9 and 4.10.

Close inspection of the summarized correlations reveal stark similarities in the scaling of the dimensionless Reynolds and Prandtl numbers for these heating conditions. The results of Belov and Terpigor'ev are identical in form to Cohen despite their diverse background in relating the heat transfer at the stagnation point of blunt bodies. In addition, semi-empirical results for the average heat transfer from cylindrical and spherical bodies presented by Hadad and Jafarpur vary in Prandl number to these correlations by less than 0.07.

Table 4.1: Summary of Heat Transfer Correlations

	Eq.	Location	Conditions
Cylinder:			
Hadad and Jafarpur (2008)			
$Nu = 1.5828 + 0.5506\ Re^{1/2}Pr^{1/3}$	(5)	average	$1 \leq Re \leq 100$
Belov and Terpigor'ev (1969)			
$Nu = 0.763\ Re^{0.5}Pr^{0.4}$	(7)	sagnation point	laminar, subsonic jet with no turbulence
Kang and Sparrow (1987)			
$Nu = 0.202\ Re^{2/3}Pr^{1/3}$	(8)	longitudinal max	$7{,}700 \leq Re \leq 47{,}000$
Sogin (1964)			
$Nu = 0.20\ Re^{2/3}$	(9)	leeward edge	$100{,}000 < Re < 440{,}000$
Sphere:			
Hadad and Jafarpur (2008)			
$Nu = 2 + 0.5918\ Re^{1/2}Pr^{1/3}$	(6)	average	$1 \leq Re \leq 100{,}000$
Whitaker (1972)			
$Nu = 2 + (0.4\ Re_D^{1/2} + 0.06\ Re_D^{2/3})Pr^{0.4}(\mu/\mu_s)^{1/4}$	(10)	average	$0.71 \leq Pr \leq 380$ $3.5 \leq Re \leq 7.6 \times 10^4$ $1.0 \leq (\mu/\mu_s) \leq 3.2$
Cohen (1961)			
$Nu = 0.768\ Re^{0.5}Pr^{0.4}\ (\mu_e\rho_e/\mu\rho)^{0.4}$	(12)	Stagnation point	$v < 9144$ m/s 10^{-4} atm $< p_{st} < 10^2$ atm 300 K $< T_w <$ 1722 K

Table 4.1: Summary of Heat Transfer Correlations, Continued

Cylinder:		*Heat Transfer Coefficient, h ($W/m^2 \cdot K$)*	
	Eq.	Old TFC	New TFC
Hadad and Jafarpur (2008)			
$Nu = 1.5828 + 0.5506\ Re^{1/2}Pr^{1/3}$	(5)	10.8	23.8
Belov and Terpigor'ev (1969)			
$Nu = 0.763\ Re^{0.5}Pr^{0.4}$	(7)	11.4	24.0
Kang and Sparrow (1987)			
$Nu = 0.202\ Re^{2/3}Pr^{1/3}$	(8)	7.1	13.9
Sogin (1964)			
$Nu = 0.20\ Re^{2/3}$	(9)	13.2	25.3
Sphere:			
Hadad and Jafarpur (2008)			
$Nu = 2 + 0.5918\ Re^{1/2}Pr^{1/3}$	(6)	12.1	16.8
Whitaker (1972)			
$Nu = 2 + (0.4\ Re_D^{1/2} + 0.06\ Re_D^{2/3})Pr^{0.4}(\mu/\mu_s)^{1/4}$	(10)	19.7	N/A
Cohen (1961)			
$Nu = 0.768\ Re^{0.5}Pr^{0.4}\ (\mu_e\rho_e/\mu\rho)^{0.4}$	(12)	25.7	N/A

The consistency in the form of these correlations allows heating trends to be predicted through changes in the components that make up the dimensionless variables. These trends should only be considered as general and approximate, valid only if they continue to meet their suggested range of use as described in Table 4.1. Nevertheless, using expressions of Reynolds ($Re = \rho vL/\mu$) and Prandtl ($Pr = c_p\mu/k$) numbers with exponents of 0.5 and 0.4 respectively, the general empirical form of the Nusselt number may be written as shown in equation 4.1.

$$\left(\frac{hL}{k}\right) = C\left(\frac{\rho vL}{\mu}\right)^{0.5}\left(\frac{c_p\mu}{k}\right)^{0.4} \tag{4.1}$$

With 'C' being a constant empirically found for a given geometrical setup and heating conditions, and the specific heat, c_p, being constant for the full temperature range of LIFE's conditions (see Appendix A), the heat transfer coefficient, h, may be written as being proportional of the form shown in equation 4.2.

$$h \propto \left(\frac{\rho vL}{\mu}\right)^{0.5} \frac{k^{0.6}}{\mu^{0.1}} \tag{4.2}$$

The first term in equation 4.2 shows a positive trend in the heat transfer coefficient for increases in gas density and target speed to the one-half power. Reduction of either of these variables will intuitively reduce the heat transfer coefficient. However, reduction of the velocity will not decrease the overall heat load exposed to the target. For instance, if the target speed was doubled from the old TFC of 200 m/s to 400 m/s, the heat transfer coefficient will increase by approximately 71% but the flight time will be cut in half. It is therefore advisable to have the target travel as fast as possible that can still be accurately tracked and engaged and does not cause flight instabilities. Conversely, the chamber density is based on design criteria of ion and x-ray attenuation, and will likely not be changed greatly due to target heating.

Also within this first term of equation 4.2 is the inverse trend of heating due to increases in the characteristic length to the one-half power. This suggests target heating

will decrease as the scale of the target is enlarged. The target size and shape is based on target physics and efficient coupling of the driver energy to the fuel capsule, and thus not a likely to change due to convective heating. However, this trend can be more applicable when thinking of localized heating near the stagnation point as presented by Cohen. The 'local velocity gradient' described previously in section 3.3 is Cohen's way of accounting for this dependence on shape. Simply increasing the scale of the target will have the same inverse heating trend, but further reductions in the 'local velocity gradient' can be made if the leading edge is made to be more blunt. In essence, this constitutes 'trapping' air near the stagnation point, reducing the effectiveness of convective heat trasfer.

Heat transfer trends dealing with the final two coefficients of equation 4.2 are both dependent on non-linear changes in thermal conductivity and viscosity with temperature, and thus will be grouped together. As was done for the majority of heating correlations in Table 4.1, their variation with temperature through the thermal boundary layer will be approximated from their calculation at the appropriate film temperature. In addition, since both transport properties share the same temperature dependence (see Appendix A), they may be thought of as the same variable and combined when calculating the relative heat transfer coefficient, such as $h \sim k^{0.5}$.

The first heating scenario is taken to be for a constant fluid or chamber gas temperature with an ever increasing wall temperature. For the old TFC, the heat transfer coefficient rose 30% when varying the wall from 0 to 1000 K while holding the chamber gas at 1000 K. Similarly for the new TFC, an increase of 25% was seen when varying the wall from 0 to 8000 K while holding the chamber gas at 8000 K. These calculations

are shown in Table 4.2 for the temperature extremes and graphically in Figure 4.1 for the full temperature range.

Table 4.2: Heat Transfer Scaling vs. Wall Temperature

Old TFC:

			(calculated @ T_f)			
T_{ref} (K)	T_w (K)	T_f (K)	k (mW/m·K)	μ (μPa·s)	$h \sim k^{0.6}/\mu^{0.1}$	$h \sim k^{0.5}$
1000	0	500	8.8	37.0	2.57	2.96
1000	1000	1000	14.9	62.9	3.35	3.86
			relative heat transfer coefficient, h: *(normalized to T_w = 0 K)*		1.304	1.304

New TFC:

			(calculated @ T_f)			
T_{ref} (K)	T_w (K)	T_f (K)	k (mW/m·K)	μ (μPa·s)	$h \sim k^{0.6}/\mu^{0.1}$	$h \sim k^{0.5}$
8000	0	4000	158.1	37.5	14.52	12.57
8000	8000	8000	247.3	58.7	18.16	15.73
			relative heat transfer coefficient, h: *(normalized to T_w = 0 K)*		1.251	1.251

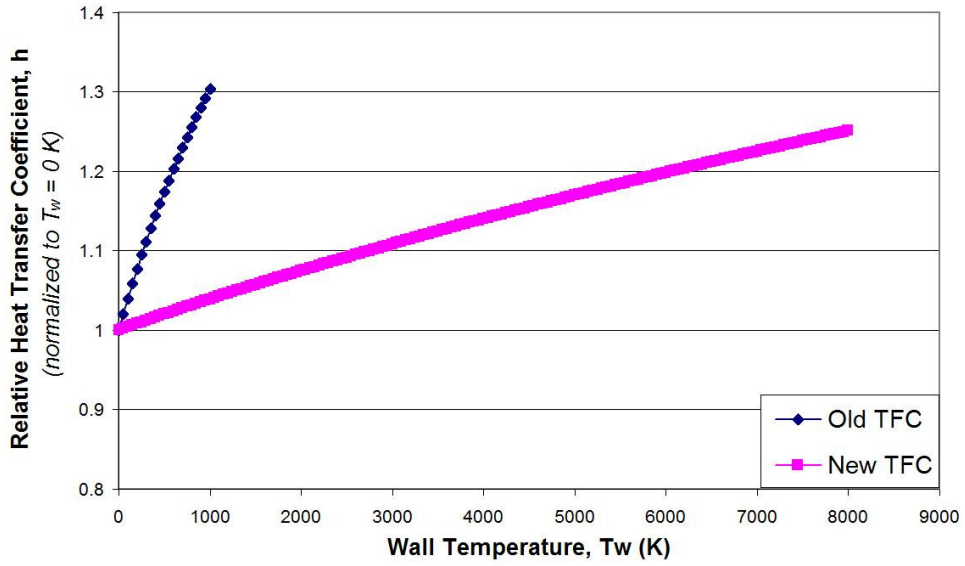

Figure 4.1: Heat Transfer Scaling vs. Wall Temperature

The second heating scenario is the effect in raising the chamber gas temperature from 1000 to 8000 K for the new target flight conditions. Once again holding the wall temperature at 0 K, the heat transfer coefficient was found to increase 107%. This calculation is illustrated for the temperature extremes in Table 4.3 and the entire temperature range in Figure 4.2.

Table 4.3: Heat Transfer Scaling vs. Chamber Gas Temperature

		(calculated @ T_f)				
T_{ref} (K)	T_w (K)	T_f (K)	k (mW/m·K)	μ (μPa·s)	$h \sim k^{0.6}/\mu^{0.1}$	$h \sim k^{0.5}$
1000	0	500	8.8	37.0	2.57	2.96
8000	0	4000	37.5	158.1	5.31	6.13
			relative heat transfer coefficient, h:		2.067	2.067
			(normalized to T_w = 0 K)			

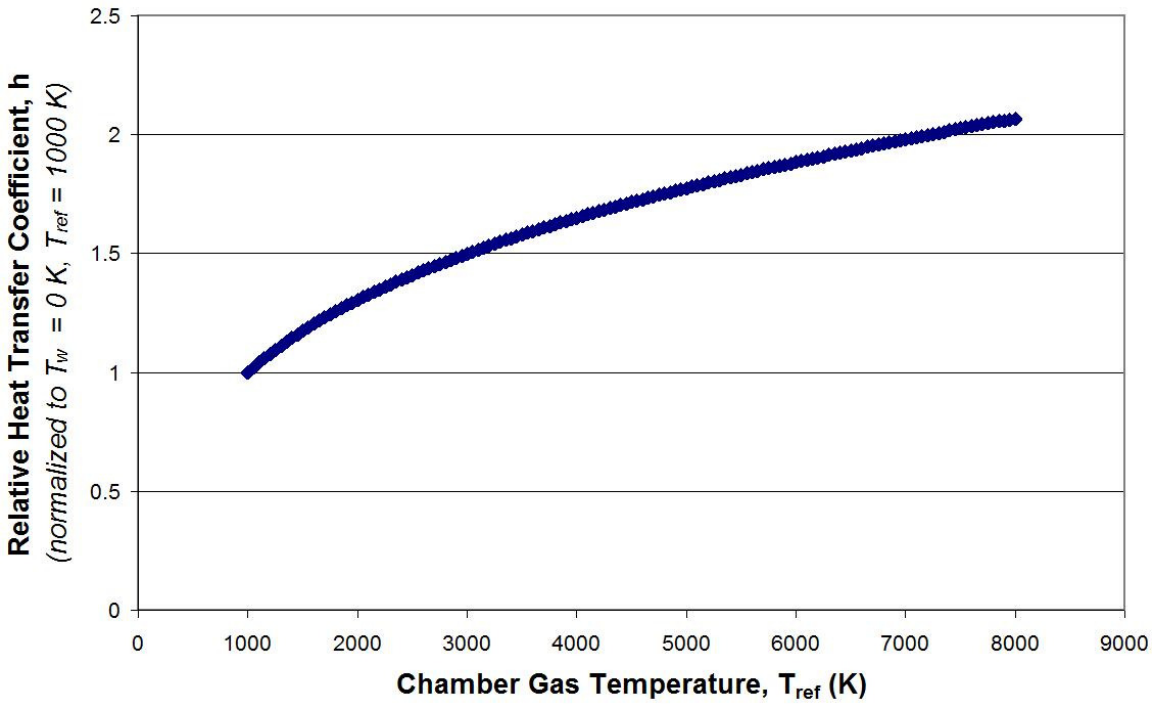

Figure 4.2: Heat Transfer Scaling vs. Chamber Gas Temperature

4.2: Convective Heating of LIFE Targets

The resulting flow fields and convective heat transfer to the surface of the LIFE targets traveling through the xenon environment of the LIFE chamber are presented here. The NIF-like hohlraum and exemplary spherical body have been exposed to the old target flight conditions, while the LIFE.2 target was simulated in the new flight conditions.

This work focuses on illustrating the similarities and differences in the thermal and viscous boundary layers through side-by-side comparison of the ANSY and DS2V flow field solutions of temperature, velocity and pressure for the LIFE targets. The before mentioned properties in addition to density will also be plotted along the stagnation line leading up to the stagnation point to help aid in this comparison, as well as provide insight into the heating of the hohlraum's surface. The resulting position-dependent heat fluxes will then be plotted along side the empirically and analytically heat transfer expressions derived previously in section 4.1.

The effects of increasing wall temperature on the local heat transfer coefficient are then investigated through a series of simulations performed with ANSYS to corroborate the conclusions of section 4.1. Finally, a simple design study has been included showing the advantages of including baffles to protect the windward face from excessive heating.

4.2.1: Flow Field Profiles

To see how well DS2V and ANSYS model the LIFE hohlraums in the target chamber, a comprehensive side-by-side comparison of the temperature, velocity and pressure flow fields will first be shown. Starting with the NIF-like hohlraum exposed to

the old flight conditions, the flow field contours are depicted in Figures 4.3.a–c. Note, the rainbow color scheme for the figures have been set for the combined global minimum and maximum of the corresponding DS2V and ANSYS simulations, shown subsequently in Table 4.4.

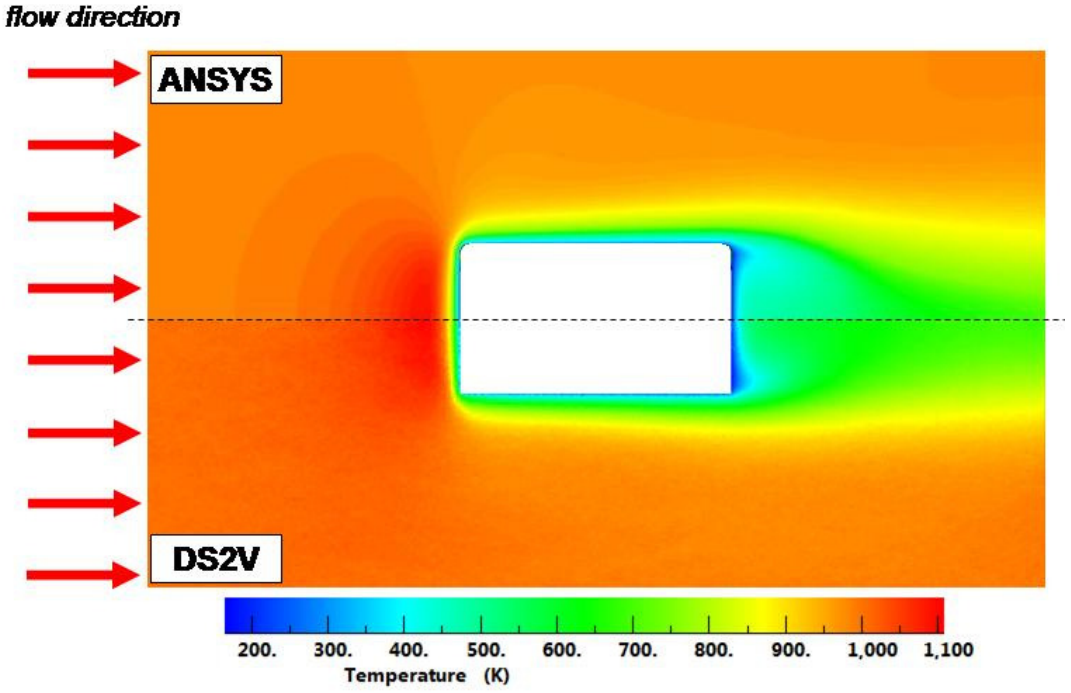

Figure 4.3.a: Old TFC, Temperature Flow Field; Normalized: 150-1108 K

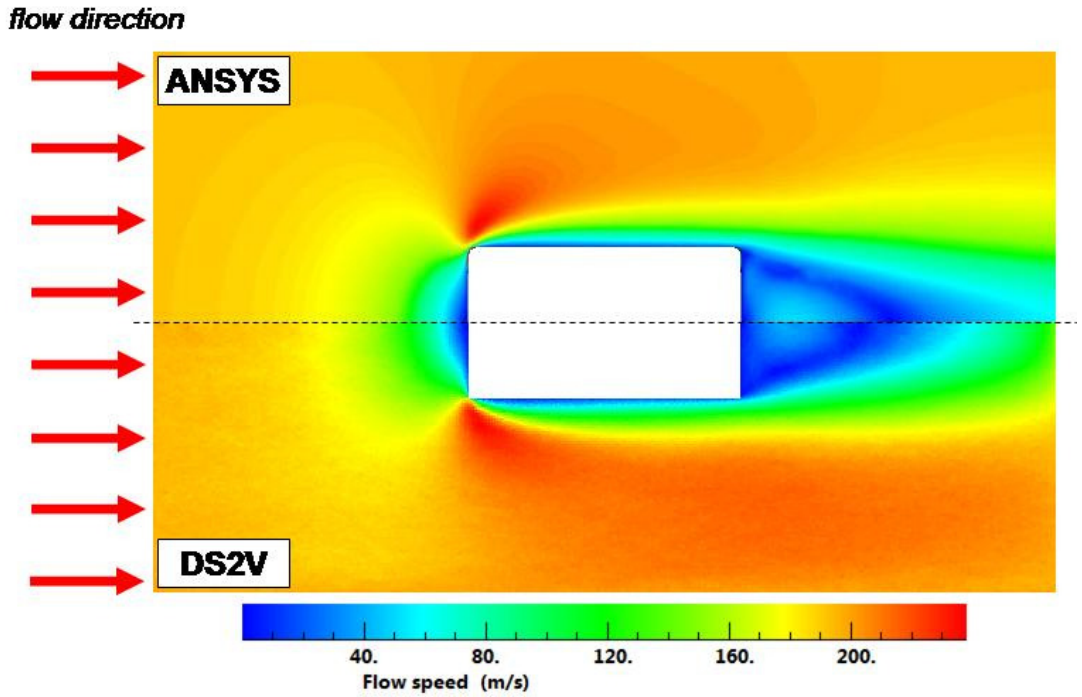

Figure 4.3.b: Old TFC, Velocity Flow Field;
Normalized: 0-238 m/s

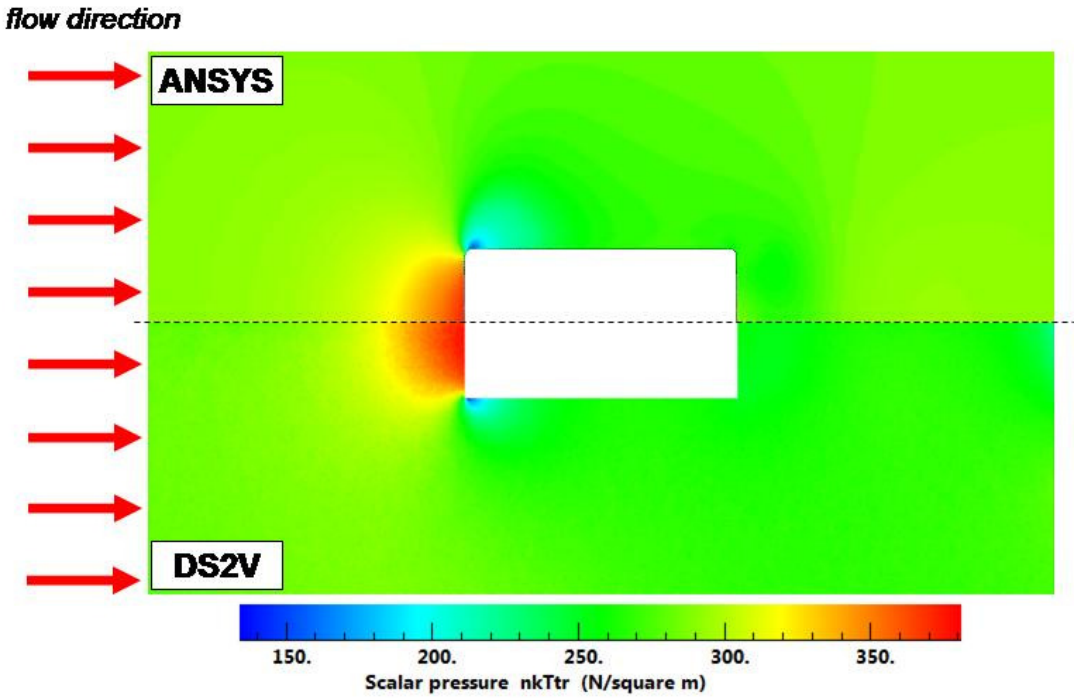

Figure 4.3.c: Old TFC; Pressure Flow Field;
Normalized: 134-381 Pa

The two distinctly different methods of ANSYS and DS2V show remarkable similarities in producing the flow field contours. The thermal boundary layers depicted in the temperature profile of Figure 4.3.a appear to be nearly identical in size, shape and magnitude. The viscous boundary layers illustrated in the velocity distribution of Figure 4.3.b is largely the same as well, with the only significant difference appearing in the size and shape of the wake following the hohlraum. Another disparity occurs within the pressure contours of Figure 4.3.c, where DS2V is predicting a slightly higher stagnation pressure than ANSYS. The magnitude of this difference will be looked at further in the subsequent section, when pressure is plotted along the stagnation line among other properties.

Similar flow field contours are depicted in Figures 4.4.a-c corresponding to the LIFE.2 target exposed to the new target flight conditions. However, since ANSYS was unable to find a solution when holding the wall temperature to 150 K, DS2V was re-run for a wall temperature of 2000 K. This was the lowest simulated wall temperature completed by ANSYS, and was done for continuity between the two simulations in comparing their flow fields and stagnation line properties in the subsequent section. Due to time constraints, only the front half of the hohlraum was simulated in DS2V for a reduced domain size 0.308 x 0.01 m in the 'X' and 'R' directions (see Figure 3.2). As before, the rainbow color scheme for the figures has been set for the combined global minimum maximum of the DS2V and ANSYS simulations, with the exception of the pressure contours of Figure 4.4.c. The reduced domain size appears to have created pressure singularities near the hohlraum's surface, and was set to match the global minimum and maximum of the ANSYS solution.

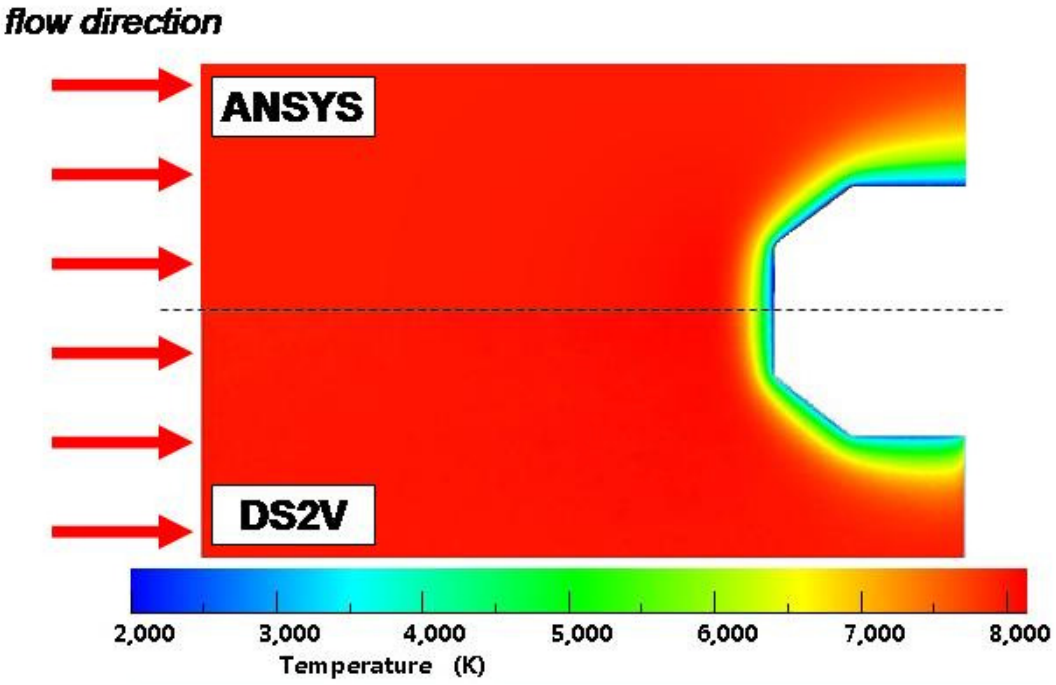

Figure 4.4.a: New TFC; Temperature Flow Field;
T_w = 2000 K, Normalized: 2000-8137 K

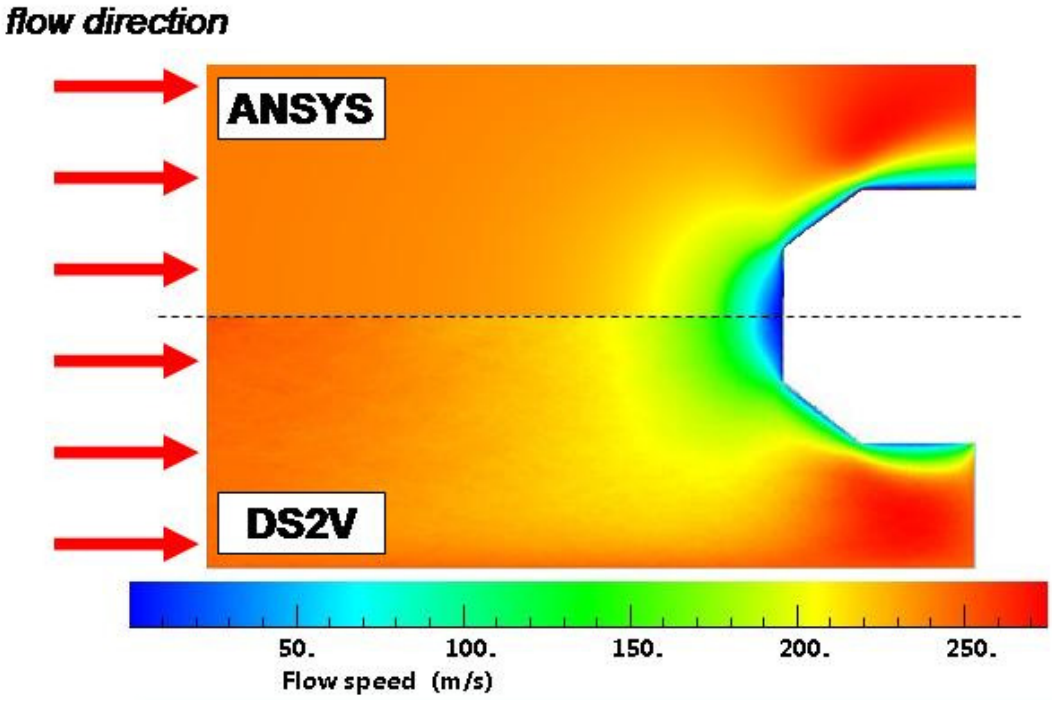

Figure 4.4.b: New TFC; Velocity Flow Field;
T_w = 2000 K, Normalized: 0-275 m/s

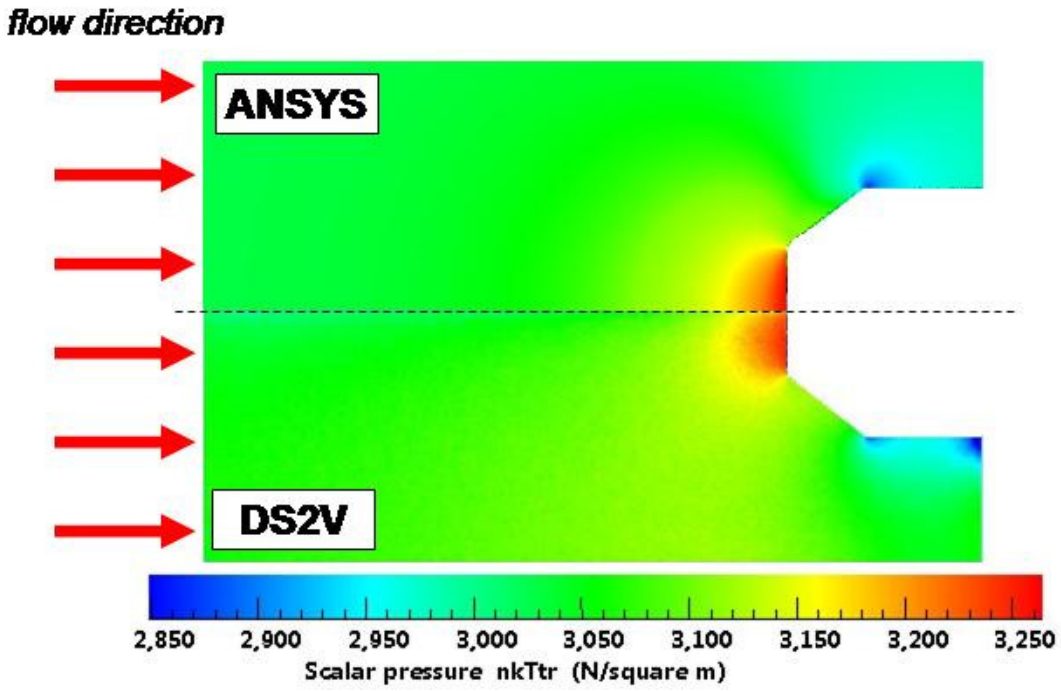

Figure 4.4.c: New TFC; Pressure Flow Field;
T_w = 2000 K, Normalized: 2049-3264 Pa

Despite DS2V being simulated on a reduced domain, the three contours of Figures 4.4.a-c are again remarkably similar. Distortions are seen on the far right boundary of DS2V, but they appear to not affect the upstream flow field excessively. The thermal boundary layer of Figure 4.4.a appears identical in size, shape and magnitude. Slight differences are seen in the velocity contours of Figure 4.4.b, especially in the deceleration of the gas along the stagnation line, but in general match very well. As with the NIF-like hohlraum, the largest discrepancy is seen in the pressure contours of Figure 4.4.c. The area in front of the leading surface in general appears alike in magnitude and size but there seems to be an unphysical drop in pressure along the axis of symmetry near the hohlraum's surface. This will be looked at closely in the following section.

In addition to providing the bounds for consistent color schemes of the previous figures, Table 4.4 allows for a comprehensive look at the global flow field properties predicted by DS2V and ANSYS. In general, good agreement in seen in the minimum and maximum property values, as was expected from the very symmetrical DS2V and ANSYS contours of Figures 4.3.a-c and 4.4.a-c. The one exception is the minimum pressure simulated by DS2V, but as shown in Figure 4.4.c is largely not an issue and a result of singularities near the surface due to the reduced domain size.

It is interesting to note the increase in velocity around the front edge of the hohlraum creates localized regions of increased Mach number approximately equal to 0.80 and 0.31 for the old and new TFC respectively. When compared to the overall Mach numbers of 0.62 and 0.27 presented earlier in Table 3.1, a potential cause of concern is raised. If the localized Mach number is able to break the local speed of sound, flight instabilities will likely occur that could jeopardize reliable target tracking and engagement. However, this is only likely to be a concern for the lower chamber temperatures, where the speed of sound is much more comparable with target velocity.

Table 4.4: Global Flow Field Property Comparison

	Old TFC				New TFC			
Global	DS2V		ANSYS		DS2V		ANSYS	
Flow Field Property	min	max	min	max	min	max	min	max
Temperature (K)	165	1108	150	1099	2272	8136	2000	8101
Velocity (m/s)	0	238	0	238	2	275	0	273
Pressure (Pa)	139	381	134	374	628	3255	2849	3264
Mach number	0	0.792	0	0.800	0	0.306	0	0.307

4.2.2: Flow Properties along Stagnation Line

The flow field contours of Figures 4.3.a-c and 4.4.a-c are useful in noticing asymmetries and large magnitude variation between the DS2V and ANSYS solutions. To better visualize these variations through the thermal and viscous boundary layers, the flow properties of temperature, velocity, pressure and density will be plotted along the axis of symmetry leading up to the stagnation point. The NIF-like hohlraum exposed to the old TFC will be shown first in Figures 4.5.a-d, followed immediately by Figures 4.6.a-d for the LIFE.2 target exposed to the new flight conditions. As before, Figures 4.6.a-d corresponds to ANSYS and DS2V solutions for a wall temperature of 2000 K. Note, the differences in plotted length are attributed to the different domain sizes of the ANSYS and DS2V simulations.

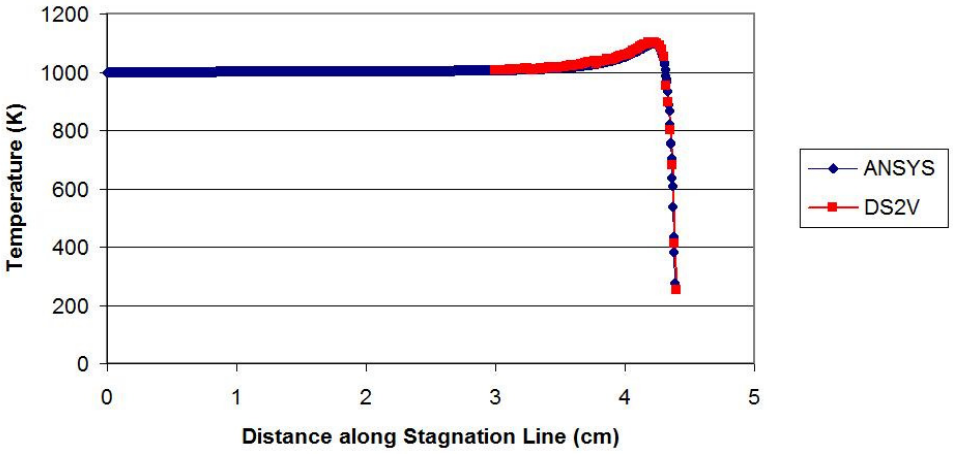

Figure 4.5.a: Old TFC, Temperature along Stagnation Line

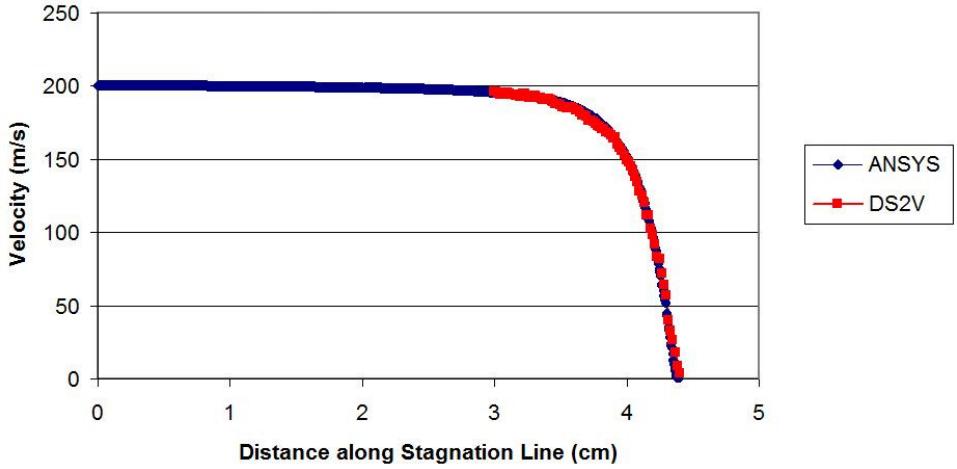

Figure 4.5.b: Old TFC, Velocity along Stagnation Line

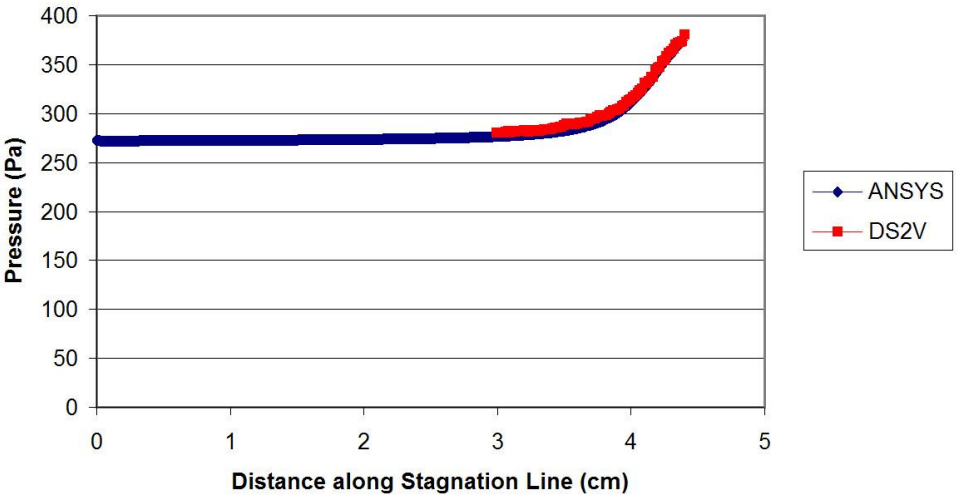

Figure 4.5.c: Old TFC, Pressure along Stagnation Line

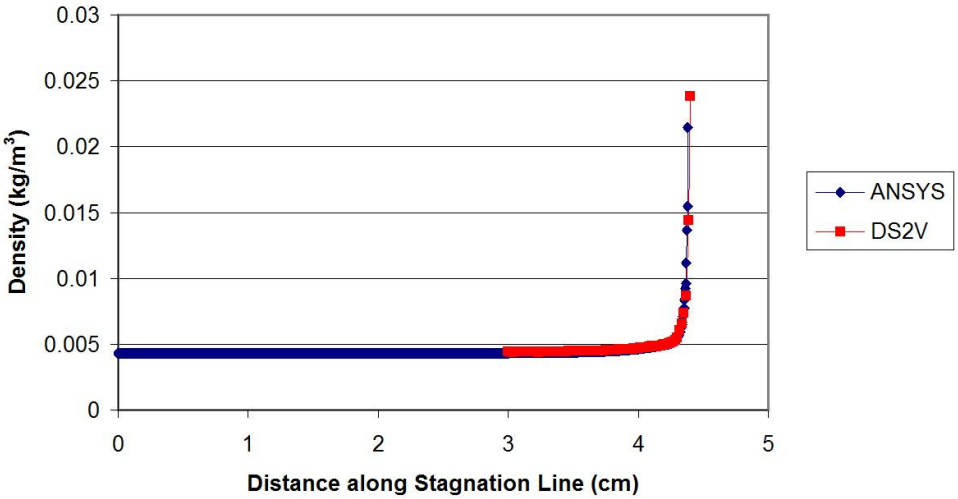

Figure 4.5.d: Old TFC, Density along Stagnation Line

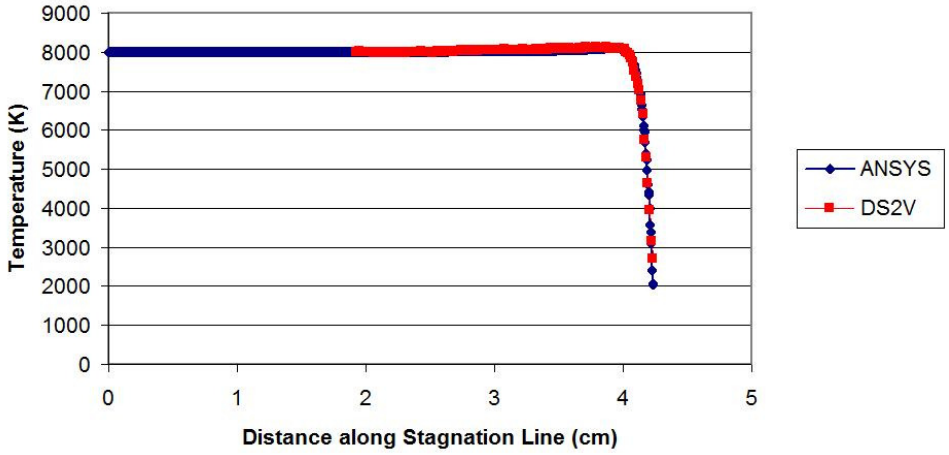

Figure 4.6.a: New TFC, Temperature along Stagnation Line

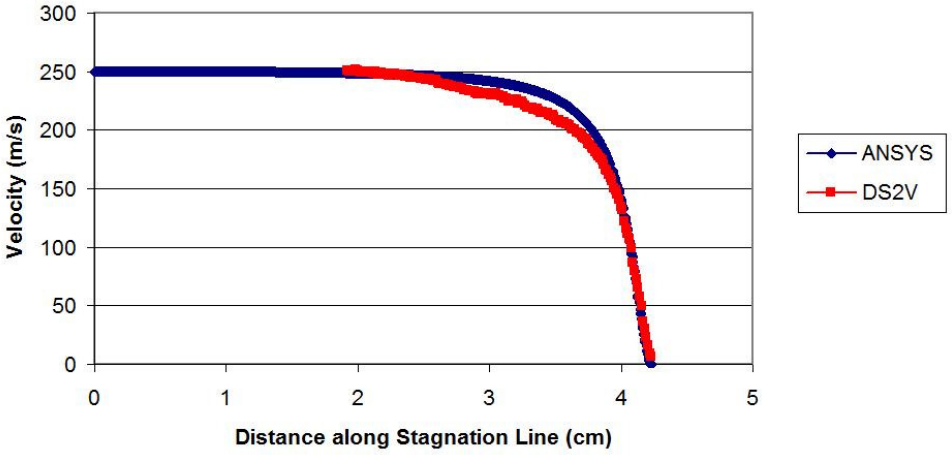

Figure 4.6.b: New TFC, Density along Stagnation Line

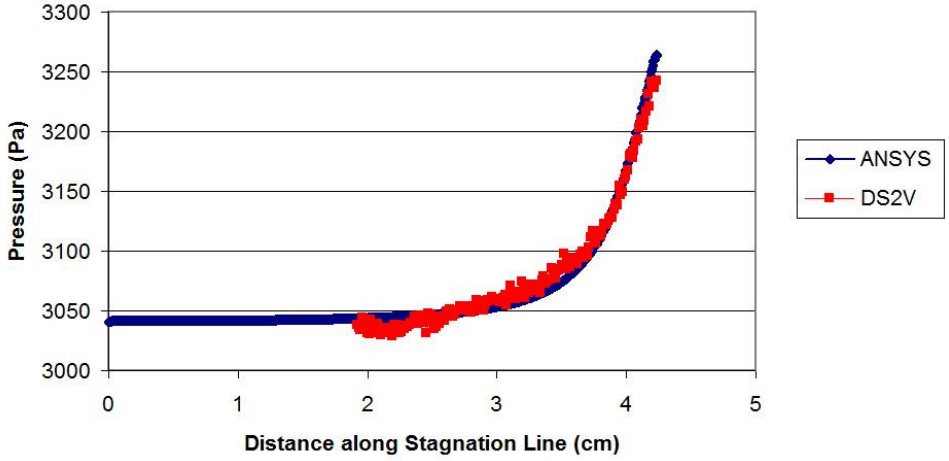

Figure 4.6.c: New TFC, Pressure along Stagnation Line

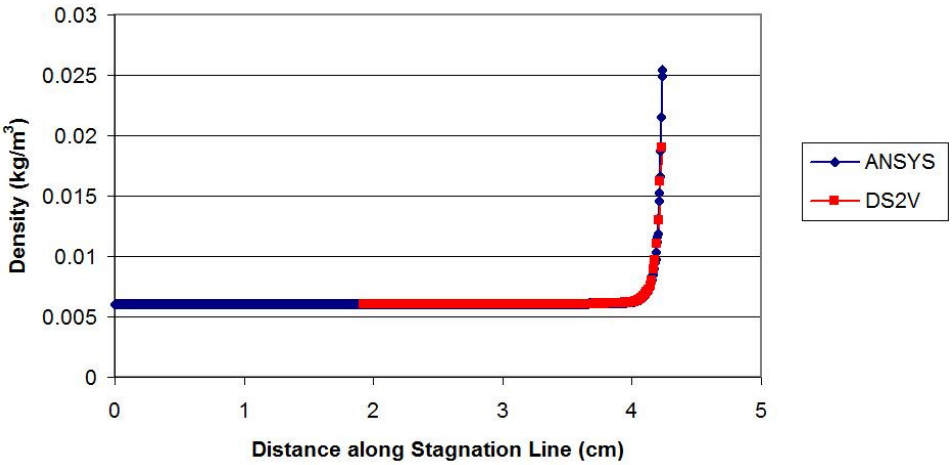

Figure 4.6.d: New TFC, Density along Stagnation Line

As was the case for the flow field contour plots of section 4.3, excellent agreement is seen between the DS2V and ANSYS methods in modeling the two flow conditions. All four stagnation line comparisons of Figures 4.5.a-d for the NIF-like hohlraum are virtually identical leaving little doubt that either DS2V or ANSYS modeled the flow with great accuracy. However, there is a bit more variation in the LIFE.2 plots of Figures 4.6.a-d. The temperature and density profiles for DS2V and ANSYS compare well with each other, but there appears to be some statistical scatter in the DS2V solution for speed and pressure. This is believed to be the direct result of the lack of refinement from limited time in running DS2V at the elevated temperature, and not of concern for final heat transfer results of the subsequent section where excellent refinement was shown.

Due to the significant increase in temperature and pressure near the stagnation point, a useful means of comparison is in calculation of the isentropic or 'total' flow properties. From Anderson, the isentropic pressure, p_t, and temperature, T_t, have been derived in terms of the overall Mach, and is shown in equations 4.3 and 4.4.[1]

$$\frac{p}{p_t} = \left(1 + \frac{\gamma - 1}{2} Ma^2\right)^{\frac{-\gamma}{\gamma - 1}} \tag{4.3}$$

$$\frac{T_t}{T} = 1 + \frac{\gamma - 1}{2} Ma^2 \tag{4.4}$$

These values are calculated and are shown next to the maximum temperature and pressure simulated by ANSYS and DS2V for the old and new flight conditions along the stagnation line within Table 4.5. In either case, the isentropic values should be considered as the theoretical maximums.

Table 4.5: Isentropic Flow Comparison along Stagnation Line

	Old TFC			New TFC (T_w = 2000 K)		
Flowfield Property	Isentropic	DS2V	ANSYS	Isentropic	DS2V	ANSYS
Temperature (K)	1126	1102	1099	8197	8121	8100
Pressure (Pa)	372	380	374	3228	3242	3231

From Table 4.5, it is can be seen that both DS2V and ANSYS model a stagnation temperature very near to each other, but not breeching the isentropic temperature. Conversely, the stagnation pressure predicted by DS2V and ANSYS is mildly higher then the isentropic condition for both flight conditions. This clearly is not physical, and points to slight inadequacies in the accuracy of both DS2V and ANSYS.

The density plots of Figure 4.5.d and 4.6.d are indicative of the large macroscopic gradients that lead to error within the Chapman-Enskog theory presented in section 3.2. In response, the local Knudsen number has been calculated based on the local density and

mean free path outputted by DS2V for the Old TFC along the stagnation line, and is shown in Figure 4.7.

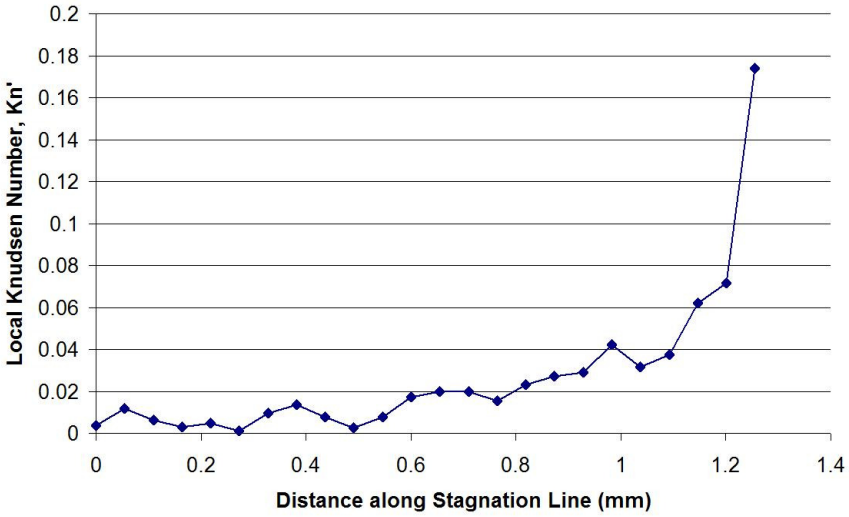

Figure 4.7: Old TFC, Local Knudsen Number along Stagnation Line

According to Bird, errors in the Navier-Stokes results are significant in regions of the flow where the local Knudsen number exceeds 0.1, and must be replaced by a molecular model above 0.2.[2] It is apparent from Figure 4.7 that this breakdown is occurring, but only in a very small region – approximately 50 microns - surrounding the target. For the greater part of the domain, it appears the continuum assumption is valid. However, since heat transfer along the surface of the hohlraum is of particular interest, the heating results from ANSYS come into question.

It is also interesting to note with regards to the old TFC, a 2% change in the upstream temperature and speed is seen at a distance of approximately 21.7 and 20.2 mm respectively in front of the target. This confirms the thermal and viscous boundary layers are comparable in length as was suggested previously in section 3.1.

4.2.3: Local Heat Flux along Hohlraum Bodies

A comprehensive look of the calculated and simulated heat fluxes along the LIFE targets are presented here. Taking the appropriate heat transfer coefficients from Table 4.1 and multiplying them by the temperature difference between the free stream and wall, they are plotted along side the simulated heat fluxes from DS2V and ANSYS in Figures 4.8-10. The first figure represents a fictitious spherical target traveling through the old TFC. The following two are for the NIF-like and LIFE.2 targets exposed to the old and new TFC respectively. For all three figures, the heat flux is plotted beginning with the windward center and ends at the leeward center.

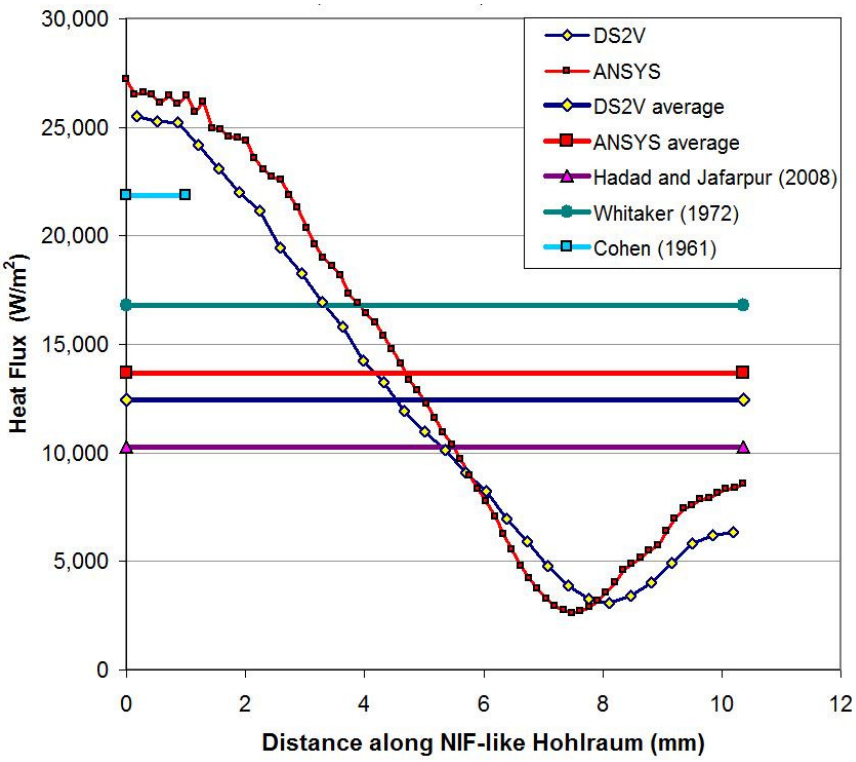

Figure 4.8: Old TFC, Heat Flux along Spherical Target; T_{ref} = 1000 K , T_w = 150 K

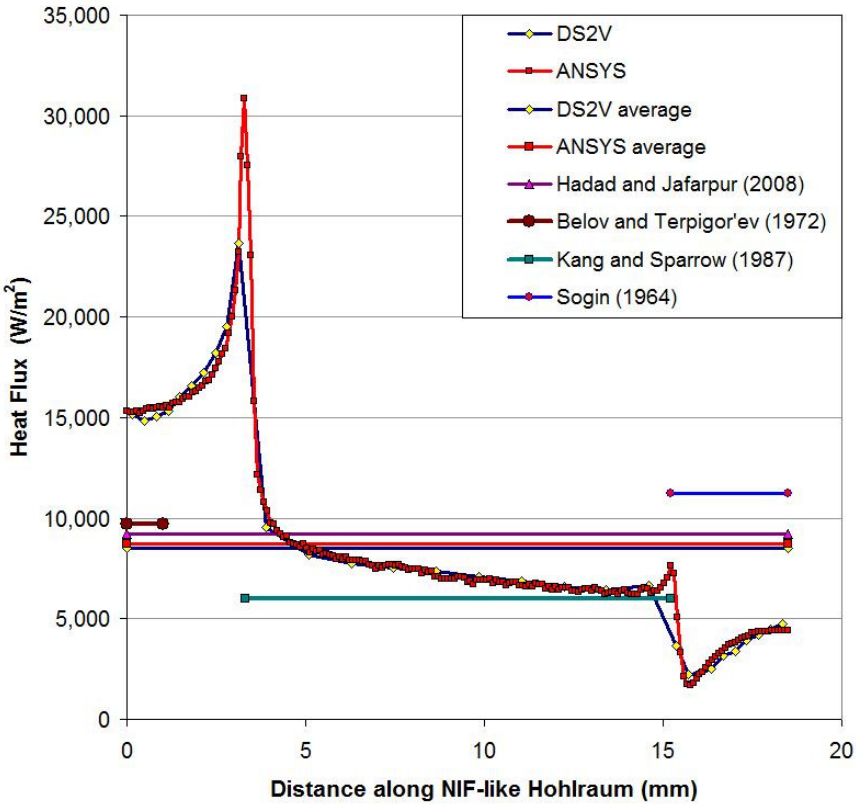

Figure 4.9: Old TFC, Heat Flux along NIF-like Hohlraum; T_{ref} = 1000 K , T_w = 150 K

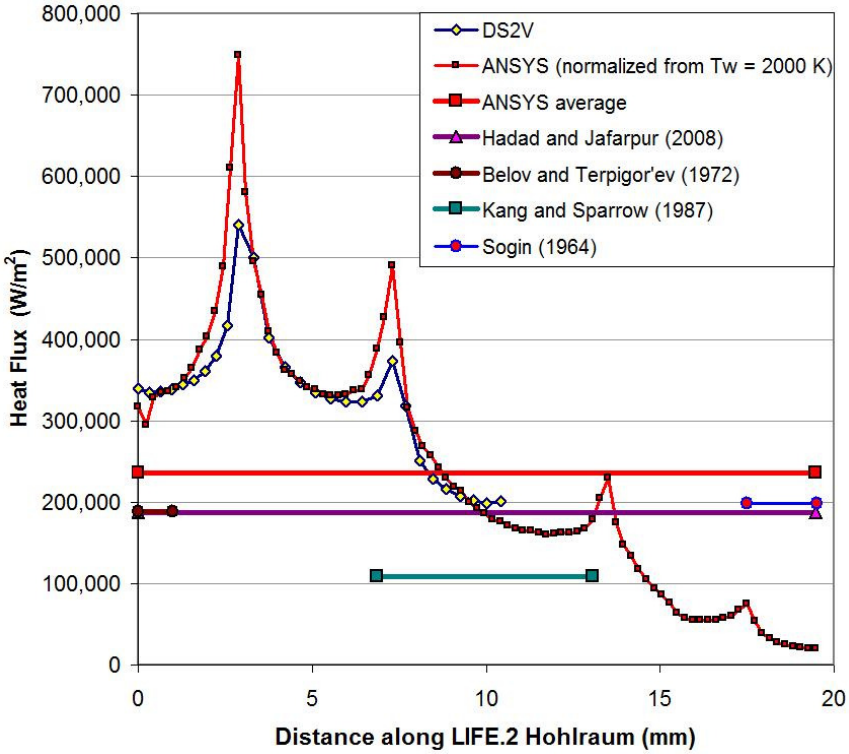

Figure 4.10: New TFC, Heat Flux along LIFE.2 Hohlraum; T_{ref} = 8000 K , T_w = 150 K

Correlations regarding spheres are numerous, and thus allowed the fictitious sphere of Figure 4.8 a sound basis of comparison between the DS2V and ANSYS programs. Their simulation in parallel with the LIFE targets allowed quick comparisons to be made with velocity flow field contours and surface pressure distributions, validating the proper implementation of the axisymmetric boundary conditions for each of the methods.

In regards to the results shown of Figure 4.8, DS2V and ANSYS solutions once again coincided with each other very well. ANSYS' heat flux, especially in the front half of the spherical target, was slightly higher than DS2V and 9% on average. As predicted, the correlation of Hadad and Jararpur proved to be slightly less than the average of DS2V and ANSYS, most likely caused by their assumption of incompressibility. No explanations can be said for why Whitaker is higher than expected other than it is being used slightly outside of its accepted bounds. As expected, the correlation provided by Cohen for heating near the stagnation point proved well above the average, but undershot the results by DS2V and ANSYS.

The results of the NIF-like target in the old TFC of Figure 4.9 are remarkably consistent. Not only is the heat flux predicted by ANSYS and DS2V match very well in position and average to one another with ANSYS being 3% higher on average, but is also very consistent to the average presented by Hadad and Jarapur. The maximum heat flux along the longitudinal surface predicted by Kang and Sparrow is substantially lower, but is to be expected from its use outside of its accepted applicability range. This is even more accentuated with the results of Sogin being significantly higher than predicted by DS2V and ANSYS along the trailing edge.

Many of the same results of the LIFE.2 target in the new TFC in Figure 4.10 can be made with its NIF-like predecessor of Figure 4.9. Note, only the front half of the LIFE.2 hohlraum was able to be simulated with DS2V due to time and computational constraints. In addition, the position-dependent heat flux of ANSYS was normalized to a wall temperature of 150 K to match its counterpart DS2V run. Validity of this assumption rests on the heat transfer coefficient remaining constant for increased wall temperature, and will be looked into further in the subsequent section. Nevertheless, the results obtained are very encouraging with DS2V and ANSYS once again matching very well with ANSYS 8% higher on average. However, the correlation of Hadad and Jarapur has become less applicable then before as its shape deviates further from a unit-length sphere. The results of Sogin as well as Kang and Sparrow are also only mildly applicable for the new flight conditions are still well outside the bounds of their accepted validity.

4.2.4: Local Heat Transfer Coefficient as a Function of Wall Temperature

A series of simulations were conducted using ANSYS to further investigate the effect of increasing wall temperature on the heat transfer coefficient, presented analytically from dimensionless variables in section 4.1. Beginning with the NIF-Like target in the old flight conditions, the heat flux along the hohlraum's surface was divided by the 850 K temperature difference between the 150 K wall and 1000 K upstream gas. This ANSYS simulation was then duplicated for increasing wall temperatures of 300, 600 and 900 K, with the resulting position-dependent heat fluxes being divided by the relative temperature differences of 700, 400 and 100 K respectively. The resulting local heat

transfer coefficients were then plotted as a function of position along the hohlraum's body in Figure 4.11.

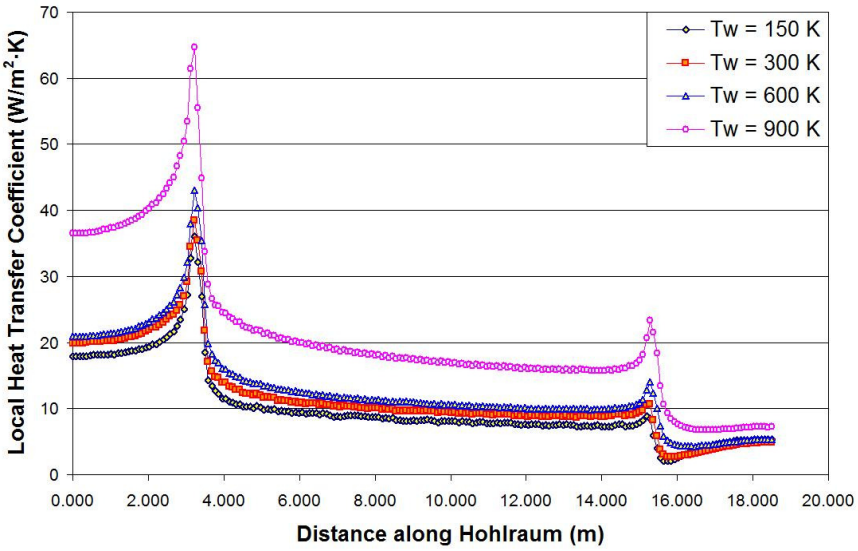

Figure 4.11: Old TFC, Local Heat Transfer Coefficient along NIF-like Hohlraum; T_{ref} = 1000 K

Figure 4.11 confirms the local heat transfer coefficient increases with wall temperature. Interestingly, the increase is steady for wall temperatures up to 600 K, but then shows a tremendous jump when reaching 900 K. This is in direct contrast to the smooth transition in Figure 4.1 for the analytically based derivation. For the wall increasing from 150 to 900 K, changes in the dimensionless variables predict an increase of 21% while ANSYS calculates an increase of 104% at the stagnation point. However, by restricting the wall temperature from 150 to 600 K, heating coefficient predictions of the two methods are much more consistent with one another; 14% increase from dimensionless variables and 17% increase from ANSYS.

As shown previously in section 4.3, the high speed of the target creates a stagnation region along the windward surface, raising the temperature to roughly 1100 K. The xenon gas then steadily decreases in value until coming to the fixed wall temperature

of the given simulation. It is therefore fair to assume a more appropriate reference temperature that corresponds to a 'total' temperature condition of 1100 K. Duplicating the procedure from before but with this new reference temperature, the new local heat transfer coefficients along the surface of the hohlraum were calculated and are presented in Figure 4.12.

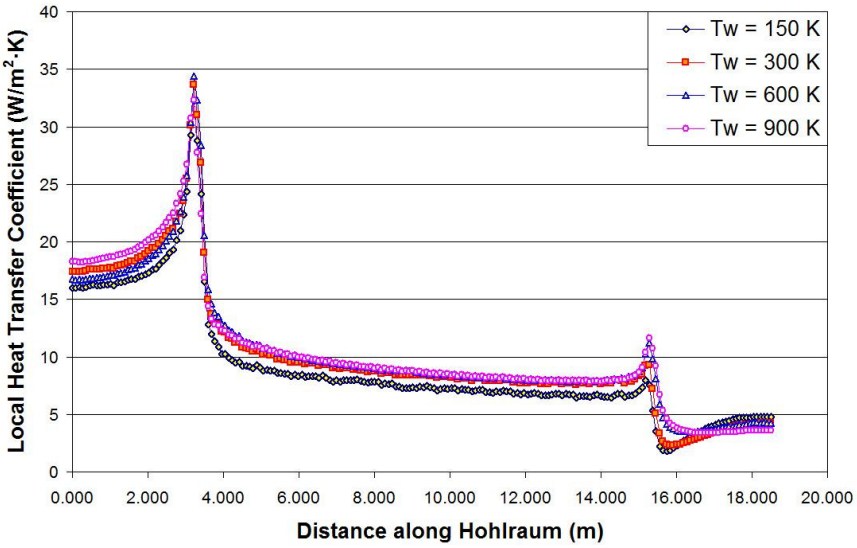

Figure 4.12: Old TFC, Local Heat Transfer Coefficient along NIF-like Hohlraum; T_{ref} = 1100 K

Choosing a new reference temperature of 1100 K did well to collapse the local heat transfer coefficient plots into a tighter distribution. However, unexpectedly the heating coefficient no longer steadily increases with wall temperature, but rather is the lowest for a wall temperature of 600 K. Nevertheless, for wall temperatures increasing from 150 to 900 K, ANSYS now predicts an increase of 17% to the dimensionless variables prediction of 21% at the stagnation point.

Similar calculations were performed with regards to the LIFE.2 target for the new flight conditions of varying wall temperatures 2000, 4000 and 6000 K to a reference

stream of 8000 K. The results of these calculations are shown in Figure 4.13. For the wall increasing from 2000 to 6000 K, ANSYS predicts an increase of 12% to the dimensionless variable's 6%. Although ANSYS was not able to simulate a wall at 150 K, the local heat transfer coefficient is not expected to change dramatically based on these results. Note, using the 'total' temperature of approximately 8200 K was not needed since the 200 K increase represents 2.5% of the free-stream temperature as opposed to 10% of the old TFC. In addition, simulating walls near the stream temperature of 8000 K where the choice in reference temperature becomes a problem is of no interest since the target would have long been destroyed.

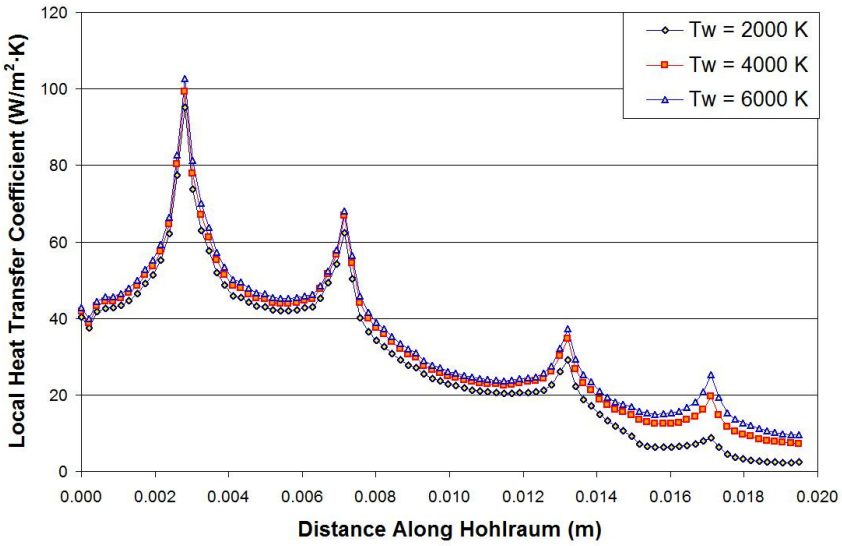

Figure 4.13: New TFC, Local Heat Transfer Coefficient along LIFE.2 Hohlraum; T_{ref} = 8000 K

4.2.5: Hohlraum Shaping

With the LEH window being orders of magnitude thinner than the hohlraum shell, the convective heating from the ambient high-temperature xenon gas to the window is the most importance. Not only does the window provide the easiest means for heat transfer to the fuel capsule, but failure of the window constitutes failure of the target. Therefore, designing the shape of the target to resist this heating is very important.

To illustrate one such design improvement, a baffle one radius in length on the windward end of the NIF-like hohlraum was simulated for the old flight conditions using DS2V. A side-by-side velocity profile of the hohlraum with and without this baffle can be seen in Figure 4.14.

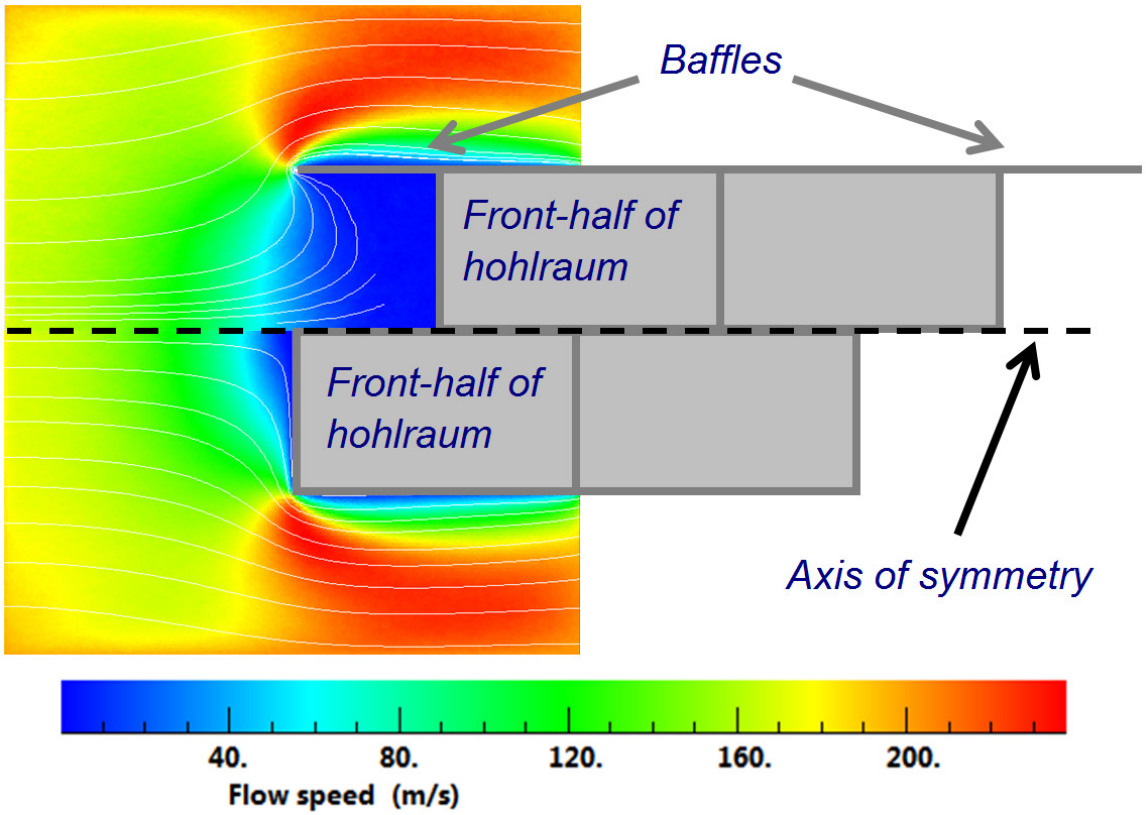

Figure 4.14: DS2V Velocity Profile of NIF-Like Hohlraum with and Without Baffles

While the baffle is borderline excessive in length due to the blocking of incident driver beams, this heat flux to the LEH window was decreased by a factor of 8.5!

This pitot-static tube inspired design illustrates a number of key advantages. First, the baffle traps xenon gas near the LEH window, providing a layer in which heat from upstream must conduct through to reach the window. This effectively reduces the convective heating mechanism of the window to conduction. In addition, since the target will be shot at cryogenic temperatures, the xenon gas trapped near the LEH window will be significantly colder than the ambient chamber gas. This gas must first come to temperature before being able to heat the window, and is expected to reduce the heat load to the LEH window even further.

4.2.6: Accuracy Discussion of DS2V and ANSYS Results

As described by Bird, the criteria for a good DSMC calculation with DS2V is for the mean collisional separation distance to mean free path (m.c.s./m.f.p.) to be much less than one, approximately 0.2.[2] However, meeting this criteria becomes troublesome with extreme temperature variation between the target and bulk flow. The full accommodation assumption dictates molecules hitting the wall to be ejected at the temperature of the wall, which is accompanied by significant reductions in the mean free path and dramatic increasing in the m.c.s./m.f.p. ratio.

To combat this, one of three variables can be changed: an increase in the number of simulated molecules or decrease in the domain size or temperature variation. For the old TFC, each of these were changed such that as molecules were added as

computationally possible by the DS2 program, only the front half of the target was modeled with an overall reduced domain by a factor of ten, and the wall temperature increased to 300 K. These three changes in unison yielded a maximum m.c.s./m.f.p of 0.23 throughout the domain. However, through the course of this refinement study, very little change in the overall flow field properties in addition to heat flux along the hohlraum's surface was seen. This leads to the conclusion that a small m.c.s./m.f.p. ratio signifies a DS2V simulation to be accurate, but not vice versa.

A similar refinement study in regards to the LIFE.2 target was also done, but was unsuccessful of making an adequate m.c.s./m.f.p ratio. The late introduction of the new TFC parameters, in addition to increases in number density and temperature made this a very difficult task. Molecular number and domain size was altered as before, but a significant temperature increase would have been needed to further reduce the ratio near 0.2. Nevertheless, a maximum m.c.s./m.f.p. of 1.6 was obtained for a wall temperature of 150 K, but as before there was very little change in flow field properties and surface heat flux and were not expected to change further for future refinements.

In contrast to the mutli-week DS2V simulations needed for the previous refinement studies, ANSYS was able to prove its accuracy relatively quickly. By halving the maximum element edge length on the hohlraum's surface and axis of symmetry, in addition to reducing the expansion factor from 20 to 5% (see Table 3.2), the number of elements increased from approximately 1 to 4 million grouped tightly around the hohlraum. This along with increases in domain had no final effect on either the flow field or heat flux to the targets surface. With the continuum assumption proven to be accurate for the vast majority of the ANSYS domain, and with close agreement between

ANSYS and DS2V for the simulated heat flux along the hohlraum walls, it appears the thin layer surrounding the hohlraum where the continuum assumption begins to break down did not have a substantial effect in its final heating results.

4.3: Transient Thermo-Mechanical Behavior of Target

The sensitivity of the heat transfer internal to the LIFE targets have been analyzed for varying external heat transfer coefficients imposed while the target transverses across the high-temperature chamber gas while spinning at 15,000 RPM. This work focuses on the heating of the LEH window as well as the helium internal to the target surrounding the fuel capsule to aid in the optimization of the final target design.

This work was performed in collaboration with the LIFE team at LLNL, and thus only heating of the LIFE targets for the most recent flight conditions were of interest. As described in Section 3.5, coupling of the heat transfer and fluid mechanics internal to the hohlraum was accomplished using the multi physics code COMSOL. Note, this analysis only takes into account the convective heating of the hohlraum once inside the chamber, ignoring radiation effects from the chamber walls.

4.3.1: Developing Helium Flow Field Internal to Target

Before modeling the hohlraum inside the target chamber, the transient flow field solution to the helium internal to the target must be understood. During injection, the target will have been accelerated from rest to a velocity of 250 m/s, spinning at a rate of 15,000 RPM. This spin is necessary for flight stabilization, but is also important in understanding its effects on the heating of the helium internal to the hohlraum.

To look at development of this internal flow field, the helium of the larger LIFE.2 target was assumed initially at rest, and then instantaneously exposed to no-slip interior walls being spun at 15,000 RPM along its axis of symmetry. Figures 4.15 and 4.16 depict the angular velocity of the internal helium after 20 ms and the angular velocity along the centerline of the hohlraum - with no capsule, starting along the axis of symmetry and going radially outward - in 1 ms intervals respectively. For clarification, Figure 4.16 contains a schematic of the LIFE.2 target highlighting the plotted path by a red arrow. After 20 ms, the flow reached a minimum of 96% of its steady-state value. Considering the target will spend approximately 44 ms while in free-flight (also referred to as 'drift') before reaching the target chamber, the helium internal to the target is expected to be fully developed angularly upon entering the chamber.

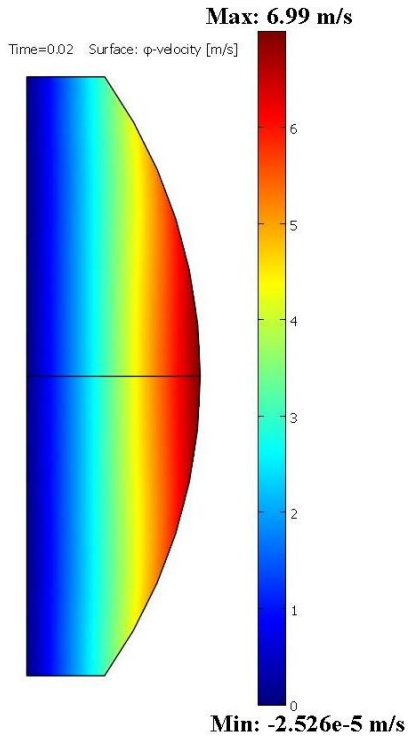

Figure 4.15: Angular Velocity (m/s) of the Helium Internal to the LIFE.2 Target after 20 ms; Helium Initially at Rest, Interior Walls Spin at 15,000 RPM

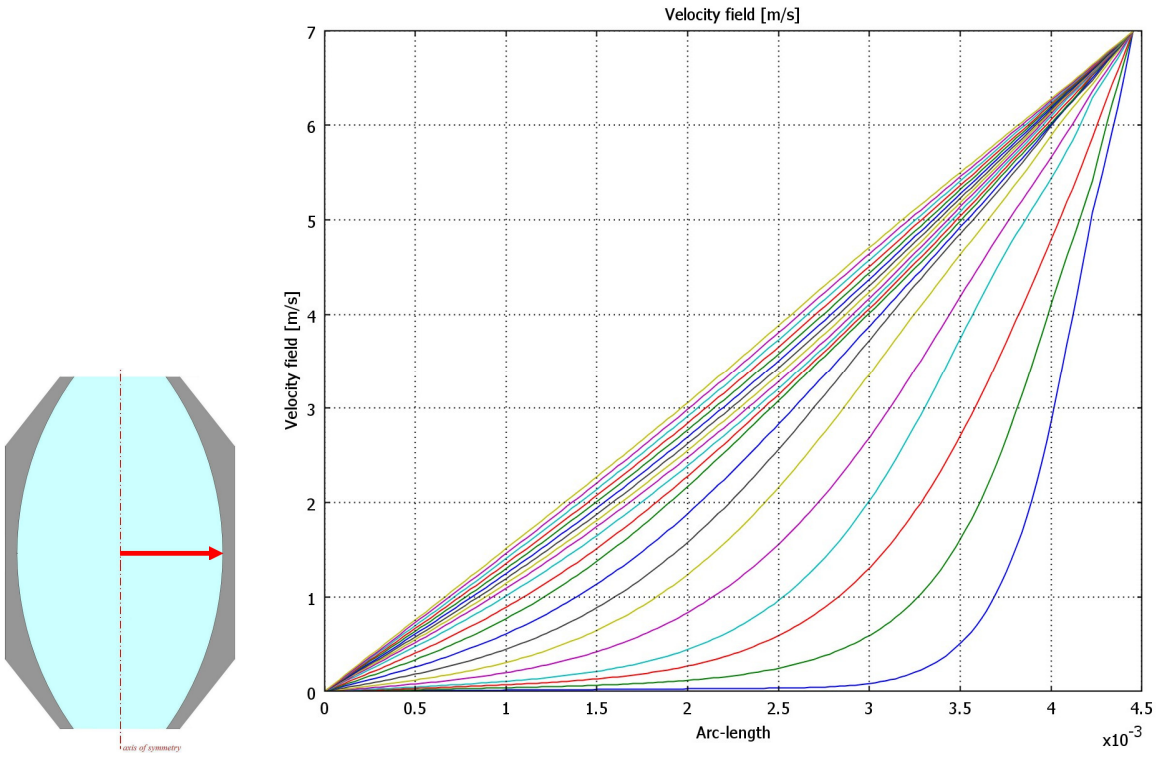

Figure 4.16: Angular Velocity Development of Helium Internal to the LIFE.2 Target vs. Radial Distance in 1 ms Intervals

4.3.2: Adiabatic/Insulated LEH Window Heating

Using the external heat transfer coefficients, a fully transient thermal response of the LEH window can be performed. Assuming a polyimide (old TFC), adiabatic window that does not transfer any heat to the interior of the hohlraum, analysis is first completed by use of the "lumped capacitance method," where by a body is immersed in a fluid assumed to be isothermal during heating/cooling. To check the validity of this assumption, it is first necessary to see if the thermal resistance at the body/fluid interface (LEH window/xenon gas) greatly exceeds the thermal resistance within the interior of the body (LEH window). Computationally, this generally equates to a Biot number (hL_c/k) of less than 0.1, where h is the external heat transfer coefficient, L is the characteristic

length and k the thermal conductivity of the solid.[3] Although the thermal conductivity of polyimide is low (approximately 0.048 W/m·K at 20 K[4]), the window thickness, L_c, is so thin that the Biot number remains small, around 2.1 x 10^{-4} for a heat transfer coefficient of 20 W/m^2·K. Thus the assumption of the window being isothermal during heating is valid, and the lumped capacitance method for the adiabatic heating of the window can be used with great accuracy.

In a lumped capacitance model, temperature in a solid equilibrates with the surrounding fluid in an exponential manner as shown by equation 4.5:

$$\frac{T - T_\infty}{T_i - T_\infty} = \exp\left[-\left(\frac{hA}{\rho V c_p} \right) t \right] \tag{4.5}$$

where T_∞ is the stream temperature, T_i is the initial temperature of the window, ρ is the polyimide density, c_p the polyimide heat capacity, V and A the volume and surface area of the body respectively, and h is the heat transfer coefficient from the body to the surrounding fluid assumed to be constant over the body's entire surface.[3] Figure 4.17 shows the heat capacity of polyimide changes significantly as it heats from its cryogenic starting point, necessitating a time-dependent solution.

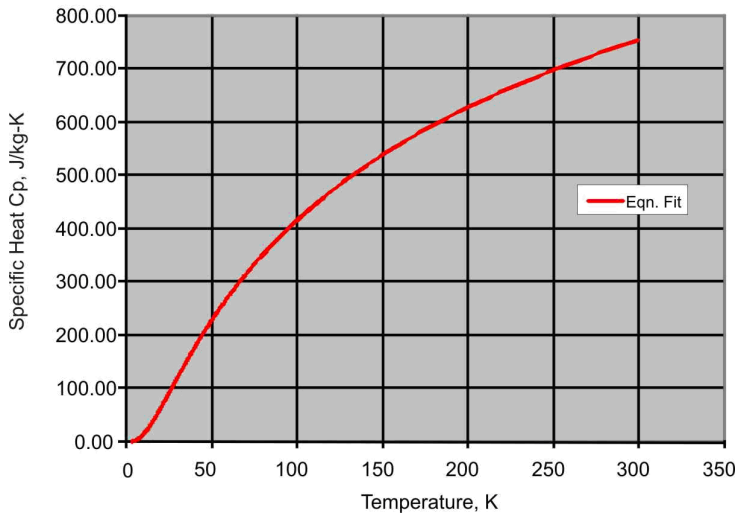

Figure 4.17: Polyimide Specific Heat (J/kg-K)[4]

According to DuPont, Kapton has been used successfully up to 400 ˚C. It does not melt, but rather decomposes at about 500 ˚C with failure between 675-775 K.[5] Temperature dependent solutions of the adiabatic window heating for chamber temperature 8000 K heat transfer coefficients 10, 20, 30 and 40 W/m^2·K are shown in Figure 4.18. It is apparent the LEH window by itself offers very little thermal resistance in heating for this adiabatic case. Note, this analysis was not repeated using graphene for it still in the development stages. In addition, it has no bearing on the heating analysis presented in the subsequent section where a 'virtual" LEH window is assumed with zero thermal inertia.

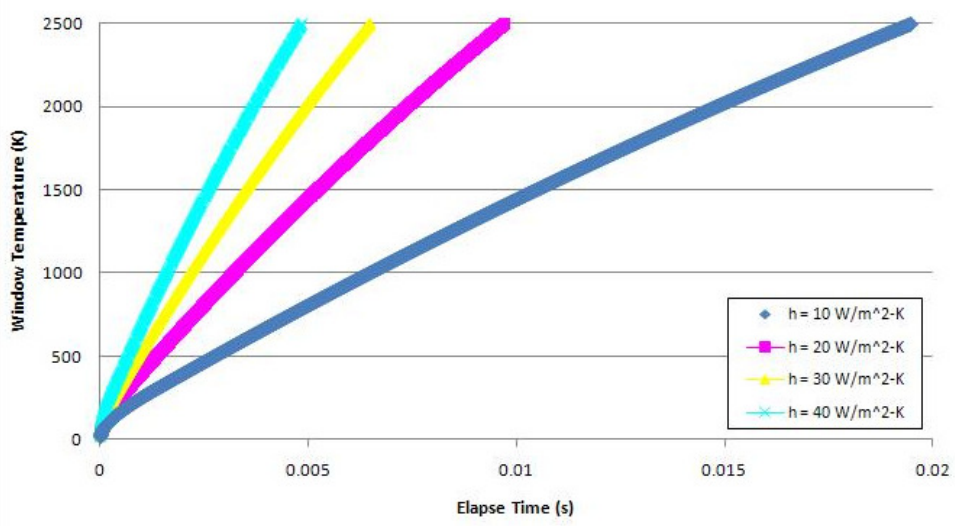

Figure 4.18: Adiabatic Heating of the Polyimide Window Using the 'Lumped Capacitance Method'

4.3.3: LEH Window Heating with Insulated Walls and Internal, Spinning Helium

The helium will now be incorporated to the hohlraum to understand its effects in acting as a heat sink for possible heating/cooling of the LEH window and fuel capsule as a function of the external heat transfer coefficient along the LEH window. As mentioned previously in section 3.5, the window thickness is approximately four orders of magnitude smaller than the hohlraum's diameter or length, and thus cannot be meshed along side the hohlraum's internal helium using COMSOL. Therefore, a "virtual" LEH window that offers no thermal resistance in heating of the internal helium will be assumed. To study the external convective heating of the helium through the LEH window independent of other heating mechanisms, the polystyrene walls and fuel capsule surfaces will be assumed to act as perfect insulators.

Figure 4.19 depicts the axial, radial and angular velocity of the LIFE.2 target after 24 ms while being spun and undergoing a heat flux set by a heat transfer coefficient, h =

5 W/m^2 and reference temperature, T_{inf} = 8,000 K through the LEH window. Analogous to buoyancy effects in free convection, the increase in temperature near the LEH window - and consequently the decrease in density - results in a flow "rising," moving radially inward opposite of the outward radial acceleration. The surrounding cooler helium then moves to replace it, setting up circulating convections cells internal to the target. A temperature profile with streamlines has been included in Figure 4.19 for clarity. For this simulation, the heat transfer through the upper and lower LEH windows are equal, resulting in mirrored circular flow of the upper and lower regions.

As the heat load through the LEH window increases, the helium internal to the hohlraum begins to take on a different shape altogether. The buoyancy effects seen in Figure 4.19 are quickly dominated by the helium expansion near the LEH windows, causing an outward movement of helium along the entire window's surface. This helium expansion is illustrated in Figure 4.20 for an elevated heat transfer coefficient of 20 W/m^2·K, including a temperature profile with streamlines for clarity.

Pressure increases and density gradients are expected to follow suit from this expansion of helium. As shown in Table 2.1, the helium internal to the target is initially at 17 K with a density of 1 mg/cc or 1 kg/m^3, corresponding to an initial pressure of 35,311 Pa. Continuing the example with an elevated heat transfer coefficient of 20 W/m^2·K, the pressure is shown to stay equilibrated through its domain and rise 61% to 56,810 Pa over the 24 ms simulation in Figure 4.21. This pressure increase is a function of the total heat added to the system, varying from an 19% increase to 42,000 Pa and a 119% increase to 77,240 Pa for heat transfer coefficients of 5 and 40 W/m^2·K respectively.

Density gradients were expected from the apparent buoyancy effects described earlier; however, the density profile as a function of time reveals density gradients due to thermal expansion dominate the solution for higher and lower heat fluxes alike. Figure 4.22 shows the density transient solution for a heat flux again set at a heat transfer coefficient, h = 20 $W/m^2 \cdot K$ for the spun LIFE.2 target in 4 ms intervals. The maximum density at the end of the 24 ms run scales with the maximum pressure; 18.9% and 118.7% increase for heat transfer coefficients 5 and 40 $W/m^2 \cdot K$ respectively. However, the overall minimum density change is far more drastic, but more consistent between runs, having a 95.7% to 98.3% reduction in density near the LEH windows for heat transfer coefficients 5 and 40 $W/m^2 \cdot K$ respectively.

Note, the simple hohlraum schematics of Figure 2.4 of Chapter 2 are incomplete for they do not show all of the features internal to the target. For instance, the internal structure of the fuel capsule is omitted, but more importantly to this analysis are the absent radiation shields between the fuel capsule and LEH windows. It is likely the presence of these shields will retard the helium thermal expansion and heating of the capsule while exasperating the heating of the LEH windows. Nevertheless, the rest of this analysis will assume those shields are not in place when looking at these two heating effects.

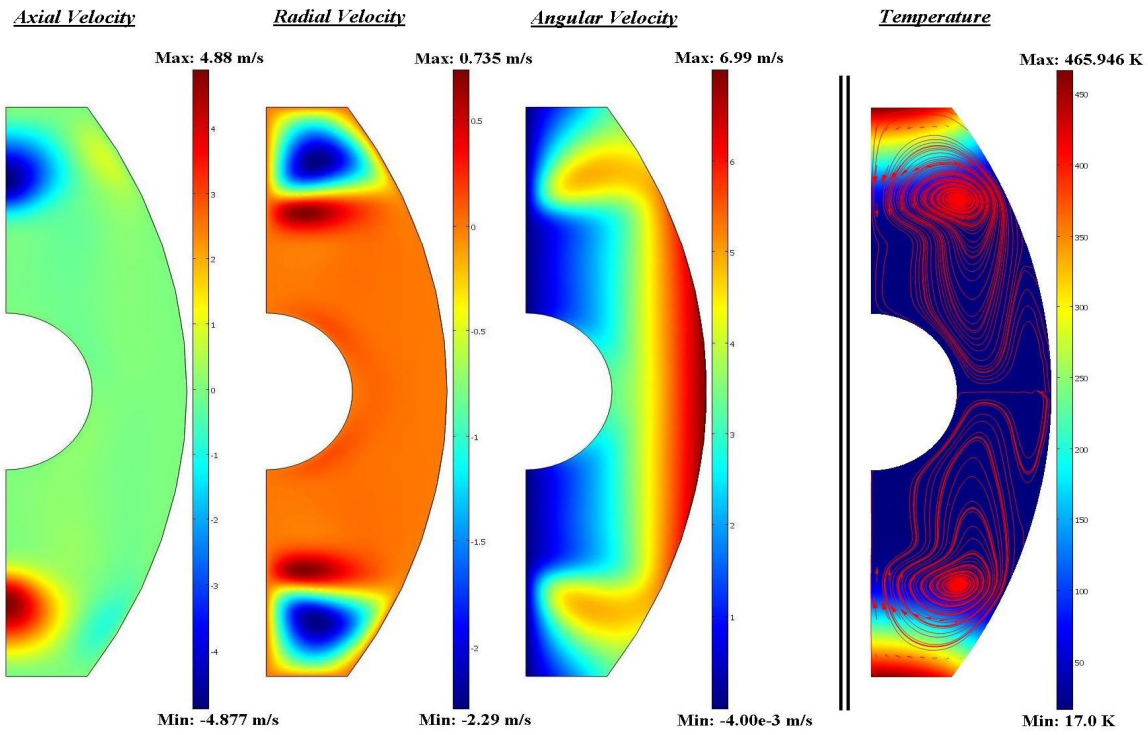

Figure 4.19: Velocity and Temperature Profiles of Spun LIFE.2 Target after 24 ms; h = 5 W/m^2·K, T_{inf} = 8000 K

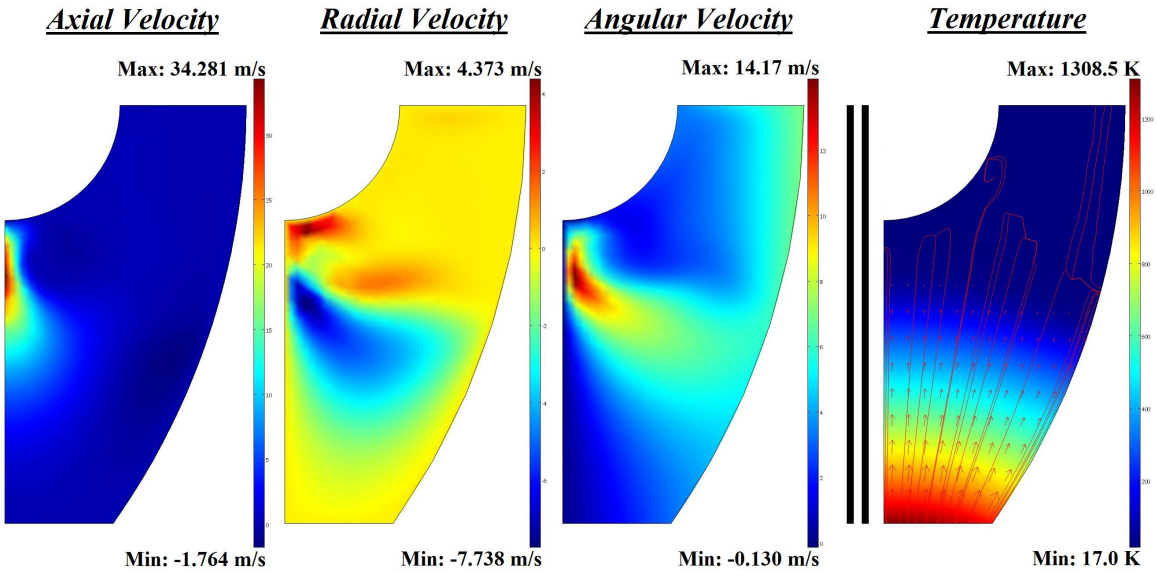

Figure 4.20: Velocity and Temperature Profiles of Spun LIFE.2 Target after 24 ms; h = 20 W/m^2·K, T_{inf} = 8000 K

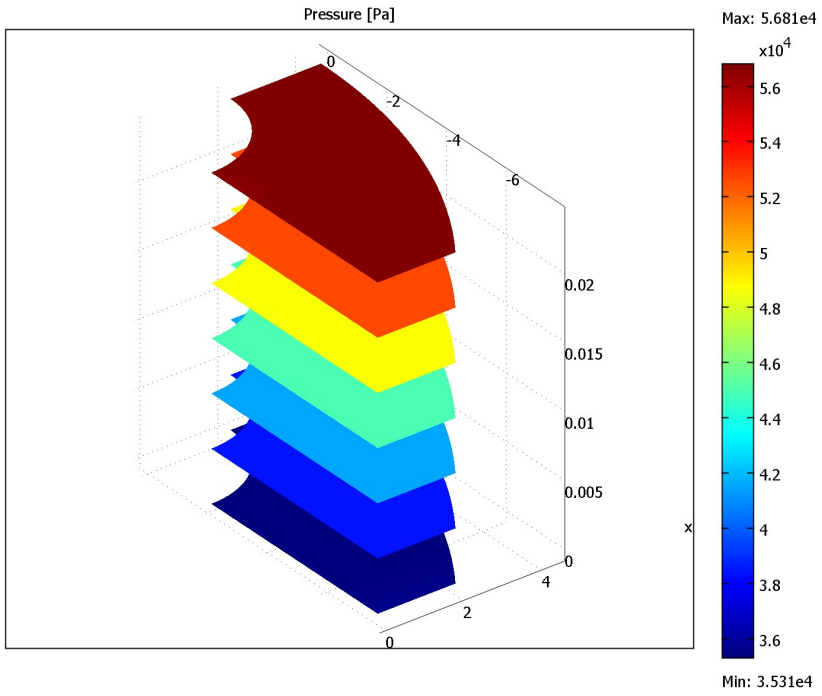

Figure 4.21: Transient Pressure Profile of Spun LIFE.2 Target in 4 ms Intervals; h = 20 W/m^2·K, T_{inf} = 8000 K

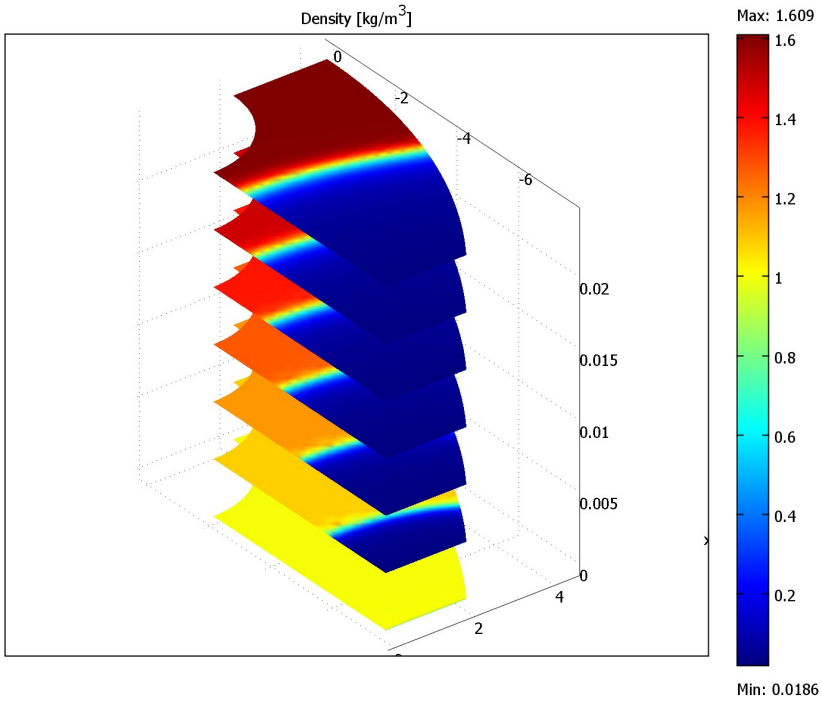

Figure 4.22: Transient Density Profile of Spun LIFE.2 Target in 4 ms Intervals; h = 20 W/m^2·K, T_{inf} = 8000 K

The sensitivity of the maximum helium temperature for both the NIF-like and LIFE.2 hohlraum as a function of the external heat transfer coefficient is plotted in Figure 4.23. For each simulation, the maximum temperature was obtained along the axis of symmetry and is thus thought of as the maximum LEH window temperature. Variation of the window temperature between targets is attributed to geometry differences. Assuming the hohlraum's walls act as good insulators, the decrease in window diameter does well to decrease the total amount of heat introduced to the interior of the target. It is interesting to note that regardless of size, the heat-up of the window temperature appears nearly linear upon reaching a certain heat transfer coefficient threshold, in these cases around 10 $W/m^2 \cdot K$. This transition appears to be when the buoyancy effects are dominated by the expansion of helium near the LEH window for the higher driven heat fluxes.

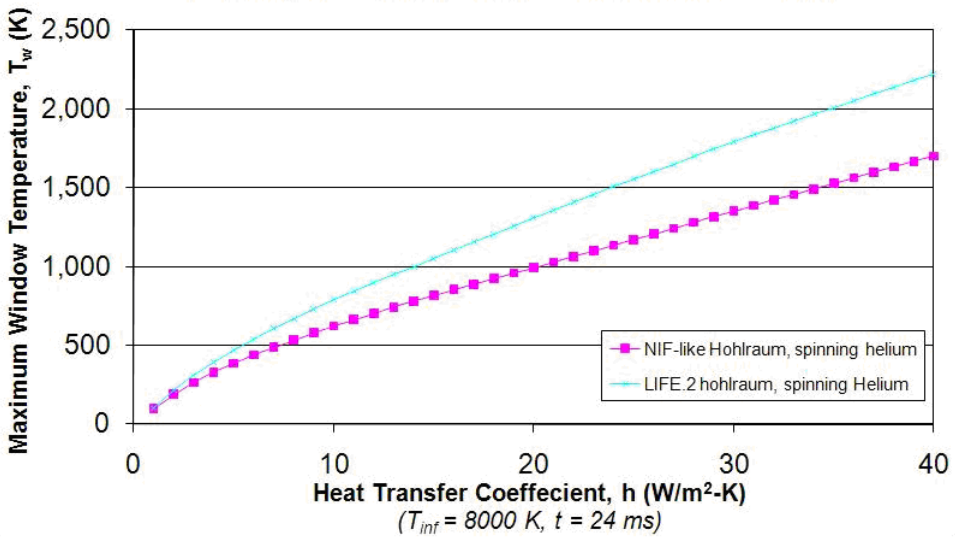

Figure 4.23: Maximum Window Temperature for the NIF-like and LIFE.2 Hohlraums as a Function of the External Heat Transfer Coefficient

While these simulations are not set up to directly show the heating of the DT ice layer, the helium temperature leading to and around the capsule's surface as a function of time can be shown. These are represented in Figures 4.24 and 4.25 for the LIFE.2 target respectively, for a heat transfer coefficient, h = 20 $W/m^2 \cdot K$ and reference temperature, T_{inf} = 8,000 K. For clarification, each figure contains a schematic of the LIFE.2 target highlighting the plotted path by a red arrow. The portion of the capsule laying on the axis of symmetry shows the greatest temperature increase, and is plotted as a function of heat transfer coefficient next to the NIF-like target for comparison in Figure 4.26.

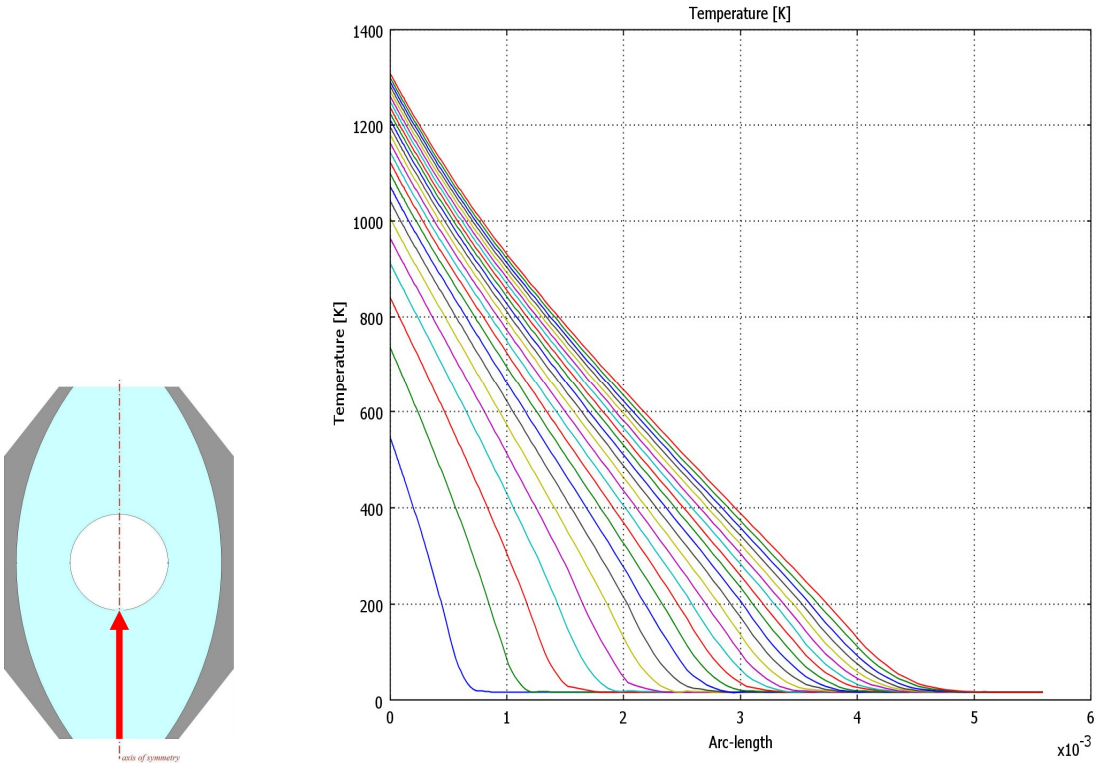

Figure 4.24: Helium Temperature Profile from LEH Window to the Fuel Capsule's Surface along the Axis of Symmetry in 1 ms Intervals

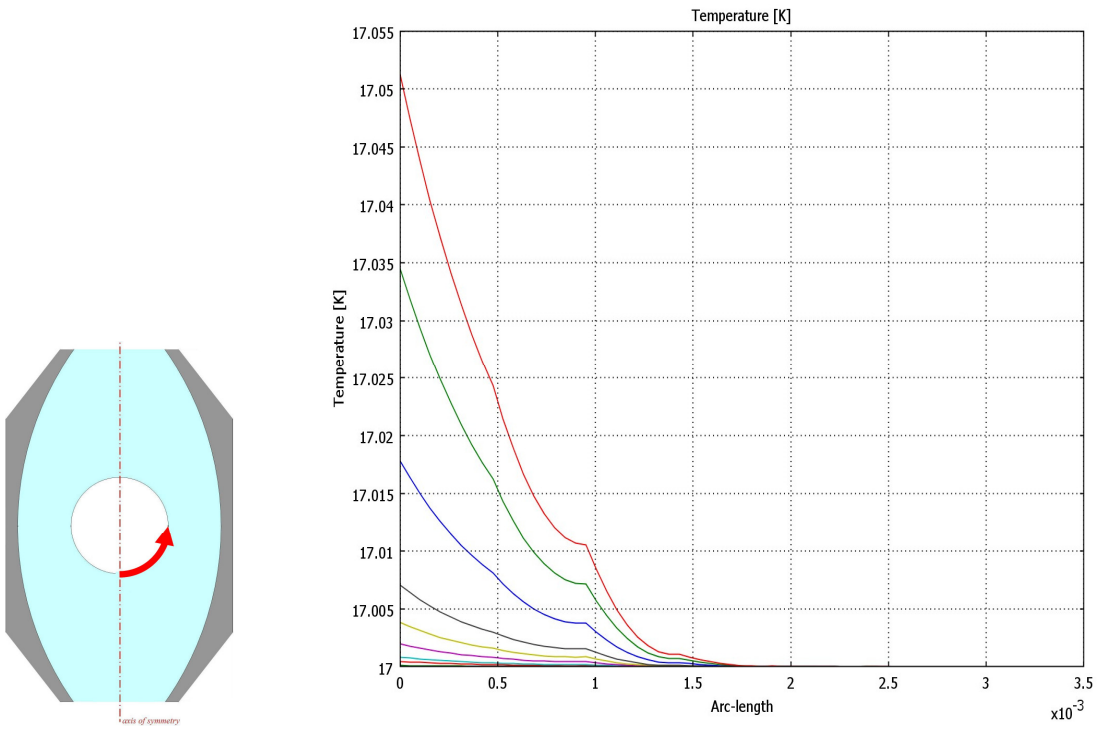

Figure 4.25: Helium Temperature Profile along Fuel Capsule Surface Starting From the Axis of Symmetry Moving Angularly Away 90° in 1 ms Intervals

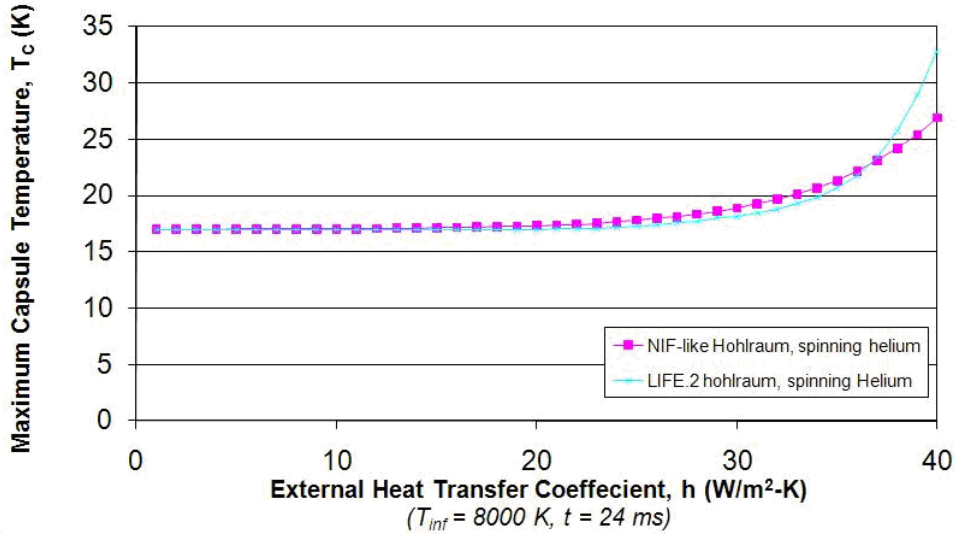

Figure 4.26: Maximum Helium Temperature along Fuel Capsule's Surface along Axis of Symmetry as a Function of the External Heat Transfer Coefficient

Despite the NIF-like target having a shorter distance from LEH window to capsule surface compared to the LIFE.2 target - 4.3 mm versus 5.58 mm measured along the axis

of symmetry - the LIFE.2 fuel capsule is more sensitive to heating at elevated heat transfer coefficients. Currently, a temperature increase of 1 degree is seen for the NIF-like target for a heat transfer coefficient of 27 $W/m^2 \cdot K$ and 29 $W/m^2 \cdot K$ for the LIFE.2 target.

The sudden and drastic change in temperature near the capsule's surface is attributed to changes in the thermal diffusivity of the helium coupled with the amount of time the hohlraum is exposed to heating. The speed in which the density wave propagates axially inward is dependent on the intensity of the thermal load imposed through the LEH windows. As the external heat transfer coefficient increases, the helium temperature bordering the LEH window increases more quickly, causing a stronger density wave to propagate axially inward through the helium. This density wave is more adept to quickly compressing the remaining helium internal to the hohlraum, only stopping when the 24 ms of simulation time is reached.

The importance of this density wave is shown through its relationship with thermal diffusivity ($k/\rho c_p$). General material properties for helium show an almost constant specific heat and a maximum of 13-times increase in thermal conductivity for helium increasing in temperature from 20-1000 K and varying pressures of 1-100 bar.[6] In addition, when considering the region behind the particle wave to the LEH window shows a 23.3 to 58.8-times decrease in density, the thermal diffusivity following the wave will generally increase significantly. Therefore, for elevated cases of heat transfer coefficients or increased target transit time, helium external to the fuel capsule will begin to see a dramatic and sudden increase in temperature upon reaching a critical threshold. This threshold is evident in Figure 4.26, where the temperature at the fuel capsule surface

as dramatically increased due to the density wave reaching the capsule's surface at the end of the 24 ms run for the maximum simulated heat transfer coefficient of 40 $W/m^2 \cdot K$.

When dealing with heating of regions in series, *i.e.* the window and internal helium, the medium of highest thermal resistance is dominant in determining the transient response of the system as a whole. Considering the hypothetical case of the window heating to 2,220 K with an external heat transfer coefficient of 40 $W/m^2 \cdot K$, the internal helium with "virtual" LEH windows requires a time of 24 ms, as shown in Figure 4.23. From the adiabatic window heating case shown in Figure 4.18, only 4.2 ms is needed to reach the same 2,220 K. The realistic time for this system to heat to 2,220 K would be somewhere between 24 and 28.2 ms. However; since these two systems heat in series, the higher helium thermal resistance dominates dictating a solution very near 24 ms.

Chapter 4, in part, contains materials submitted to Transactions of Fusion Science and Technology, June 2011. Holdener, D. S., Tillack, M. S., Wang, X. R., 2011. The thesis author was the primary investigator and author of this paper.

References:

1. Anderson, John David. *Fundamentals of Aerodynamics*. 3rd ed. Boston: McGraw-Hill, 2001. pp 499. [ISBN: 0-07-237335-0]

2. Bird, Bird, G. A. *Molecular Gas Dynamics and the Direct Simulation of Gas Flows*. Oxford: Clarendon, 1994, pp. 2-3.

3. Incropera, Incropera, Frank P., David P. DeWitt, Theodore L. Bergman, and Adrienne S. Lavine. *Introduction to Heat Transfer.* 5th ed. Hoboken NJ: Wiley, 2007: pp. 256-261.

4. NIST Cryogenic Technologies Group, “Material Properties: Polyimide (Kapton)”, <http://cryogenics.nist.gov/MPropsMAY/Polyimide%20Kapton/PolyimideKapton_rev.htm>.

5. "DuPont Electronics : Kapton® Polyimide Film." *DuPont. The Miracles of Science™*. Web. 12 Nov. 2009. <http://www2.dupont.com/Kapton/en_US/>.

6. Lide, David R., and William M. Haynes. *CRC Handbook of Chemistry and Physics*. Boca Raton, FL: CRC, 2009. 6.21-27.

Chapter 5:

Conclusions and Recommendations

Utilizing direct simulation Monte Carlo and Navier-Stokes CFD methods, the heating of the LIFE targets transversing the target chamber has been analyzed for thermal correlations. The simulation codes DS2V and ANSYS provided the ability to analyze the convective heating from the xenon gas of the chamber to the LIFE hohlraum and provide consistent flow field solutions and heat fluxes to the target's surface. Empirical and analytical heating results produced consistent results with the code simulation, while the codes themselves closely matched each other.

DS2V proved to be far simpler and robust in obtaining accurate solutions yet compared to ANSYS is far slower in obtaining them. Preliminary ANSYS simulations indicated a heat flux a factor of two lower than expected, and considerable effort was dedicated to help explain why this differed with the DS2V solution. It was found that a continuum assumption of CFD methods was becoming inaccurate near the surface of the hohlraum; however this proved inconsequential when material properties, boundary conditions, and mesh densities of the ANSYS simulations were carefully reviewed and a more consistent heating profile obtained.

Changes in the dimensionless variables of the Nusselt number governing this flow were found to help characterize target performance. Varying flow parameters such that the targets travel as fast as possible, it was concluded the reduction in flight time deemed to offset the increase in heat transfer coefficient thereby reducing the total heat load on the target would be beneficial so long as flight instabilities from the local speed of sound did not occur or the target speed became to great to feasibly engage the targets. Varying additional parameters like the size and shape of the hohlraum can be shown to have an enormous effect on its localized heating. For instance, reducing the windward surface profile of the LIFE.2 target successfully makes the target more aerodynamic, but has adverse heating effects to the sensitive LEH window. This concept was further exemplified with the inclusion of baffles, which successfully traps air near the LEH window, thereby reducing the convective heating mechanisms, resulting in a significant lowering of the heat flux to the window.

Changes in the heat transfer coefficient were also seen from variation of the xenon gas and hohlraum surface temperatures. These calculations were accomplished through changes in the temperature-dependent thermal conductivity and viscosity of the Reynolds and Prandtl numbers. For the case of an ever increasing wall temperature, the heating coefficient has the potential of increasing 30 and 25% for the old and new target flight conditions respectively, however more significant was the doubling in heat transfer coefficient as a result from raising the xenon in the new chamber from 1000 to 8000 K.

From the transient thermo-mechanical analysis of the hohlraum, the heating of the LEH window and fuel capsule was found largely dependent on the internal helium. Independently, the half-micron thick windows have very little thermal resistance and are

shown to heat up very quickly. Inclusion of helium on the inside surface of the LEH window proved to be a tremendous heat sink, pulling heat away from the window and towards the fuel capsule. It was also found that spinning the hohlraum during this heating process produced buoyancy-driven swirling effects, exacerbating the cooling of the window and heating of the capsule. However, only when the LEH windows were exposed to very high heat transfer coefficients did any appreciable amount of heat reach the capsule.

Based on the results of the work herein, it is highly recommended the LIFE targets include external baffles on the forward and leeward surfaces. These baffles have been shown to be a simple addition independent of all other target parameters, and to effectively reduce the heat transfer to the window on the windward surface. Reduction in the LEH window diameter was also shown to reduce the overall heat load to the interior of the hohlraum and keep the window temperature to a minimum. It is also highly recommended that the internal radiation shields be made to completely partition the helium into a number of regions. Why this will likely increase the temperature of the LEH windows, the fuel capsule will hopefully be sufficiently shielded from extraneous heat carried by the swirling helium.

Future simulations are required to better understand the transient heating response of the hohlraum. This includes a comprehensive look at the convective and radiation modes of heat transfer with a fully develop target model of LEH windows, lead walls, radiative shields, internal helium and fuel capsule with the internal DT ice layer. A more detailed design study of the size and shape of the baffles - along with other design variables - would be beneficial in maximize their effectiveness in protecting the LEH

windows and fuel capsule. Ultimately however experimental validation of these heating results must be performed on the physical system. LIFE is being designed at a rep-rate of 20 Hz, resulting in approximately 1.7 million targets being engaged daily. Target design and survival is a pivotal engineering task in the LIFE project, and requires a substantial effort in its optimization and testing, let alone demonstration of large-scale fabrication, before successfully being implemented.

Chapter 5, in part, contains materials submitted to Transactions of Fusion Science and Technology, June 2011. Holdener, D. S., Tillack, M. S., Wang, X. R., 2011. The thesis author was the primary investigator and author of this paper.

Appendix A:

Xenon Transport Properties

Modeling the convective hat transfer to the target in the LIFE chamber under current specifications, the 17 Kelvin target will be shot into the hostile, high temperature xenon gas environment at 8000 Kelvin. Traversing the target chamber, a thermal boundary layer will develop where heat is transferred from the xenon to the hohlraum. This heat flux into the target is dependent on the temperature difference between the chamber gas and the hohlraum's surface, and will decrease over time as the surface comes into thermal equilibrium with the chamber gas. Accurately representing the transport properties of xenon through this thermal boundary layer and accompanying temperature gradient is critical in validating the heat transfer models.

A.1: Xenon Phase Diagram

As the hohlraum enters the LIFE chamber, a stagnation region will develop on the blunt leading surface as it travels upwards of 250 m/s. The pressure along this leading edge will increase from 276 to 372 Pa or 3,037 to 3,228 Pa based on the old or new target flight conditions for isentropic compression. The xenon gas deposits onto the target surface until the wall reaches its critical sublimation temperature of 110 or 127 K based

on this isentropic compression and careful examination of Figure A.1 below. Deposition of the xenon gas onto the surface of the hohlraum was not the focus of this work, and thus steady state solutions were found by holding the hohlraum wall temperature at an elevated 150 K.

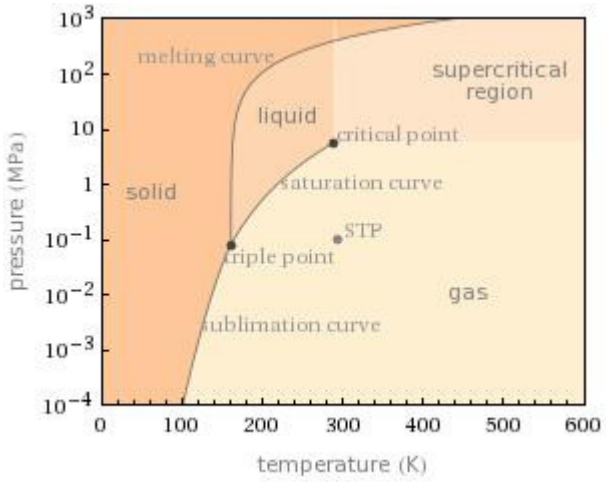

Figure A.1: Xenon Phase Diagram[1]

While deposition of xenon onto the surface of the hohlraum is an exothermic reaction, further investigation into the rate of deposition is possible, but not necessary for the LIFE project. As demonstrated in Chapter 4, preliminary transient heating results of the hohlraum show the surface temperature of the LEH window rise past 500 K in 1 ms for the new flight conditions (see Figure 4.24). This time represents approximately 4% of the total target flight time in the chamber. Once the critical temperature is reached, remaining xenon ice will quickly sublimate in an endothermic reaction, pulling the same amount of energy from the target as was put in during the exothermic deposition process, producing a net-zero energy transfer.

A.2: Estimated Transport Properties from the Lennard-Jones Potential

Viscosity and thermal conductivity can be predicted using kinetic theory until the onset of ionization. Chapman in England and Enskog in Sweden independently solved the Boltzmann equation, developing expressions for transport properties as a function of the intermolecular forces between particles, φ(r), where r the distance between nuclei undergoing a collision. Although the exact functional form of φ(r) is not known, a satisfactory model for non-polar atoms is the Lennard-Jones (6-12)[2] potential given by equation A.1

$$\varphi(r) = 4\varepsilon\left[\left(\frac{\sigma}{r}\right)^{12} - \left(\frac{\sigma}{r}\right)^{6}\right] \tag{A.1}$$

where ε is a characteristic energy, or the maximum energy attraction between two molecules, and σ is a characteristic diameter or the collision diameter of the molecule. Using the Lennard-Jones (6-12) potential for modeling intermolecular forces between particles, the Boltzmann equation for the velocity distribution has been solved numerically yielding expressions[3] for the viscosity (μ) and thermal conductivity (k) of a given molecular weight, M, and is given by equations A.2 and A.3:

$$\mu = \frac{5}{16}\frac{\sqrt{\pi m \kappa T}}{\pi\sigma^2\Omega_\mu} = 2.6693\times10^{-5}\frac{\sqrt{MT}}{\sigma^2\Omega_\mu} \tag{A.2}$$

$$k = \frac{25}{32}\frac{\sqrt{\pi m \kappa T}}{\pi\sigma^2\Omega_k}\hat{C}_v = 1.9891\times10^{-4}\frac{\sqrt{T/M}}{\sigma^2\Omega_k} \qquad \text{(A.3)}$$

The second form of the thermal conductivity equation substitutes the molar heat capacity at constant volume, $\hat{C}_v = 3\kappa/2m$, and then both combine the integration constant, Boltzmann constant (κ) and pi, yielding the following units; if T [=] K and σ [=] Å, then μ [=] g/cm·s and k [=] cal/cm·s·K. The dimensionless quantities, Ω_μ and Ω_k, are called the collision integrals for viscosity and thermal conductivity and are identical for a particular gas species. The collision integrals are a function of the dimensionless temperature κT/ε, and account for the detailed path molecules take during a binary collision for a given φ(r). Calculated values for viscosity and thermal conductivity using the Lennard Jones (6-12) potential have been confirmed within 1% for the temperature range of 100 to 5000 K when compared to the identical approach presented by Svehea in the 1962 NASA report TR R-132.[4]

A similar approach is taken by Bich, Millant and Vogel where the transport properties are also calculated via the Chapman-Enskog formulation.[5] However, included in this formulation are higher order correction factors, in addition to the collision integral being calculated from the Aziz HFD-B type potential.[6] This model is based on a short-range Hartree-Fock (exponential) term and long-range attractive ($1/r^6$, $1/r^8$, $1/r^{10}$) terms, and is considered one of the best interatomic model potentials.[7] Reported results from Bich et al. for the viscosity and thermal conductivity for xenon up through 5000 K are presented in Figures A.1 and A.2, along side calculated values using the Lennard-Jones

(6-12) potential for characteristic diameter, σ, 4.009 Å and characteristic temperature, ε/κ, 234.7 K^3.

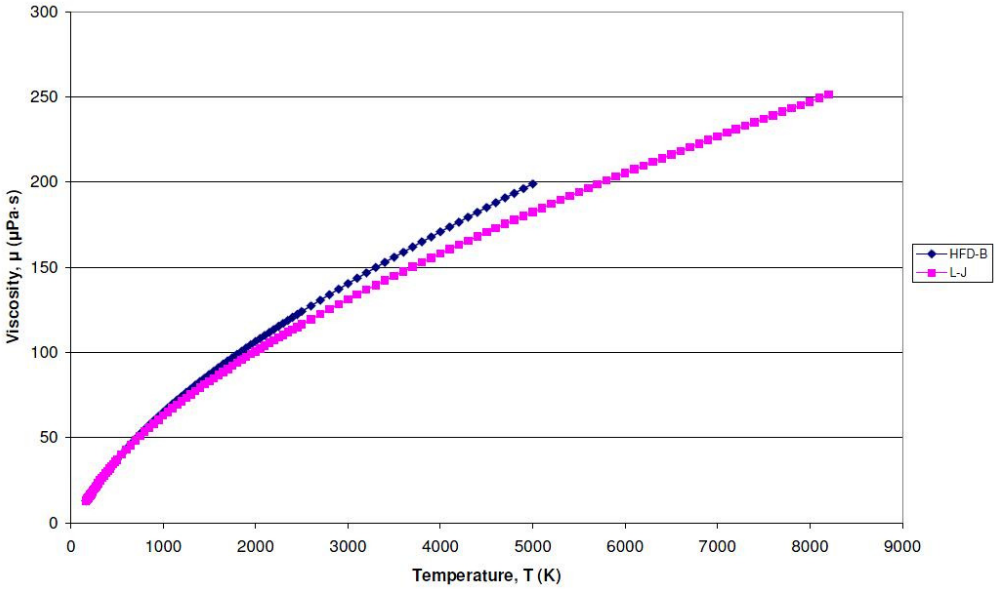

Figure A.2: Xenon Viscosity vs. Temperature

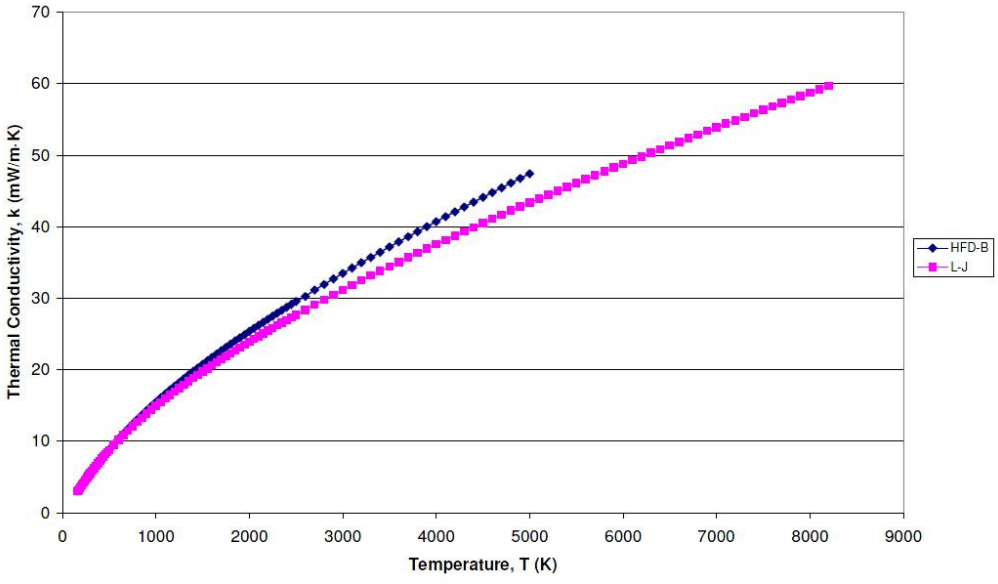

Figure A.3: Xenon Thermal Conductivity vs. Temperature

Bich et al. compares the estimated values of viscosity and thermal conductivity with a number of experimental results, including shock tube measurements for thermal conductivity taken by Mastovsky up to 7000 K[8]. This study was the only reported empirical data for xenon transport properties above 2000 K, and consistently yielded lower results than Bich's estimated values by 1-2% for xenon. It is of note this method appears not to be as accurate for lighter noble gases, with Bich consistently reporting overestimations of 11-12% for Krypton and 6-16% for Helium among others. While this suggests the true temperature dependence of these transport properties is between the presented correlations, with results from Bich using HFD-B interatomic potentials being slightly more accurate, this work exclusively uses using Lennard-Jones (6-12) for consistency between DS2V simulations and used through 8200 K to cover the full temperature range of the new target flight conditions.

The DSMC method represents gas properties based primarily on the coefficient of viscosity, in conjunction with variation of this parameter with temperature using a power law of the form equation A.4 below[9]

$$\mu \propto T^{\omega} \tag{A.4}$$

As Bird notes, simulating spheres of varying diameter at the molecular level is related to the variation of the coefficient of viscosity with temperature at the continuum level[9]. By applying a power-law curve fit to the Lennard-Jones estimation for viscosity for the appropriate temperature range, the required temperature-dependent viscosities were

obtained for both target flight conditions. Unique to the DS2V program is the use of an effective or reference diameter d_{ref}, calculated from reference temperature T_{ref}, viscosity μ_{ref}, and temperature power ω from equation A.5 below[9]

$$d_{ref} = \left(\frac{5\left(mkT_{ref}/\pi\right)^{1/2}}{2(5-2\omega)(7-2\omega)\mu_{ref}} \right)^{1/2} \tag{A.5}$$

A summary of these calculated DS2V parameters are shown in Table A.1.

Table A.1: DS2V Viscosity Reference Parameters

	Lennard-Jones Parameters[3]		
Characteristic Diameter, σ	4.009 Å		
Characteristic Temperature, ε/κ	234.7 K		
	DS2V default[9]	Old TFC	New TFC
Temperature Range	N/A	150-1125 K	150-8200 K
Reference Temperature, T_{ref}	273 K	638 K	4175 K
Temperature Power, ω	0.85	0.8721	0.6958
Reference Viscosity (@ T_{ref}), μ_{ref}	21.07 μPa·s	45.0 μPa·s	162.5 μPa·s
Reference Diameter (@ T_{ref}), d_{ref}	5.74 Å	4.91 Å	3.80 Å
Coefficient of Determination, R^2	N/A	0.9954	0.9952

A.3: Ionization Using the Saha Equation

Kinetic theory is utilized for the transport properties of non-polar atoms until the onset of ionization. With the temperature of the LIFE chamber estimated to be around 8000 K, a brief look into the ionization of xenon gas is warranted, via the Saha Equation.

From the law of mass action, Vincenti and Kruger derive the Saha Equation, employing the following assumptions[10]:

1. Gas is in thermal equilibrium
2. Only three types of molecules are present: neutral atom, singly ionized atom, and electrons
3. Electric charge and mass is conserved
4. Interaction of the gas with surroundings is neglected

By defining the fraction of the originally neutral particles that have become ionized as the degree of ionization Φ ($0 \leq \Phi \leq 1$), Vincenti and Kruger find

$$\frac{\phi^2}{1-\phi} = \frac{m_z}{\rho}\left(\frac{2\pi m_e \kappa T}{h^2}\right)^{3/2} \frac{2\prod_{\text{int}} Q_{\text{int}}^{z^+}}{\prod_{\text{int}} Q_{\text{int}}^{z}} \exp\left(-\Theta_i / T\right) \tag{A.6}$$

Equation A.6 gives the degree of ionization as a function of density and temperature, where m_z is the mass of a Z-particle, m_e is the mass of an electron, h is Plank's constant, $\prod_{\text{int}} Q_{\text{int}}^{z}$ and $\prod_{\text{int}} Q_{\text{int}}^{z^+}$ are the product of internal partition functions for the neutral and singly ionized atom respectively, and Θ is the characteristic energy for ionization. Using the perfect gas law in relating pressure with number density, equation A.7 can be expressed in terms of pressure in the form:

$$\frac{\phi^2}{1-\phi^2} = \frac{1}{p}\left(\frac{2\pi m_e}{h^2}\right)^{3/2}(\kappa T)^{5/2}\frac{2\prod_{\text{int}} Q_{\text{int}}^{z^+}}{\prod_{\text{int}} Q_{\text{int}}^{z}}\exp(-\Theta_i/T) \tag{A.7}$$

In this isobaric form of the Saha equation, the degree of ionization may be solved for implicitly as opposed to solving a quadratic in the density form.

Xenon is a monatomic gas, and consequently has no internal energy contribution from rotation and vibration. Only the internal energy associated with electrons within the atom need to be considered, and consequently maintains a constant specific heat until the onset of ionization. The degeneracy factors and characteristic temperatures needed for this calculation have been compiled and presented by E. B. Saloman for the National Institute of Standards and Technology[11]. Including the first 50 characteristic temperatures for electronic excitation within the partition functions, as well as the first characteristic ionization energy of xenon at 12.12984 eV[12] (140,755 K) the degree of ionization is calculated from equation A.6 as a function of temperature for a select few pressures, results of which are shown in Figure A.4.

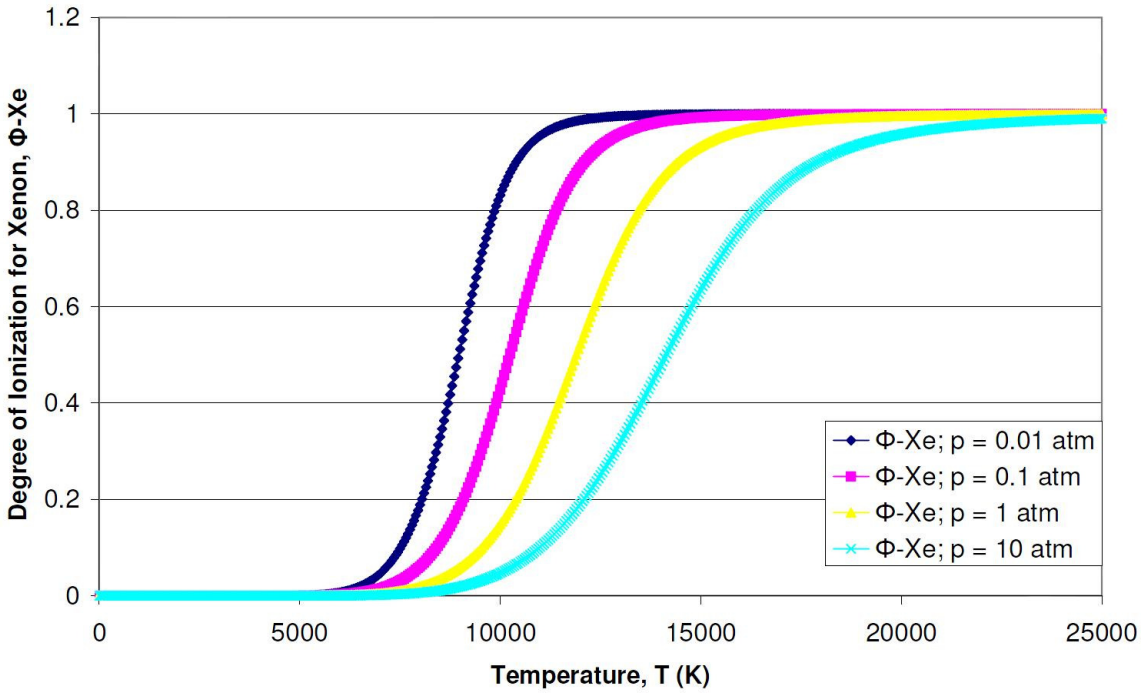

Figure A.4: Degree of Ionization as a Function of Temperature and Pressure

The onset of ionization begins suddenly and rapidly, as expected from the exponential term of temperature in equations A.4 and A.5. Also of note is the inverse relationship of ionization with the density and pressure of the system. Despite the characteristic ionization energy being so much greater than normal temperatures, the tail ends of the velocity distribution are fast enough for particles to become ionized, but the 3-body-collisions required for recombination become less frequent at lower densities and pressures. This yields lower degrees of ionization for the same gas temperatures.

Specific to the LIFE.2 new target flight conditions, the degree of ionization has been calculated at 11.0%. If the internal partition functions are not accounted for, as is the case in the simplified form of the Saha Equation presented by Chen,[13] the ionization drops to 3.8%. Figure A.5 was constructed to look at the effect of internal energy, showing the ratio of internal partition functions due to electronic excitation for singly

ionized to neutral xenon gas as a function of temperature. Note, Figure A.5 and the calculation presented by Chen also do not include the constant 2 grouped with the ratio of the partition functions. This constant comes from the two permissible quantum energy states associated with the spin of an electron. For the temperature range of interest (< 12,000 K), only the first few electronic excitations are important in accurately accounting for xenon internal energy contributions to the partition function, as is typically the case.

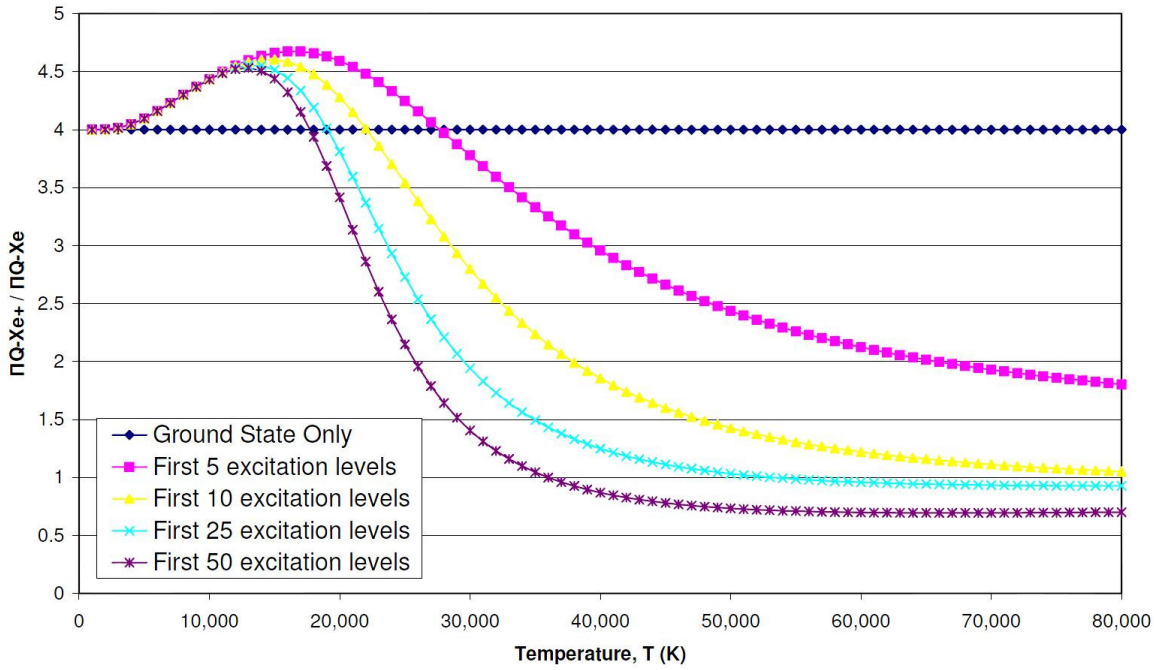

Figure A.5: Ratio of Internal Partition Functions Due to Electronic Excitation for Singly Ionized to Neutral Xenon versus Temperature

The main limitation in apply the Saha Equation to the state of the LIFE chamber is that Saha requires local thermodynamic equilibrium. Correspondence with LIFE members responsible for the design specification of 8000 K of xenon gas with no appreciable ionization confirm this is a non-equilibrium issue, depending on the interplay between the recombination, cooling, and electron-ion coupling rates. Local thermodynamic equilibrium is not expected to be reached in the maximum time of 100

ms between shots.[14] With ionization expected to not be an issue, using the Lennard-Jones model for intermolecular forces to solve for xenon's transport properties remains applicable.

Appendix A, in part, contains materials submitted to Transactions of Fusion Science and Technology, June 2011. Holdener, D. S., Tillack, M. S., Wang, X. R., 2011. The thesis author was the primary investigator and author of this paper.

References:

1. "Phase Diagram of Xenon - Wolfram|Alpha." *Wolfram|Alpha: Computational Knowledge Engine*. Web. 19 Mar. 2011. <http://www.wolframalpha.com/input/?i=phase+diagram+of+xenon>.

2. (Lennard-)Jones, J. E. "On the Determination of Molecular Fields. I. From the Variation of the Viscosity of a Gas with Temperature; II. From the Equation of State of a Gas." *Proceedings of the Royal Society* A106 (1924): 441-62, 463-77.

3. Bird, Robert Byron, Edwin N. Lightfoot, and Warren E. Stewart. *Transport Phenomena*. 2nd ed. New York: Wiley, 2007. Print.

4. Svehla, Roger A. *Estimated Viscosities and Thermal Conductivities of Gases at High Temperatures*. Tech. no. NASA TR R-132. Cleveland, Ohio: Lewis Research Center, 1962.

5. Bich, E., J. Millant, and E. Vogel. "The Viscosity and Thermal Conductivity of Pure Monatomic Gases from Their Normal Boiling Point up to 5000 K in the Limit of Zero Density and at 0.101325 MPa." *Journal of Physical Chemistry* 19.No. 6 (1990): 1289-305.

6. Aziz, Ronald, Frederick McCourt, and Clement Wong. "A New Determination of the Ground State Interatomic Potential for He 2." *Molecular Physics* 61.6 (1987): 1487-511.

7. Ceperley, D. M. "Path Integrals in the Theory of Condensed Helium." *Reviews of Modern Physics* 67.2 (1995): 279-355.

8. Mastovsky, J. Tech. no. Z-1026/87. CSAV. Ustav Termomechaniky, Prague: 1987.

9. Bird, G. A. *Molecular Gas Dynamics and the Direct Simulation of Gas Flows*. Oxford: Clarendon, 1994: pp. 92, 408-409

10. Vincenti, Walter G., and Charles H. Kruger. *Introduction to Physical Gas Dynamics*. Huntington, NY: Krieger, 1975. Print.

11. Saloman, E. B. "Energy Levels and Observed Spectral Lines of Xenon, XeI through XeLIV." *Journal of Physical and Chemical Reference Data* 33.3 (2004): 765.

12. Lide, David R. *CRC Handbook of Chemistry and Physics: a Ready-reference Book of Chemical and Physical Data*. Boca Raton, FL: CRC, 2009. Print.

13. Chen, Francis F. *Introduction to Plasma Physics*. New York: Plenum, 1974. Print.

14. Tillack, Mark S. "Ionization of Xe." Message to Howard Scott. 3 Mar. 2011. E-mail.